Synthesis of Cr-doped SrTiO₃ nanocrystals for photocatalytic CO₂ reduction applications

Vangroenweghe Louis

Promotor: Prof. Dr. I. Van Driessche
Co-promotor: Dr. Katrien De Keukeleere
Supervisor: Jonas Billet

Acknowledgements

As my thesis year comes to an end I would like take the time to reflect on the years that have passed and the people that I've met during my study at UGent. Six years ago, I decided to study chemistry because of my nature of wanting to understand how things work, both on a molecular level and a macro scale. Now, six years later, I am about to finish my Master's degree in Chemistry and will extend my academic journey with another two years in Engineering.

I can honestly say that my experiences at the UGent have helped make me the person that I am today. I have learned to be a critical thinker. I have learned how to organise myself and achieve deadlines. I have learned how to work together in teams and work towards a common goal. And most importantly, I have learned that I can do anything if I put my mind to it.

First of, I would like to thank Jonas Billet for the continued guidance and support throughout my thesis year. With every question or proposition I could appeal on his expertise and practical experience. Besides his role as a supervisor he was also a daunting opponent in our afternoon kicker sessions. I would also like to thank Evert D'Haene for his expertise in the wondrous world of NMR, for his guidance in the lab, and for teaching me how to work more efficiently and focussed in the lab. Furthermore I would like to thank professor doctor Isabel Van Driessche and professor doctor Klaartje De Buysser for providing me the opportunity to work on my master dissertation in the SCRIPTS group. From day one the SCRIPTS group has welcomed me with open arms and I could not have wished for a better research group to work on my master thesis.

Last but not least I would like to thank my parents for their continued support and encouragement over the course of my study. Thank you for believing in me.

Synthesis of Cr-doped SrTiO₃ nanocrystals for photocatalytic CO₂ reduction applications

L. Vangroenweghe,[a] J. Billet[a] and Isabel Van Driessche[a]

1st June 2018

[a] Department of Inorganic and Physical Chemistry, Sol-gel Centre for Research on Inorganic Powders and Thin films Synthesis (SCRIPTS)
Ghent University, 9000 Ghent, Belgium

Abstract

SrTiO₃ is an ABO₃ type perovskite oxide which exhibits excellent physical and chemical properties and has the theoretical potential to efficiently convert CO_2 molecules into value added chemicals such as CH_4 and CH_3OH. Highly crystalline, monodisperse $SrTiO_3$ nanocrystals (NCs) were synthesized with trioctylphosphine oxide (TOPO), serving both as a solvent and a structure directing agent in the NC synthesis. The NCs were doped with Cr^{3+} ions to extend the optical response to the visible light region, thus increasing its photocatalytic performance. Through surface modifications, the native TOPO ligands were exchanged for oleic acid which where then stripped off through a mild BF_3:Et_2O stripping procedure to render near-bare cationic NCs. The ligand stripped NCs could then be utilized as building blocks into a mesoporous NC framework through a polymer-templated assembly which were then deposited as mesoporous powders. Finally, the obtained mesoporous NC frameworks were characterized through N_2 adsorption-desorption and UV-Vis measurements, and the photocatalytic ability was briefly explored through the photodegradation reaction of methylene blue and methylene orange.

1 Introduction

The rapid consumption of fossil fuels and inherent production of the greenhouse gas (GHG) carbon dioxide (CO_2) is one of the key challenges our society faces in the 21st century. CO_2 emission by anthropogenic sources amounts to 76%[1] of global GHG emissions and it is estimated that 35 Gt of CO_2 is released every year by large fossil fuel facilities, biomass energy facilities and other major CO_2-emitting industries.[2] The reason why CO_2 is such a persistent GHG in our atmosphere is due to its double C=O bond which possesses a much higher bond energy (799 kJ/mol) as compared to C–C bonds, C–H bonds and C–O bonds (respectively 347 kJ/mol, 413 kJ/mol and 358 kJ/mol).[3] Furthermore, CO_2 exhibits a large energy gap between its LUMO and HOMO (13.7 eV) and a large electron affinity (-0.6 ± 0.2 eV), which make it an inactive molecule.[4] As a result of this thermodynamic stability, transforming CO_2 into hydrocarbons and intermediates requires harsh reaction conditions. Fortunately, the photocatalytic conversion of CO_2 offers a feasible alternative to convert this GHG into value added chemicals under milder reaction conditions. In the strive for a circular CO_2 economy, the large scale photocatalytic conversion of CO_2 into CH_4 and CH_3OH has received particular interest in the scientific community.[5]

Photocatalyst materials composed of transition metal oxides and group IIIA metal oxides are the most widely studied materials for CO_2 reduction applications owing to their high catalytic activity, stability and low cost.[6–8] More specifically, perovskite-phase mixed metal oxide nanostructures demonstrate excellent photocatalytic activity for CO_2 reduction applications and hence are at the scope of this research.[3,9] One such perovskite oxide which exhibits a high potential for application in CO_2 photoreduction processes and organic dye degradation is strontium
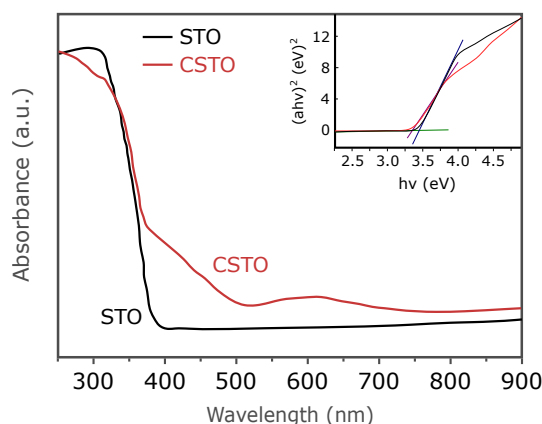
titanate (SrTiO$_3$).[10]

Figure 1: UV-Vis absorption spectra of pristine SrTiO$_3$ and Cr-doped SrTiO$_3$ as measured by Bi et al.[11]

SrTiO$_3$ is a semiconductor with a bandgap energy of 3.2 eV, and thus is only optically active upon UV light irradiation. As UV light only accounts for 4% of sunlight, SrTiO$_3$ is far from an ideal CO$_2$ photocatalyst. A way to increase the photocatalytic application potential of SrTiO$_3$ is to dope the photocatalyst with foreign elements which pull the optically active region to the visible light region, accounting for 43% of sunlight.[12] Bi et al. proved that by incorporating Cr^{3+} ions into the SrTiO$_3$ perovskite oxide, the visible light response was succesfully enhanced (figure 1), and the photocatalyst could be applied in the CO$_2$ photoconversion reaction to CH$_4$ and CH$_3$OH.[11] Furthermore, introducing elements which possess a lower oxidation state than the Ti^{4+} ions induces oxygen vacancies in the surface (figure 2). Surface oxygen vacancies can improve adsorption of surface species and can act as photoinduced charge traps, aiding charge transfer to the surface adsorbed CO$_2$ molecules.[13]
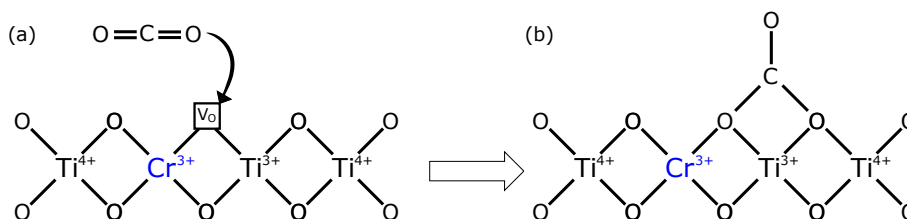

Figure 2: Illustration of the influence of Cr doping on SrTiO$_3$'s surface (a) Cr^{3+} induced surface oxygen vacancy on SrTiO$_3$, and (b) enhanced adsorption site for CO$_2$ molecules

Various studies have shown nanoparticles (NPs) to exhibit greater photocatalytic activity as compared to their bulk counterpart due to their large surface area, optical properties, and catalytic nature.[14–17] The most common solvent for NC synthesis is benzyl alcohol, resulting in the synthesis of highly crystalline NCs that are often agglomerated as-synthesized and can be stabilized by adding surfactants.[18] Surfactant containing synthesis routes have also been studied with a variety of group 4 metal oxides, producing highly crystalline, non-agglomerated NPs.[19] Quite recently, De Roo et al. published a paper where the surfactant tri-n-octylphosphine oxide (TOPO) was used as a solvent to synthesize TiO$_2$, ZrO$_2$ and HfO$_2$ NPs with pristine reaction control.[19] The surfactant solubilizes the growing nanoparticles whilst also serving as a structure directing agent, leading to highly monodisperse and crystalline NCs that exhibit excellent scalability and colloidal stability.[19]
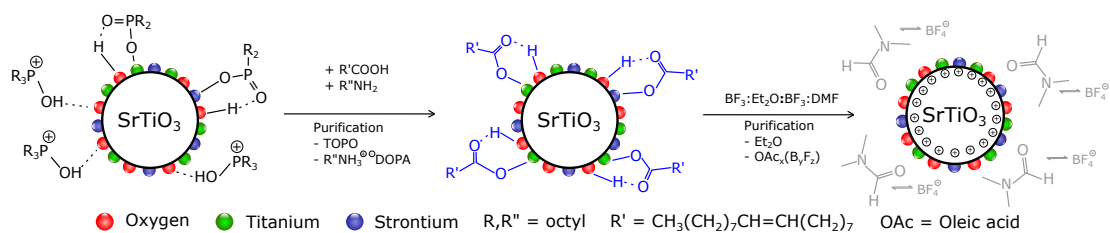
Figure 3: Overview of surface modifications performed on the nanocrystal: the d-n-octylphosphinate shell is first exchanged to a carboxylate shell through oleic acid treatment under basic conditions before being stripped off through a mild BF_3:Et_2O/DMF ligand stripping procedure.

The native coordinating ligands acquired during synthesis are necessary to exert control over NC size, composition, morphology, and dispersibility, but are often not beneficial for the final application in terms of chemical behaviour, physical properties and catalytic activity.[20] As for $SrTiO_3$, with a surface resembling that of the TiO_2 NCs, it is expected that the surface is covered with neutral TOPO, protonated TOPO and di-n-octylphosphinate ligands.[19] The NCs can be processed into 3D ordered mesostructures through the use of block-copolymer (BCP) architecture-directing agents.[21] Before being able to arrange these NCs into a mesoporous network, the native ligands have to be stripped off of the NCs surface to allow favourable interaction with the BCPsNC-tethering domains. Through the use of oleic acid (OAc)/n-octylamine (octAm) we are able to exchange the native TOPO ligands and TOPO derivatives for OAc. The OAc ligands can then be stripped from the surface through a facile BF_3:Et_2O stripping method in DMF developped by Doris et al. (figure 3).[21] Once the ligand stripped NC building units are obtained, the assembly of colloidal NCs frameworks can be accomplished through the use of PDMA-b-PS BCPs. These BCPs contain a NC-tethering domain (PDMA) that interacts with the bare NC surface as if it were DMF molecules, and a pore-generating domain that controls the pore sizes in the NC framework (figure 4). The pore sizes, wall thickness and periodicity can be finely tuned by altering the M_w of the PS block, the M_w of the PDMA block, and the M_w of both BCP domains respectively, thus allowing extensive control over the properties of the mesoporous material.

2 Experimental

SrTi(OEtOMe)$_6$ precursor synthesis

A SrTi(OEtOMe)$_6$ precursor was prepared to gain a 1:1 Sr:Ti ratio in the $SrTiO_3$ NCs. To start, 0.525 g of Sr (6 mmol) and 1.776 mL Ti(OiPr)$_4$ (6 mmol) was dissolved under inert atmosphere (Ar) in 1.892 mL (24 mmol) and 5.677 mL (72 mmol) of MeOEtOH respectively. The Sr solution was heated to 60 °C while stirring until Sr was completely dissolved. The Ti(OiPr)$_4$ MeOEtOH mixture was heated to 80 °C under vacuum while vigorously stirring and 1.892 mL (24 mmol) of additional MeOEtOH was added two consecutive times to the Ti(OiPr)$_4$ mixture to force a complete ligand exchange. Both solutions were added into a 100 mL three-neck flask under argon atmosphere and the mixture was refluxed overnight at 135 °C.

Nanocrystal synthesis

The $SrTiO_3$ NCs were synthesized by degassing 13.2 g of TOPO to 65 °C to remove any adsorbed water. After degassing, the flask was flushed with argon and 3 mmol of SrTi(OEtOMe)$_6$ precursor was added. For the Cr-doped $SrTiO_3$ NC synthesis, chromium acetylacetonate (0.15 mmol) was dissolved in 0.5 mL of MeOEtOH and was added along with the SrTi(OEtOMe)$_6$ precursor. The residual unbound MeOEtOH was vacuumed off as the mixture was slowly heated to 100 °C while vigorously stirring. When no more bubbles were formed the mixture was flushed
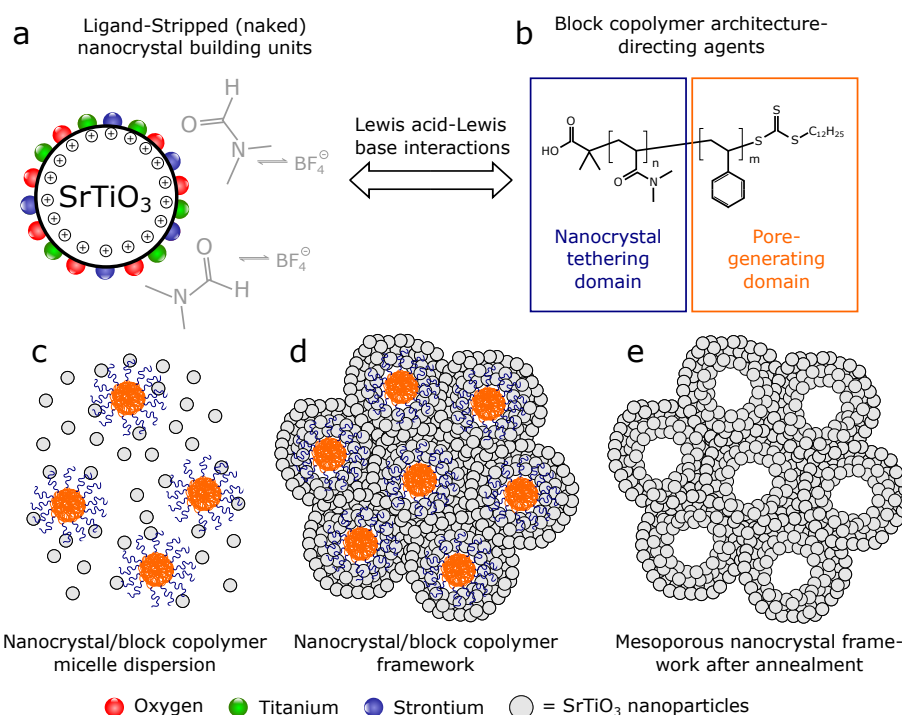
Figure 4: (a) naked cationic $SrTiO_3$ nanoparticles, (b) PDMA-b-PS block-copolymer, (c) nanocrystal/block-copolymer dispersion, (d) nanocrystal/block-copolymer framework, and (d) mesoporous nanocrystal framework after annealing.

with argon and heated to 300 °C. After 2 hours and 30 minutes at 300 °C, the flask was allowed to cool down to 80 °C and the NCs were precipitated with 20 mL of CH_3CN at 5000 rotations per minute (rpm) for 2 min. The NCs were redispersed in 10 mL of toluene and this procedure was repeated for two consecutive times to obtain a monodisperse NC suspension in toluene.

Ligand exchange and stripping

To exchange the native TOPO ligands to OAc ligands, 200 μL of octAm and 400μL of OAc was added in excess to the NC suspension. The NCs were precipitated with 2 mL of acetone and redispersed in 1 mL of hexane along with 50μL of OAc. The NCs were then purified three consecutive times by acetone/toluene and finally redispersed in 0.5 mL of anhydrous hexane. To strip off the OAc ligands, activated DMF was prepared by adding 20 μL of boron trifluoride diethyl etherate (BF_3:Et_2O) to 500 μL of DMF. Next, 500 μL of the activated DMF solution was added to the hexane NC suspension resulting in a two-phased liquid system with hexane as the top layer ($\rho = 0.867$ g/L) and DMF as the bottom layer ($\rho = 0.944$ g/L) The two-phased system was mixed vigorously for 2 minutes and placed in the ultrasonic bath for another 2 minutes. To induce mixing of the two layers, 3 mL of toluene was added and the suspension was centrifuged for 2 minutes at 5000 rpm, dispersed in 1 mL of DMF, and washed for 2 consecutive times with 1 mL of hexane and precipitated with 2 mL of toluene. Finally, the NC precipitate was suspended in 1 mL of DMF.

Mesoporous nanocrystal framework

To synthesize the mesoporous powders, 25 mg of $PDMA_{8,3k}$-b-PS_{33k} was weighed into a 4 mL glass vial and 400 μL of DMF was added while stirring to dissolve the BCP. When the BCP was completely dissolved, 1.6 mL of EtOH was added in drops of 10 μL to obtain a micellar BCP solution. The solution was left stirring overnight. The NCs were precipitated with hex-

ane/toluene and 100 mg of dry NCs were redispersed in 100 μL of DMF. The micellar BCP solution was added to the NC suspension under vigorous stirring and the resulting BCP-NC suspension was stirred for an additonal 2 hours. The suspension was then poured onto a glass tray and heated to 80 °C for 72 hours to evaporate the solvents and form the BCP-NC framework through evaporation induced self-assembly (EISA). After three days a flake-like precipitate was obtained which was calcined at 400 °C for 2 hours at a heating rate of 2 °C/min.

Photocatalytic tests

For the methylene blue degradation experiment, the mesoporous Cr-doped $SrTiO_3$ NC frameworks were first grounded into a fine powder and 15 mg of NCs was added to a 50 mL methylene blue solution (0.05 g/L). For the methylene orange degradation experiment, 50 mg of the grounded NCs was added to a 50 mL methylene orange solution (0.01 g/L). Both organic dye mixtures were transferred into separate glass containers at a constant temperature of 25 °C. The mixture was stirred for one hour in complete darkness. A sample was taken before (H00) and after 1 hour of stirring (H0). After 1 hour of stirring, the UV lamp (mercury lamp $\lambda = 365$ nm) was turned on and a sample was taken every 15 minutes for the first four samples and every 30 minutes after that.

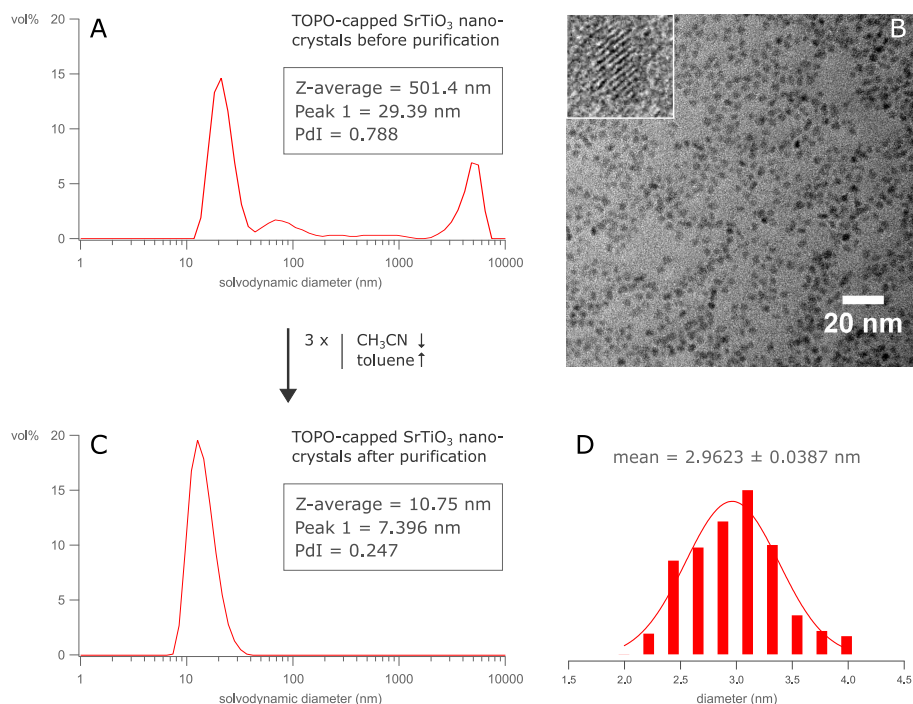## 3 Results and discussion

3.1 nanocrystal characterization

Figure 5: (A) DLS image of as-synthesized TOPO-capped $SrTiO_3$ nanoparticles before CH_3CN purification and (C) after CH_3CN purification (B) TEM image of TOPO capped $SrTiO_3$ nanoparticles after CH_3CN purification and (D) histogram of nanoparticles size.

Image 5 shows the dynamic light scattering (DLS) spectrum of TOPO-capped $SrTiO_3$ NCs. The as-synthesized $SrTiO_3$ NCs surface is coated with protonated TOPO, through H-bonding with the surface O-species, di-n-octylphosphinate, through covalent bonding with the surface Sr and

Ti atoms, and surrounded by free unbound TOPO. Before CH_3CN purification, large agglomerates are present in the NC suspension owing to the free unbound TOPO molecules present in the suspension. After three consecutive CH_3CN purification steps, the agglomerates have disappeared and a sharp peak around 10 nm has emerged with the major peak indicating a size of 7.396 nm and a polydispersity index of 0.255. The CH_3CN purification steps have washed of all unbound TOPO and gave result to a monodisperse NC suspension. TEM images further confirm the monodispersity and non-agglomeration of the NCs (figure 5.B). The size of the NCs was also plotted in a histogram using the TEM results, resulting in an average size of $\pm$ 2.90 nm.
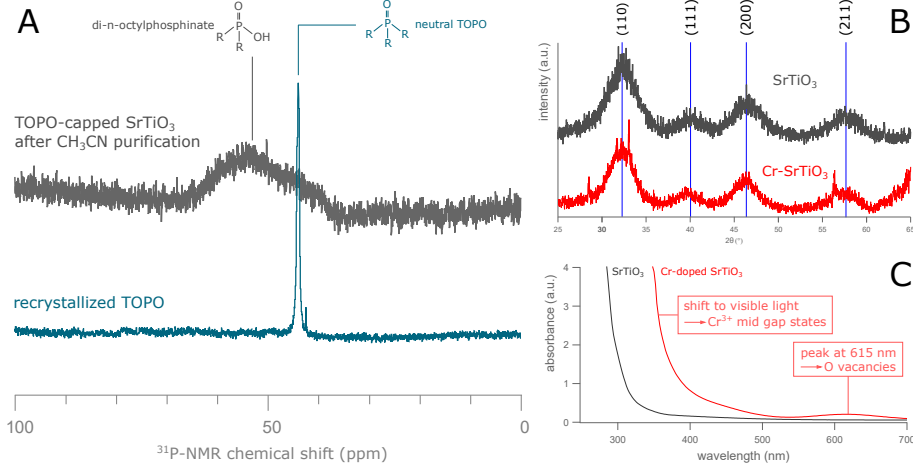
Figure 6: (A)(top) ^{31}P-NMR spectrum of SrTiO$_3$ NCs after CH$_3$CN purification, (bottom) ^{31}P-NMR spectrum of pure TOPO after recrystallisation; (B) (top) XRD spectrum of the cubic crystal structure of Cr-doped SrTiO$_3$, (bottom) XRD spectrum of the cubic crystal structure of undoped SrTiO$_3$; (C) UV-Vis measurement of undoped SrTiO$_3$ and Cr-doped SrTiO$_3$ nanocystals capped with oleic acid ligands, displaying a shoulder formation at 500 nm induced by the Cr^{3+} ions, and a peak at 615 nm owing to the oxygen vacancies in Cr-doped SrTiO$_3$.

To assign which types of TOPO derivatives are bound to the NC surface, a ^{31}P-NMR spectrum was taken (figure 6.A). The bottom spectrum displays the ^{31}P-NMR spectrum for pure, recrystallised TOPO. The sharp resonance peak at $\delta = 43$ ppm coincides with that of free neutral TOPO. No further peaks are visible in this spectrum which indicate that the recrystallised TOPO is indeed pure. The top ^{31}P-NMR spectrum was taken from the SrTiO$_3$ NCs suspension after three consecutive CH$_3$CN purification steps. The resonance peak at $\delta = 57$ ppm can be ascribed to di-n-octylphosphinate (DOPA) groups that are bound to the NC surface. The resonance peak broadening can be ascribed to the bound state of DOPA.

$$D = \frac{k\lambda}{\beta cos(\theta)} \tag{1}$$

An X-Ray diffraction (XRD) measurement was performed on the SrTiO$_3$ and Cr-doped SrTiO$_3$ NCs to identify the crystallite size and phase (figure 6.B). The measurement was performed using Cu$_{K\alpha}$ radiation in a 2θ range from 25 to 65°. Characteristic peaks can be found at 32.2°, 40°, 46.3° and 57.5° that can be assigned to the (110), (111), (200) and (211) diffractions respectively. The characteristic peaks are in perfect alignment with the diffraction peaks for the Pm$\bar{3}$m space group which corresponds with a cubic lattice structure with cell parameters a = 0.39053 nm.[22] The peak broadening is consistent over all diffraction peaks and is owed to the nanosize of the crystallite. The Scherrer equation (formula 1) was used to determine the crystallite size; where k is the constant (0.94 for this equation), λ is the X-ray wavelength ($\lambda_{K\alpha} =$ 0.15418 nm), θ is the diffraction angle of the characteristic peak with the highest intensity, 32.2° for SrTiO$_3$ which is devoted to the (110) diffraction, and β is the full width at half maximum in

radian of the (110) peak, equal to 4.3° in this spectrum. Based on this formula, we were able to calculate the crystal size to be about 2.01 nm.

To test wether the optical activity of the synthesized Cr-doped $SrTiO_3$ NCs was indeed extended to the visible light region, a UV-Vis measurement was performed on the OAc capped Cr-doped and undoped $SrTiO_3$ NCs. The resulting UV-Vis spectrum can be witnessed in figure 6.C. As can be observed from the spectrum, the UV-Vis response of Cr-doped $SrTiO_3$ NCs is significantly extended to the visible light region as opposed to the undoped $SrTiO_3$ NCs. By doping the photocatalyst with Cr^{3+} ions we thus increase the optical properties of the photocatalyst, as was intended.

3.2 Ligand exchange and stripping

To verify whether the ligand exchange procedure to OAc was successful, a ^{1}H-NMR spectrum was taken after purification (figure 7). All peaks in the ^{1}H-NMR spectrum can be assigned to that of surface bound oleyl chains which, together with the lack of P signals in the XRF results, leads to the conclusion that the native TOPO ligands are successfully exchanged for OAc ligands.
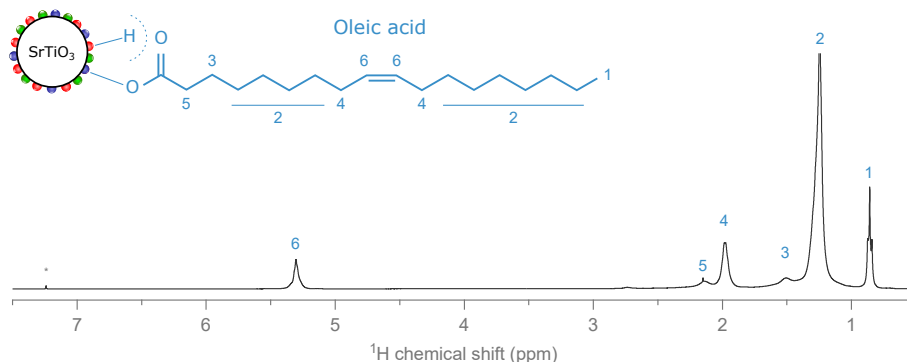
Figure 7: ^{1}H-NMR spectrum of oleic acid capped nanocrystals after the complete ligand exchange procedure and acetone purification (* = $CDCl_3$).

Figure 8 depicts the Fourier-transform infrared spectroscopy (FTIR) spectrum of the ligand stripped $SrTiO_3$ NCs versus the FTIR spectrum of OAc capped $SrTiO_3$ NCs. The OAc capped NC FTIR spectrum does not show a broad O-H stretch region between 3300-2500 cm^{-1}, indicating that all OAc is bound with the carboxylate group to the surface and no unbound OAc is present in the precipitate. Free unbound OAc displays a strong characteristic peak at 1700 cm^{-1} related to C=O stretch vibrations of carboxylic acid and C=C stretch vibrations of cis and trans OAc, which is not present in this spectrum.[23]

To utilize the $SrTiO_3$ NCs as building blocks in a NC framework, the OAc ligands have to be stripped off through a mild BF_3:Et_2O/DMF stripping procedure to allow favourable interaction of the bare cationic NC surface with BCP architecture directing agents. In the ligand stripped NC FTIR spectrum the sharp C-H stretches at around 3000 cm^{-1}, owing to CH_2 and CH_3 stretch vibrations, have strongly diminished indicating the removal of OAc ligands from the NC surface. Based on this FTIR spectrum we can conclude that the ligand stripping procedure removed the majority of OAc ligands, yet some ligands retained to the NC surface. During the stripping procedure the Lewis acid BF_3 forms a physisorbed $[OAc:BF_3^-]^-$ with the carboxylate terminus of the bound oleyl oleate ligands that is in a dynamic equilibrium with DMF and is responsible for the surface stabilization during the stripping procedure. Because an excess of BF_3 is added, the physisorbed $[OAc:BF_3^-]^-$ undergoes a disproportionate reaction to form a neutral $OAc_x(B_yF_z)$ species which is lost during the hexane washing step, and BF_4^- serves as an elec-
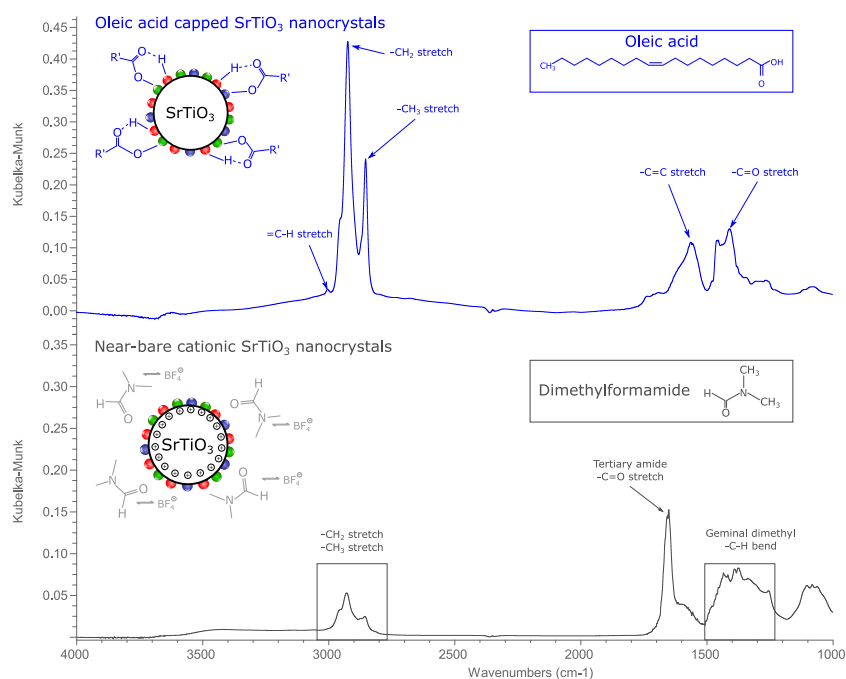
Figure 8: (top) oleic acid capped $SrTiO_3$ nanocrystals and (bottom) ligand stripped $SrTiO_3$ nanocrystals electrostatically stabilized by BF_4^- and co-stabilized by DMF.

trostatic stabilizer for the near-bare cationic surface. DMF and BF_4^- are in dynamic equilibrium with the cationic surface which explains the occurrence of DMF in the stripped NCs FTIR spectrum. The NCs also retained their monodispersity and non-agglomeration behaviour after the ligand stripping procedure, which is confirmed through DLS and TEM measurements (figure 9). A TGA measurement (see supporting information) was performed on the sample to determine the total yield and and check wether all organic ligands were stripped of the surface. After a thermal treatment to 1000 °C for 4 hours, the total yield was calculated at 20.22%. Furthermore, The TGA curve indicated that 23% of organic material was still present on the NC surface.
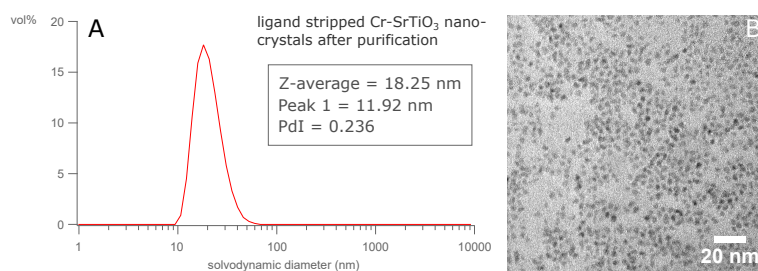
Figure 9: (A) DLS spectrum of ligand stripped Cr-doped $SrTiO_3$ nanocrystals, (B) TEM image of ligand stripped Cr-doped $SrTiO_3$ nanocrystals.

3.3   Mesoporous nanocrystal framework

The as-synthesized mesoporous NC framework should allow the retainment of a large surface area whilst providing the structural stability that is desired for photocatalytic materials. The Brunauer-Emmett-Teller (BET) surface area and pore shapes of both the $SrTiO_3$ and Cr-doped $SrTiO_3$ frameworks were determined through N_2 adsorption-desorption. The resulting isotherm plots are displayed in figure 10. A significant increase in BET surface area is observed for the

Cr-doped $SrTiO_3$ NCs (65.8215 m^2/g) as opposed to the undoped $SrTiO_3$ NCs (27.2723 m^2/g). Bi et al., for example, reported BET surface area values for undoped $SrTiO_3$ (30.7 m^2/g) and Cr-doped $SrTiO_3$ (54.3 m^2/g) particles that are about 300 nm in size and not formed into a NC framework.[11] The BET surface area results presented in this work thus are very promising. The N_2 adsorption-desorption isotherms also show a hysteresis loop which indicate the pore shape to be slit-shaped for the undoped $SrTiO_3$ NC framework (H3) and a combination between slit-shaped and cylindrical for the Cr-doped $SrTiO_3$ NC framework.
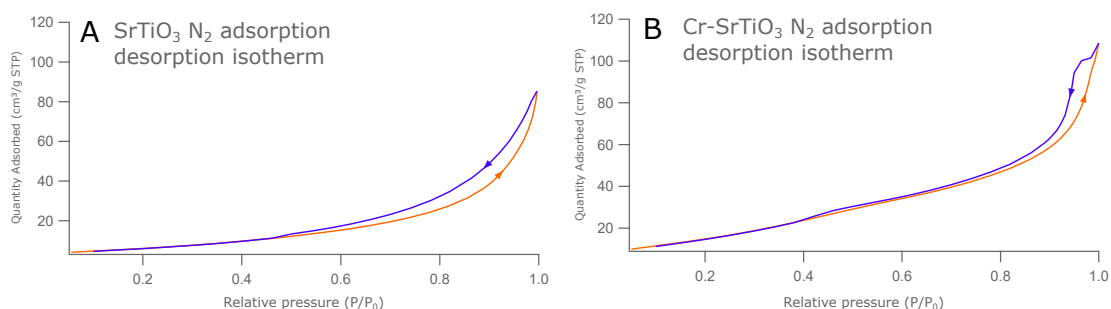
Figure 10: (A) N_2 adsorption-desorption isotherm of mesoporous $SrTiO_3$ nanocrystal framework, and (B) N_2 adsorption-desorption isotherm of mesoporous Cr-doped $SrTiO_3$ nanocrystal framework.

3.4 Photocatalytic tests

Figure 11 represents the UV-VIS spectra of the samples taken during the methylene blue (A) and methylene orange degradation reaction (B). A detail of the wavelength region ranging from 458 to 466 nm is shown for the methylene orange spectrum (figure 11.B). Even though no significant degradation of the organic dye is witnessed, a small decrease in absorbance is observed, A = 0.635 at 0 minutes to A = 0.619 after 210 minutes. This decrease in absorbance is however not significant enough to claim that the synthesized Cr-doped $SrTiO_3$ NC framework aids in the photodegradation of methylene orange. The detail presented in the methylene blue spectrum (figure 11.A) also suggests that the synthesized Cr-doped $SrTiO_3$ NC framework does not contribute to the photodegradation of methylene blue. The small variations in absorbance can probably be attributed to the sampling method which is non-quantitative and could lead to small differences in the UV-VIS spectra.
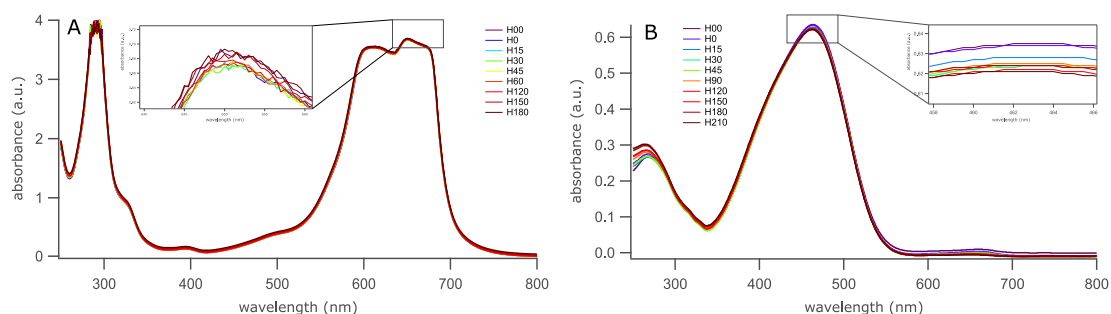

Figure 11: (A) detail of UV-VIS measurements at $\lambda = 650$ nm during the degradation reaction of methylene blue with Cr-doped $SrTiO_3$ (B) detail of UV-VIS measurements at $\lambda = 463$ nm during the degradation reaction of methylene orange with Cr-doped $SrTiO_3$.

4   Conclusion

The synthesized Cr-doped SrTiO$_3$ NC frameworks thus did not display photocatalytic activity in the photodegradation of methylene blue and methyl orange under UV-light irradiation. A possible explanation for this photocatalytic inactivity could be that the thiol containing BCP end groups inhibit the photocatalytic properties of the SrTiO$_3$ NCs. Another reason could be that the synthesized NCs were too small in size, which may have led to a predominantly amorphous NC shell that obstructs effective transport of charge carriers to the surface adsorbed species and/or may have limited adsorption of reactants to the surface. A third possibility is that the NCs are so small in size that the bandgap energy increases due to the disappearance of quantized energy levels in the Ti-3d orbitals and O-2p orbitals. However, no final conclusion as to why the Cr-doped SrTiO$_3$ NC frameworks did not exhibit photocatalytic properties can be made as further research is needed to verify or disprove these hypotheses. The synthesized Cr-doped SrTiO$_3$ NC frameworks showed promising results in terms of BET surface area as compared to the undoped SrTiO$_3$ NCs. This increase in BET surface area can be attributed to variations in pore periodicity and pore size distribution of the Cr-doped SrTiO$_3$ NC frameworks as compared to the undoped SrTiO$_3$ NC frameworks. Future research is necessary to characterize the NC frameworks and optimize the mesoporous material in terms of pore periodicity, pore shape and pore size distribution. That being said, the assembly of the synthesized SrTiO$_3$ and Cr-doped SrTiO$_3$ NCs into mesoporous NC frameworks presents a promising application field for this photocatalyst.
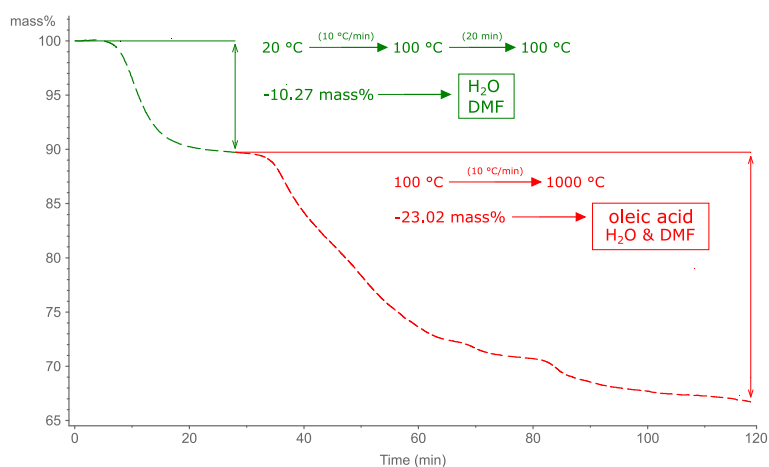
5   Supporting information

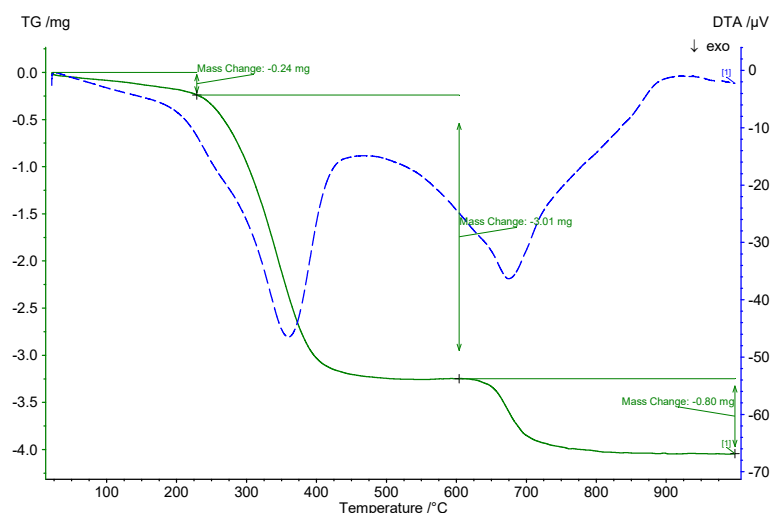**Figure 12:** TGA curve of near-bare, cationic SrTiO$_3$ nanocrystals.

Figure 13: TGA curve of as-synthesized $SrTiO_3$ nanoparticles coated with free unbound trioctylphosphine oxide, protonated trioctylphosphine oxide, and di-n-octylphosphinate bound to the surface. Di-n-octylphosphinate is thermally degraded in the temperature region from 600 $^\circ$C to 700 $^\circ$C.

<u>Chemicals</u>

Strontium (Sigma - 99.9%), titanium isopropoxide (Sigma - 97%), 2-methoxyethanol (Sigma - 99.9%), chromium acetylacetonate (Sigma - 97 %), acetonitrile (ROTIPURAN - 99.5%), toluene (VWR chemicals - 90%), oleic acid (Sigma - 90%), n-octylamine (Acro organics - 99%), acetone (VWR chemicals - 90%), hexane (Sigma - 95%), dimethylformamide (ROTISOLV - 99.5%), boron trifluoride diethyl etherate (Acros organics - 48%), ethanol (VWR chemicals - 99.8%), $PDMA_{8,3k}$-b-PS_{33k} (in-house synthesis), methylene blue (Sigma - 82%), methylene orange (Sigma - 85%) were used without purification. Trioctylphosphine oxide (STREM chemicals - 90%) was recrystallised in acetonitrile before use.

References

[1] Intergovernmental Panel on Climate Change. *Climate change 2014: mitigation of climate change*, volume 3. Cambridge University Press, 2015.

[2] JGJ Olivier, G Janssens-Maenhout, M Muntean, and JAHW Peters. Trends in global co2 emissions: 2015 report. pbl netherlands environmental assessment agency, the hague; european commission, joint research centre (jrc). *Institute for Environment and Sustainability (IES)*, 2015.

[3] Run Shi, Geoffrey IN Waterhouse, and Tierui Zhang. Recent progress in photocatalytic co2 reduction over perovskite oxides. *Solar RRL*, 2017.

[4] Elham Karamian and Shahram Sharifnia. On the general mechanism of photocatalytic reduction of co2. *Journal of CO2 Utilization*, 16:194–203, 2016.

[5] Wenhui Li, Haozhi Wang, Xiao Jiang, Jie Zhu, Zhongmin Liu, Xinwen Guo, and Chunshan Song. A short review of recent advances in co2 hydrogenation to hydrocarbons over heterogeneous catalysts. *RSC Advances*, 8(14):7651–7669, 2018.

[6] Yi Ma, Xiuli Wang, Yushuai Jia, Xiaobo Chen, Hongxian Han, and Can Li. Titanium dioxide-based nanomaterials for photocatalytic fuel generations. *Chemical reviews*, 114(19): 9987–10043, 2014.

[7] Wei Wang, Moses O Tadé, and Zongping Shao. Research progress of perovskite materials in photocatalysis-and photovoltaics-related energy conversion and environmental treatment. *Chemical Society Reviews*, 44(15):5371–5408, 2015.

[8] Peilin Liao and Emily A Carter. New concepts and modeling strategies to design and evaluate photo-electro-catalysts based on transition metal oxides. *Chemical Society Reviews*, 42(6):2401–2422, 2013.

[9] Sheng Zeng, Piyush Kar, Ujwal Kumar Thakur, and Karthik Shankar. A review on photocatalytic co2 reduction using perovskite oxide nanomaterials. *Nanotechnology*, 29(5): 052001, 2018.

[10] Markus Niederberger, Georg Garnweitner, Nicola Pinna, and Markus Antonietti. Nonaqueous and halide-free route to crystalline batio3, srtio3, and (ba, sr) tio3 nanoparticles via a mechanism involving c- c bond formation. *Journal of the American Chemical Society*, 126(29):9120–9126, 2004.

[11] Yiqing Bi, Muhammad Fahad Ehsan, Yan Huang, Jiarui Jin, and Tao He. Synthesis of cr-doped srtio3 photocatalyst and its application in visible-light-driven transformation of co2 into ch4. *Journal of CO2 Utilization*, 12:43–48, 2015.

[12] Samsun Nahar, MFM Zain, Abdul Amir H Kadhum, Hassimi Abu Hasan, and Md Riad Hasan. Advances in photocatalytic co2 reduction with water: A review. *Materials*, 10(6): 629, 2017.

[13] Huaqiao Tan, Zhao Zhao, Wan-bin Zhu, Eric N Coker, Binsong Li, Min Zheng, Weixing Yu, Hongyou Fan, and Zaicheng Sun. Oxygen vacancy enhanced photocatalytic activity of pervoskite srtio3. *ACS applied materials & interfaces*, 6(21):19184–19190, 2014.

[14] S Rajesh Kumar, CV Abinaya, S Amirthapandian, and N Ponpandian. Enhanced visible light photocatalytic activity of porous lamno3 sub-micron particles in the degradation of rose bengal. *Materials Research Bulletin*, 93:270–281, 2017.

[15] Murid Hussain, Raffaela Ceccarelli, DL Marchisio, Debora Fino, Nunzio Russo, and Francesco Geobaldo. Synthesis, characterization, and photocatalytic application of novel tio2 nanoparticles. *Chemical Engineering Journal*, 157(1):45–51, 2010.

[16] Francisco Zaera. Nanostructured materials for applications in heterogeneous catalysis. *Chemical Society Reviews*, 42(7):2746–2762, 2013.

[17] Swetlana Schauermann, Niklas Nilius, Shamil Shaikhutdinov, and Hans-Joachim Freund. Nanoparticles for heterogeneous catalysis: new mechanistic insights. *Accounts of chemical research*, 46(8):1673–1681, 2012.

[18] Alessandro Lauria, Irene Villa, Mauro Fasoli, Markus Niederberger, and Anna Vedda. Multifunctional role of rare earth doping in optical materials: Nonaqueous sol–gel synthesis of stabilized cubic hfo2 luminescent nanoparticles. *ACS nano*, 7(8):7041–7052, 2013.

[19] Katrien De Keukeleere, Sofie Coucke, Els De Canck, Pascal Van Der Voort, Fabien Delpech, Yannick Coppel, Zeger Hens, Isabel Van Driessche, Jonathan S Owen, and Jonathan De Roo. Stabilization of colloidal ti, zr, and hf oxide nanocrystals by protonated tri-n-octylphosphine oxide (topo) and its decomposition products. *Chemistry of Materials*, 29(23):10233–10242, 2017.

[20] Evelyn L Rosen, Raffaella Buonsanti, Anna Llordes, April M Sawvel, Delia J Milliron, and Brett A Helms. Exceptionally mild reactive stripping of native ligands from nanocrystal surfaces by using meerweins salt. *Angewandte Chemie International Edition*, 51(3):684–689, 2012.

[21] Sean E Doris, Jared J Lynch, Changyi Li, Andrew W Wills, Jeffrey J Urban, and Brett A Helms. Mechanistic insight into the formation of cationic naked nanocrystals generated under equilibrium control. *Journal of the American Chemical Society*, 136(44):15702–15710, 2014.

[22] RH Mitchell, AR Chakhmouradian, and PM Woodward. Crystal chemistry of perovskite-type compounds in the tausonite-loparite series,(sr 1- 2 x na x la x) tio 3. *Physics and Chemistry of Minerals*, 27(8):583–589, 2000.

[23] Przemysław Kowalik, Danek Elbaum, Jakub Mikulski, Krzysztof Fronc, Izabela Kamińska, Paulo C Morais, Paulo Eduardo De Souza, Rodrigo Barbosa Nunes, Fabiane Hiratsuka Veiga-Souza, Grzegorz Gruzeł, et al. Upconversion fluorescence imaging of hela cells using ros generating sio 2-coated lanthanide-doped nayf 4 nanoconstructs. *Rsc Advances*, 7(48): 30262–30273, 2017.

Table of Contents

Everything is theoretically impossible, until it is done.

Robert A. Heinlein

Chapter 1

Introduction

1.1 Background

The rapid consumption of fossil fuels and inherent production of the greenhouse gas (GHG) carbon dioxide (CO_2) is one of the key challenges our society faces in the 21st century. CO_2 emission by anthropogenic sources amounts to 76%[1] of global GHG emissions and it is estimated that 35 Gt of CO_2 is released every year by large fossil fuel facilities, biomass energy facilities and other major CO_2-emitting industries.[2] Although global investment in renewable energy sources like solar and wind energy are taking the lead, fossil fuels still account for 86% of the global energy production.[3] The problem does not only constitutes itself in residential and industrial energy consumption, but also includes transportation as a major CO_2 emission source, amounting to 20.5% of global CO_2 emissions. Hybrid and fully electric vehicles are already on the market and offer an impressive action radius and price range, but are still nowhere near perfect due to the low distribution of electrical charging locations and primary dependency on fossil-fuel generated electricity. At the current rate of consumption, it is estimated that the world's oil and natural gas reserves will be depleted in 50 years and coal reserves in 115 years. Furthermore, global energy needs are expected to increase by 30% by 2040 due to population increase, global economy growth and urbanisation.[3] As the current production capacity of renewable energy sources is far from supporting global energy demand, it is clear that depletion of fossil fuel sources presents a major problem for the successful propagation of our industrial society.

Despite the depletion of fossil fuels becoming a pressing issue 50-100 years from now, a more imminent threat originates from global CO_2 emission into the atmosphere

and subsequent warming of the planet: climate change. Since the 1950s, CO_2 levels in our atmosphere have risen from about 310 ppm to an average of 408.05 ppm in January 2018 (Manau Loa observatory). Global average temperature has risen by 0.9 °C as compared to pre-industrial temperatures and the effects are already visible as glaciers are retreating,[4] ice sheets are diminishing, and sea levels are rising. The majority of climate scientists agree that the rise in CO_2 levels in the atmosphere is caused by anthropogenic activity and that this increase plays a role in global warming.[5] However, not all scientists agree that CO_2 is the main contributor to global warming as H_2O exhibits a wider absorption spectrum and is more abundant in the atmosphere as compared to CO_2.[6] Still, the increase in atmospheric CO_2 contributes to global warming because it absorbs wavelengths of thermal energy that H_2O does not, thereby narrowing the window through which thermal radiation can escape the planet's atmosphere.[7]

One of the current routes to reduce CO_2 emissions is focussed on Carbon Capture and Utilisation (CCU), which aims to mitigate climate change by capturing CO_2 and utilising it into industrial processes, or converting it into useful hydrocarbons. CCU has the potential to produce value-added products that have a market and can generate a profit. Developing CO_2-based production routes for base chemicals allow to reduce the dependency of fossil carbon sources of the chemical industry. The use of alternative fuels synthesized from CO_2 as a raw material presents a novel renewable energy source which may ease the transition from a petrochemical-based industry to a renewable energy-based industry.

In nature, CO_2 conversion to useful carbohydrates occurs in plants in extremely mild conditions through photosynthesis. Photosynthesis is a biological process requiring multiple reactions to take place which rely on the cooperation of different catalysts within complex metabolic pathways. Photocatalysis can be regarded as an extension to artificial photosynthesis were the range of chemical products is extended beyond carbohydrates and oxygen through the use of a variety of simple or exotic catalysts. Using natural sunlight to drive the process to completion requires no additional input of energy and thus presents a sustainable CO_2 conversion route. Key to the success of photocatalytic CO_2 conversion is the development and use of effective and cheap catalysts.

Semiconductor materials are important materials for these photocatalysis reactions,

and can also be applied in photo optics and electronic devices.[8] One of the most widely studied class of semiconductor materials for photocatalytic CO_2 conversion are transition metal oxides due to their high activity, stability and low cost. Perovskite oxides (PO's) in particular lend themselves as great photocatalyst materials because of their great flexibility in composition and structure. One type of PO, Strontium titanate ($SrTiO_3$), exhibits excellent charge transport properties for photocatalytic reactions and, by doping the material with alkali, earth-alkaline or transition metals, the bandgap and CO_2 adsorption properties can be manipulated to enhance CO_2 reduction.[9]

The reactivity of heterogeneous catalysis depends on the elemental composition of the catalyst material as well as the surface area that is free for reaction. In recent years, nanoparticles (NPs) have been gaining increased interest for this application because of the unique physical and chemical properties related to their small size. Especially NPs built in mesoporous frameworks have shown impressive activity and stability retainment over multiple reaction cycles whilst allowing various manipulations on pore sizes to be made.[10]

1.2 Objective thesis

The objective of this master dissertation is the synthesis of chromium doped $SrTiO_3$ nanocrystals (NCs) that can be used as a photocatalyst in CO_2 reduction applications and for the degradation of organic dyes. Pristine $SrTiO_3$ is only active under UV light irradiation and thus additional energy is required for its effective use. By doping the photocatalyst with Cr^{3+} the light harvesting properties are improved, hence pulling the optically active region to the visible light spectrum, thereby improving the catalytic performance of the photocatalyst.[11] The scope of this research can be divided into three main domains: synthesis and stabilisation of Cr-doped and undoped $SrTiO_3$ NCs, processing of aforementioned NCs into mesoporous NC frameworks, and photocatalytic tests on the synthesized photocatalyst.

The first part of the thesis focusses on synthesizing Cr-doped and undoped $SrTiO_3$ NCs that stand out in terms of monodispersity, uniformity, crystallinity and stability. To obtain these material properties, trioctylphosphine oxide (TOPO) was used both as a solvent and a structure directing agent as it allows for a superior reaction

control.[12] The as-synthesized NPs are non-agglomerated, highly crystalline, have a size of $\pm$ 3 nm, and are stable in toluene requiring no additional surfactants.

Secondly, we aim to process the NPs into 3D ordered mesostructures through the use of block copolymer (BCP) architecture directing agents. Before being able to arrange these NPs into a mesoporous network, the native ligands have to be stripped of the NPs surface to allow favourable interaction with the BCPs NC-tethering domain. Through the use of oleic acid (OAc)/n-octylamine (octAm) we are able to exchange the native TOPO ligands and TOPO derivatives for OAc. The OAc ligands can then be stripped from the surface through a facile BF_3:Et_2O stripping method in DMF developed by Doris et al.[13] Once the ligand stripped NC building units are obtained, the assembly of colloidal NC frameworks can be accomplished through the use of PDMA-b-PS BCPs. These BCPs contain a NC-tethering domain (PDMA) that interacts with the bare NC surface as if it were DMF molecules, and a pore-generating domain that controls the pore sizes in the NC framework.

The third and final part of the research assesses the photocatalytic properties and possible applications of the $SrTiO_3$ mesoporous frameworks. Cr-doped $SrTiO_3$ has been shown to convert CO_2 molecules mainly into CH_3OH and CH_4, that can in turn be used as a carbon feedstock or as a fuel source in several industrial processes. Other than the photocatalytic reduction of CO_2, doped $SrTiO_3$ can also be availed for the degradation of several organic dyes such as rhodamine B, methyl orange, and methylene blue; showcasing the versatile photocatalytic properties of the material.[14,15] The application of the photocatalyst as thin films is also briefly explored and the mesoporous layers are visualized through SEM analysis.

In summary, Cr-doped $SrTiO_3$ should exhibit enhanced light harvesting properties that can be applied towards abating further anthropogenic CO_2 emissions into the atmosphere. By Cr-doping we not only increase the optical properties of the photocatalyst, but an increased CO_2 adsorption is also expected induced by the oxygen vacancies in the crystal lattice. Through the careful design of a mesoporous network consisting of uniform, monodisperse, and highly crystalline $SrTiO_3$ NPs; we aim to increase the efficiency and CO_2 conversion rate of the photocatalyst whilst also providing structural and chemical stability in harsh reaction environments.

Chapter 2

Theoretical section

2.1 CO$_2$ predicament

Greenhouse gases (GHG) in the earth's atmosphere are critical to supporting life as they are transparent to most of the incoming solar radiation, yet absorb part of the outgoing radiation from escaping the atmosphere, retaining part of the surface heat. The most important GHG in the Earth's atmosphere include H$_2$O, CO$_2$, CH$_4$, N$_2$O and O$_3$.[16]

All atmospheric gases show a complex pattern of absorption to electromagnetic radiation, as can be seen in figure 2.1.1. H$_2$O, being the most abundant GHG, is the major contributor to global warming as it is the most absorbing GHG as compared to other GHG (See figure 2.1.1). However, H$_2$O is transparent to some wavelength regions, essentially leaving water vapor windows for thermal radiation to escape the atmosphere. The most important of these water vapor windows is located in the thermal infrared region starting from about 8 to 14 µm, with the center around 10 µm. CO$_2$ is a very strong absorber of thermal infrared energy, especially in the wavelength region from 12 to 15 µm. Thus, as atmospheric CO$_2$ levels increase, so does the absorbance of wavelengths of thermal radiation that would otherwise leave the atmosphere, resulting in an overall energy imbalance. Changes in the planet's energy balance do not take effect immediately but get delayed due to the tremendous heat capacity of the ocean serving as a buffer.[17] As a response to current anthropogenic GHG emissions, global temperature has increased by 0.9 °C and this number is expected to increase even further as the energy imbalance reaches a new equilibrium. As long as there is a net increase in GHG emissions, the world's energy equilibrium is continuously put off balance and the temperature will keep on rising.
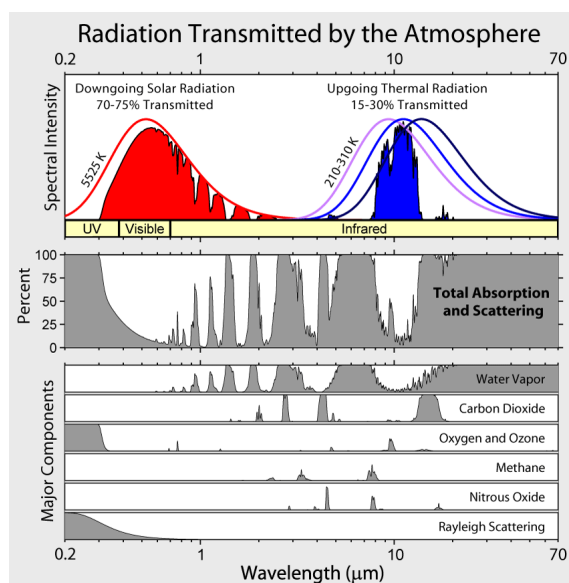
Figure 2.1.1: Absorption spectra of the most abundant greenhouse gases in earth's atmosphere.

Increased levels of CO_2 in our atmosphere are already leaving its imprint on our planet, as can be seen through the deteriorating state of coral reefs in our oceans (See figure 2.1.2). About one quarter of anthropogenically emitted CO_2 enters the ocean, where it reacts with H_2O to form H_2CO_3 and dissociates into HCO_3^- and H^+.[18] These protons can then further react with CO_3^{2-} ions in the water, reducing the rate of calcification of marine organisms and ultimately leading to erosion of coral reefs, as can be seen in figure 2.1.2.[19]

Natural CO_2 emissions occur through combustion of carbonaceous materials and volcanic activity, but the major contribution to CO_2 emissions in our atmosphere comes from anthropogenic sources. CO_2 enters the atmosphere through burning of fossil fuels (oil, coal and natural gas), solid waste, trees and wood products, and as a result of certain chemical reactions. The largest sources of CO_2 emissions in the United States in 2016 were electricity production (28%), transportation (28%), and industry (22%). The total share of CO_2 in US GHG emissions amounted to 81% in 2016.[21]

The reason why CO_2 is such a persistent GHG in our atmosphere is due to its double C=O bond which possesses a much higher bond energy (799 kJ/mol) as compared to C−C bonds, C−H bonds and C−O bonds (respectively 347 kJ/mol, 413 kJ/mol

Figure 2.1.2: Deterioration of the Great Barrier Reef due to ocean acidification and heating caused by anthropogenic activites. [20]

and 358 kJ/mol). [9] Furthermore, CO_2 exhibits a large energy gap between its LUMO and HOMO (13.7 eV) and a large electron affinity (-0.6 $\pm$ 0.2 eV), which make it an inactive molecule. [22] As a result of this thermodynamic stability, transforming CO_2 into hydrocarbons and intermediates requires harsh reaction conditions. Current state of the art technologies that aim to mitigate CO_2 emissions focus either on carbon capture and storage (CCS) (e.g. geological storage, [23] mineral carbonation, [24] or ocean storage [25]) or carbon capture and utilization (CCU) (e.g. microalgae fixation for biofuel production, [26,27] use as a chemical feedstock, [28] or for enhanced oil recovery purposes [28,29]). CCS technology has the most potential to reduce global CO_2 emissions but its wide deployment is limited due to the high economic cost and CO_2 leakage liabilities. CCU technologies on the other hand focus on utilizing CO_2 as a feedstock into various chemical processes to generate useful hydrocarbons and intermediates. This solution allows CO_2 to be treated as a commodity, rather than a waste product. [30] In the strive for a circular CO_2 economy, the large scale photocatalytic conversion of CO_2 into CH_4 and CH_3OH has received particular interest in the scientific community. [31]

2.2 Photocatalytic CO_2 reduction

Utilizing the energy of the sun combined with earth abundant semiconductor materials allow us to reduce CO_2 emissions in an economically viable way whilst generating hydrocarbons and intermediates to be used as a stable means of storing energy or as a chemical feedstock. Photocatalytic reduction of CO_2 using semicon-

ductor catalyst materials comprises three major steps: (1) absorption of photons with suitable energy and generation of electron-hole pairs, (2) separation and transportation of electron-hole pairs, and (3) chemical reaction with surface adsorbed species through charge carriers.[32] Concomitantly, an ideal photocatalyst must exhibit light harvesting properties, efficient charge separation/trapping capability, and contain CO_2 adsorption sites and acid centers.[33] The general reaction during artificial photosynthesis can be summarized as:

$$CO_2 + bH_2O \xrightarrow{h\nu} C_xH_yO_z(+O_2) \tag{2.2.1}$$
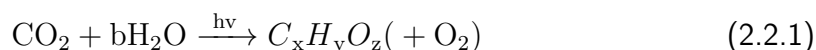
The first step in CO_2 reduction is chemisorption of CO_2 on the surface of the catalyst. The carbon atom of CO_2 is able to coordinate on the semiconductors transition metal center due to the electron deficiency in the carbonyl center.[34] This interaction results in a weakening of the C-O bonds and causes a remarkable bending of the coordinated CO_2 molecule, activating the molecule for subsequent reduction reactions.[35]

Reaction	E° (V)
$CO_2 + e^- \longrightarrow CO_2{}^-$	-1.9
$CO_2 + 2H^+ + 2e^- \longrightarrow HCO_2H$	-0.61
$CO_2 + 2H^+ + 2e^- \longrightarrow CO + H_2O$	-0.53
$CO_2 + 2H^+ + 4e^- \longrightarrow HCHO + H_2O$	-0.48
$2H^+ + 2e^- \longrightarrow H_2$	-0.41
$CO_2 + 6H^+ + 6e^- \longrightarrow CH_3OH + H_2O$	-0.38
$CO_2 + 8H^+ + 8e^- \longrightarrow CH_4 + 2H_2O$	-0.24
$H_2O + 2h^+ \longrightarrow \frac{1}{2}O_2 + 2H^+$	+0.82

Table 2.2.1: Electrochemical reactions involved in CO_2 reduction with their corresponding redox potentials.

When the semiconductor material absorbs photons of sufficient energy, electrons from the conduction band (CB) excite to the valence band (VB), creating an electron-hole pair inside the photocatalyst. If the bottom of the CB is located at a more negative potential than the reduction potential of CO_2 (-1.90 V), photogenerated electrons can act as reducing agents to convert CO_2 into various products such as HCOOH, HCHO, CH_3OH, and CH_4 as can be seen in table 2.2.1. Vice versa, when the top of the valence band is located at a higher oxidation potential than H_2O,
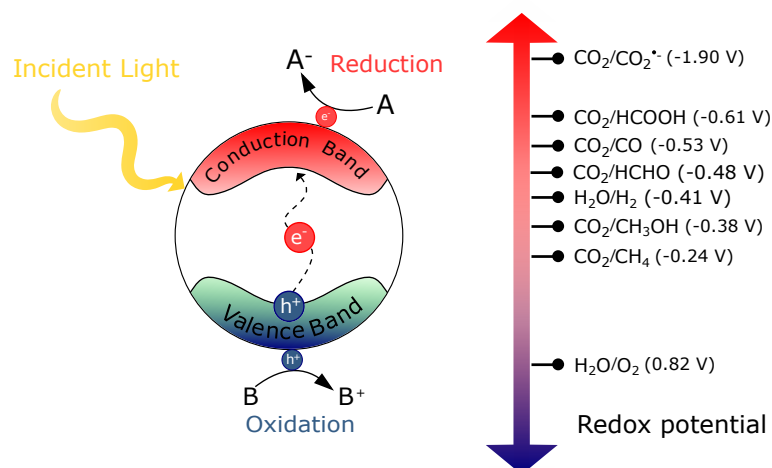
Figure 2.2.1: Photogenerated electrons and holes act as redox agents in the CO_2 reduction reaction.

photogenerated holes serve the role of oxidizing agents, oxidizing H_2O into H^+ and O_2 (see figure 2.2.1).[36] The generated electron-hole pairs can also recombine inside the photocatalyst without interacting with adsorbed species. Hence, delaying the charge carrier recombination time is vital for photocatalytic CO_2 reduction.[32]

Table 2.2.1 shows the various CO_2 conversion reactions that can occur when photocatalytically reducing CO_2. One-electron reduction of CO_2 is thermodynamically highly unfavourable due to its high negative reduction potential (-1.90 V at pH 7.00). Proton-assisted multi-electron reduction reactions are much more favourable thermodynamically owing to their lower reduction potential. Generally, H_2O is an ideal electron donor and hydrogen source for the reduction process, but problems may arise due to its ability to be both oxidized to O_2 ($E° = +0.82$ V), or reduced to H_2 ($E° = -0.41$ V). As CO_2 reduction requires multiple electrons as opposed to H_2O reduction, the latter is kinetically favoured over the thermodynamically favoured CO_2 reduction. Fortunately, by choosing the right photocatalyst able to spatially separate the photogenerated charge carriers, or by loading the photocatalyst with a suitable co-catalyst, this problem can be circumvented.[33,37] Photocatalyst materials composed of transition metal oxides and group IIIA metal oxides are the most widely studied materials for CO_2 reduction applications owing to their high catalytic activity, stability and low cost.[38–40] Perovskite-phase mixed metal oxide nanostructures in particular demonstrate excellent photocatalytic activity for CO_2 reduction applications and hence are at the scope of this research.[9,41]

2.3   Perovskite oxides

Perovskite oxides (PO) exhibit outstanding chemical and physical properties, including superconductivity,[42] magnetic properties,[43] ferroelectric abilities,[44] oxygen-transport,[45] and catalytic behaviour.[46] Its suitable band alignment allows an easier oxidation of H_2O at the VB and reduction of CO_2 at CB, facilitating the desired redox reactions over charge carriers recombination, as can be seen in figure 2.3.1. Due to PO lower bandgap energy as compared to other heterogeneous photocatalysts such as GeO_2 (5.5 eV), ZrO_2 (5.0 eV), or Ga_2O_3 (4.6 eV); PO can absorb a greater fraction of photons from incident solar radiation.[41] Furthermore, PO display greater charge carrier separation due to higher crystal lattice distortions as compared to binary oxides, leading to a greater photocatalytic capability.[47]
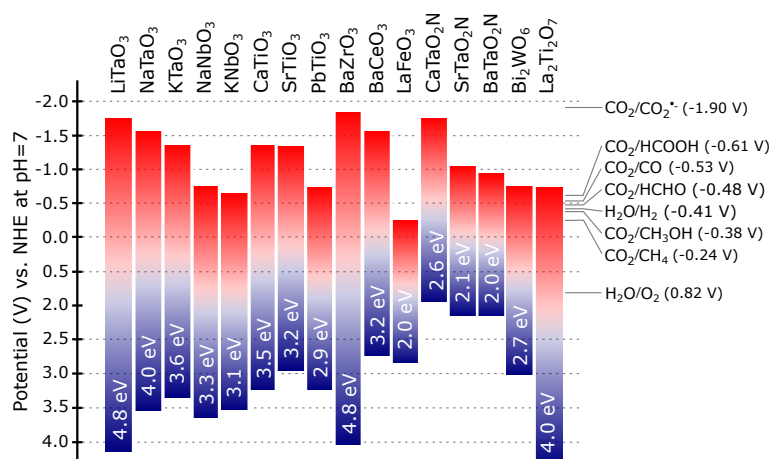
Figure 2.3.1: Energy band potentials and band gap energies of various perovskite oxides for photocatalytic applications relative to the redox potentials at pH 7 of various CO_2 reduction reactions.

PO show excellent thermal and hydrothermal stability which enable it to be used in high temperature gaseous or solid reactions, liquid reactions at room temperature, or under irradiation conditions.[48] In the last decade, much research has been devoted to PO for photocatalytic and photovoltaic processes including water splitting,[49] degradation of organic dyes,[50] and solar cells.[51] One such PO which exhibits a high potential for application in CO_2 photoreduction processes and organic dye degradation is strontium titanate.[52]

2.3.1   Strontium titanate
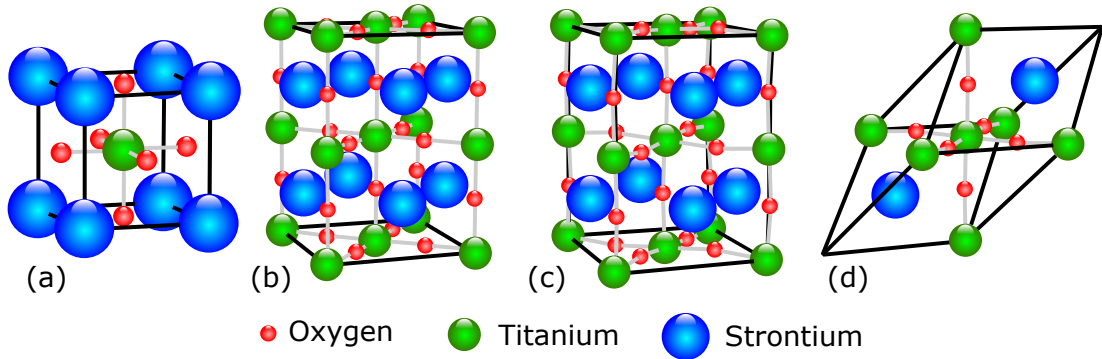
Figure 2.3.2: Crystal lattices of (a) cubic, (b) tetragonal, (c) orthorombic, or (d) rombohedral strontium titanate

Strontium titanate, which has the formula $SrTiO_3$, exhibits the typical ABO_3 perovskite crystal structure, where A and B are cations. $SrTiO_3$ can appear in either cubic, tetragonal, orthorombic, or rombohedral form (see figure 2.3.2); exhibiting the cubic form at standard conditions. In the cubic form, the B cations, or Ti^{4+} cations in $SrTiO_3$, are sixfold coordinated with O^{2-} anions. The A cations, or Sr^{2+} cations, occupy the holes created by 8 TiO_6 octahedra, thus are 12-fold coordinated with oxygen atoms. Within the TiO_6 octahedra, the Ti-3d orbitals hybridize with the O-2p orbitals to form a covalent bond. The bond between Sr^{2+} and O^{2-} is of ionic nature. As a result the $SrTiO_3$ crystal structure will exhibit a mixed ionic-covalent character, rendering it with interesting electrical properties.[53]

$SrTiO_3$ is a semiconductor with a bandgap energy of 3.2 eV. Because the bandgap energy is far larger than the thermal excitation energy (25 meV), $SrTiO_3$ is only able to generate electron-hole pairs through photoexcitation. The energy of the incident photons needed to excite valence electrons from the VB to the CB can be calculated by the following formula:

$$E(eV) = \frac{1.2398}{\lambda(\mu m)} \tag{2.3.1}$$

Thus, in the case of $SrTiO_3$ with E_g = 3.2 eV, the incident light can have a maximum wavelength of 387 nm to excite electrons from the VB. Larger wavelengths will result in electron energies lower than 3.2 eV, and will not be able to excite them to the CB. Concomitantly, the valence electrons in $SrTiO_3$ can only be excited when irradiated with UV light (λ = 10-380 nm). As UV light only accounts for 4% of

sunlight, $SrTiO_3$ is far from an ideal CO_2 photocatalyst. A way to increase the photocatalytic application potential of $SrTiO_3$ is to pull the optically active region to the visible light region (λ = 380-780 nm), accounting for 43% of sunlight.[32] Following the formula 2.3.1 we can see that increasing the wavelength means decreasing the band gap energy. Decreasing the band gap energy can be realized by either raising the highest VB energy (E_V), by lowering the lowest CB energy (E_C), or by introducing discontinuous energy levels in the forbidden zone. Altering E_V or E_C only leads to small changes in E_g, and thus does not extend the optically active region much beyond the region of UV light. As we strive for an optimal optically active photocatalyst, a larger difference in E_g is desired. Introducing dopant elements that create mid gap states in the band gap region allow us to alter the light harvesting properties more accordingly to our needs, and is thus the preferred method.

2.3.2 Effect of doping

Various methods that influence bandgap properties have been reported for wide bandgap semiconductors, including quantum dot sensitization,[54] dye sensitization,[55] and element doping.[11] The latter being the preferred method for altering the CO_2 adsorbing and photon absorbing properties of PO due to its simplicity and economic advantage.[56]

Doping in $SrTiO_3$ can occur either at the A-site or at the B-site of the ABO_3 perovskite. The Sr^{2+} ion has an ionic radius of about 0.118 nm, whilst the Ti^{4+} ion has an atomic radius of 0.068 nm respectively. Doping of $SrTiO_3$ is done using transition metals with smaller electronegativity than the host material. Most transition metals with a lower electronegativity than Ti^{4+} have about the same ionic radius as Ti^{4+}. As a result, the ions will be more easily substituted in the Ti^{4+} regions rather than the Sr^{2+} regions. When an ion with a smaller ionic radius than Sr^{2+} is substituted into the A-site of $SrTiO_3$, the crystal plane distance d will decrease, increasing the 2θ value as can be calculated with Bragg's law (formula 2.3.2). The increase or decrease in 2θ values of the diffraction peaks are an indicator that the dopants are incorporated into the $SrTiO_3$ crystal lattice.[57]

$$2dsin(\theta) = n\lambda \tag{2.3.2}$$

For undoped $SrTiO_3$, the band gap is created by the occupied O-2p states creating

the VB, and the unoccupied Ti-3d states creating the CB.[58] The difference between these two bands is 3.2 eV. Incorporating a dopant element into $SrTiO_3$ can have two results on the electronic band structure: (1) formation of a mid gap state between CB and VB,[59] or (2) alter the VB and/or CB through mixing of the energy levels.[60] Cr-doped $SrTiO_3$ exhibits the highest performance in hydrogen evolution under visible light irradiation as compared to other element-doped $SrTiO_3$.[11] The visible light response is enhanced because Cr^{3+} introduces a new mid gap state that lies about 1.0 eV higher than the VB top of undoped $SrTiO_3$.[61] As a result, the bandgap is reduced to about 2.48 eV,[62] extending the optically active region to about 500 nm (as can be calculated with formula 2.3.1) which falls in the center of the visible light region (λ = 380-780 nm).

A change in electron-donor features and adsorptivity of the photocatalyst is also observed when foreign elements are introduced,[63] owing to the different electronegativity (EN) of the dopant elements. The neutral atom EN of Cr (X_0 = 1.66) is larger than that of Ti (X_0 = 1.54), but the EN metal ion for Cr^{3+} is equal to X_i = 11.62, as compared to Ti^{4+} with X_i = 13.86. By incorporating dopant elements with a smaller X_i than the central metal atom, the photocatalyst exhibits a better CO_2 adsorption capacity.[57]
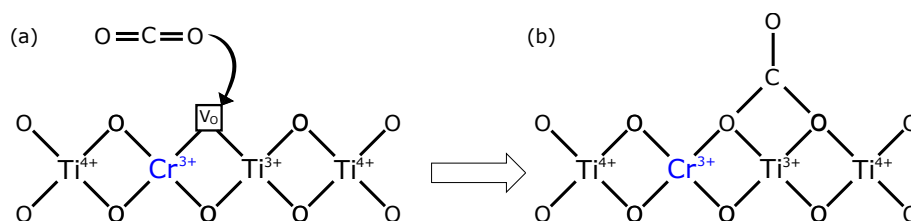
Figure 2.3.3: Illustration of the influence of Cr doping on $SrTiO_3$'s surface (a) Cr^{3+} induced surface oxygen vacancy on $SrTiO_3$, and (b) enhanced adsorption site for CO_2 molecules

Introducing oxygen vacancies in the photocatalysts surface allows retarding the recombination of photogenerated charge carriers, thereby enhancing the performance of the photocatalyst.[64,65] Surface oxygen vacancies can improve adsorption of surface species and can act as photoinduced charge traps, aiding charge transfer to the surface adsorbed CO_2.[66] Oxygen vacancies may be formed by changing the valence of the B-cation, either by heat treatment in oxidizing or reducing atmosphere, or via doping in the A-sublattice.[53] Alternative methods to induce surface oxygen vacancies in $SrTiO_3$ have also been reported by using $NaBH_4$ as an oxygen scavenger,[66] or through Ar^+ sputtering techniques.[67] In Cr-doped $SrTiO_3$, the creation of mid gap

states in the forbidden band, and oxygen vacancies on the photocatalyst surface (as can be seen in figure 2.3.3) contribute to the enhanced photon absorption and CO_2 adsorption of the photocatalyst.[68]

2.4 Nanocrystal synthesis

CO_2 photoreduction reactions occur at the surface of photocatalysts and thus a large surface area is beneficial for an increased photocatalytic performance. On the nanoscale, size and shape exert a strong influence on the chemical and physical properties.[69] Various studies have shown NPs to exhibit greater photocatalytic activity as compared to their bulk counterpart due to their large surface area, optical properties, and catalytic nature.[70–73] Several preparation methods exist for synthesizing NPs such as aqueous or non-aqueous, surfactant or surfactant free, and solid state or solvent based synthesis routes; each method having its own inherent benefits and disadvantages.

In solvent-based synthesis routes, molecular precursors are homogeneously dissolved and a large control over the particles morphology, crystallinity, surface properties, and thus agglomeration behaviour, is possible.[74] Aqueous synthesis routes generally exhibit a short reaction time, but produce NPs with a large particle size distribution and low degree of crystallinity.[75] Non-aqueous synthesis routes generally produce NPs which are highly crystalline directly after synthesis and do not require an additional calcination step to induce crystallinity.[74]

Furthermore, a differentiation can be made between surfactant-free and surfactant-containing nonaqueous synthesis routes. Surfactant-free nonaqueous synthesis routes generally produce highly crystalline NPs which agglomerate easily. The use of benzyl alcohol as a solvent is an example of a surfactant-free synthesis route, resulting in highly crystalline, yet agglomerated NCs.[76] The NPs can however be dispersed by using surfactants.[77] Surfactant containing synthesis routes have also been studied with a variety of group 4 metal oxides, producing highly crystalline, non-agglomerated NPs.[12] Quite recently, De Roo et al. published a paper where the surfactant tri-n-octylphosphine oxide (TOPO) was used as a solvent to synthesize TiO_2, ZrO_2 and HfO_2 NPs with pristine reaction control. The use of TOPO as a solvent proved to be beneficial in producing NPs that were highly monodisperse and crystalline, and

exhibited excellent scalability and colloidal stability.[12]
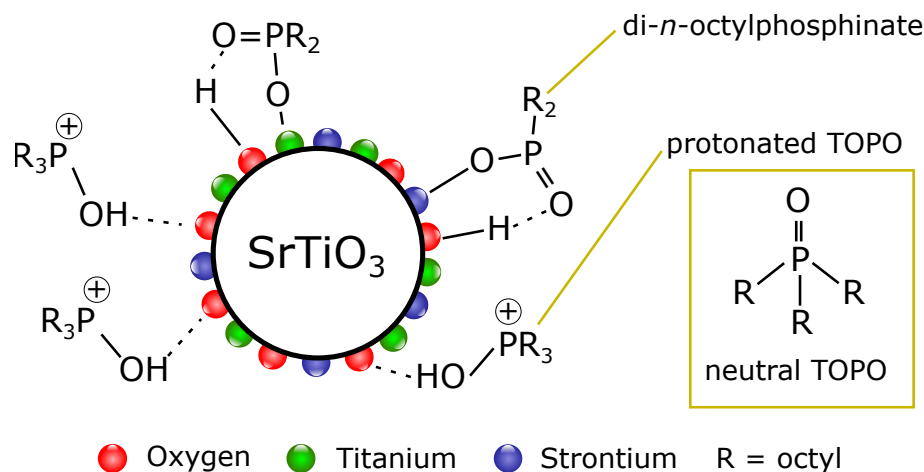
Figure 2.4.1: Complex TOPO shell of as-synthesized SrTiO$_3$ nanocrystals.

The dipolar phosphorus-oxygen head of TOPO attaches to the metal oxide whilst the apolar octyl groups render the molecule soluble in apolar solvents like chloroform and toluene. During NC growth, TOPO serves both as a solvent and a structure directing agent for the growing NPs. After synthesis the highly polar dipolar phosphorus-oxygen bond bind to the mixed metal oxides, and the octyl groups render it soluble in apolar solvent such as toluene and chloroform.[74]

2.5   Ligand coordination

The native coordinating ligands acquired during synthesis are necessary to exert control over the NC size, composition, morphology, and dispersibility; but are often not beneficial for the final application in terms of chemical behaviour, physical properties and catalytic activity.[78] As for SrTiO$_3$, with a surface resembling that of TiO$_2$ NCs, it is expected that the surface is covered with neutral TOPO, protonated TOPO and di-n-octylphosphinate ligands.[12] Because the large apolar chains of the TOPO derivatives shield the NC surface from adsorbing species and thereby lower the catalytic activity, a ligand exchange must be performed. Bare NC surfaces in particular are desirable for many advanced energy applications including light-emitting diodes,[79] field-effect transistors,[80] photovoltaics,[81] and mesoporous applications.[13]

2.5.1 Ligand classification

The Covalent Bond Classification (CBC) provides a useful framework to describe NC-ligand binding, categorizing ligands either as L-, X- or Z-type ligands depending on the number of electrons the neutral ligands contribute to the NC-bond, respectively 2, 1 or 0. L-type ligands are neutral two-electron donating Lewis bases which bond with the surface metal atoms. Z-type ligands are neutral electron accepting Lewis acids that bond to the surface non-metal atoms. The one-electron X-type ligands donate one electron to the NC-bond and can either bind to metals (X^-) or non-metals (X^+). A special kind of X-type ligand is the OAc ligand, which can be classified as an X2-type ligand. Dissociative adsorption of OAc results in an anionic $RCOO^-$ ligand (X^--type) binding to the surface metal, and a cationic H^+ ligand (X^+-type) binding to the surface non-metal. Hence exhibiting exchange characteristics similar to the L-type ligands.
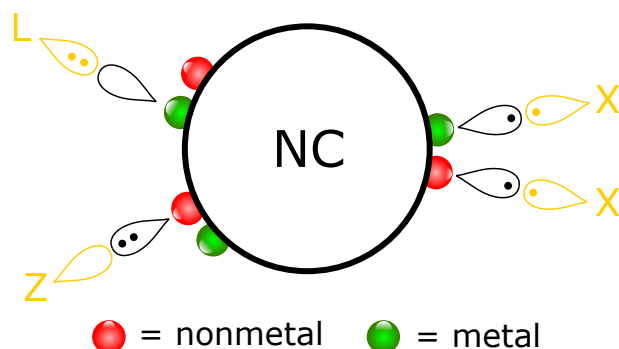
Figure 2.5.1: Three types of ligands can bind to the NC surface according tot the CBC classification: L-type ligands that bind with metals, Z-type ligands that bind with non-metals, and X-type ligands that bind with both metals and non-metals.

2.5.2 Ligand exchange and stripping

In order to obtain bare $SrTiO_3$ surfaces, the X-type TOPO ligands di-n-octylphosphinate, neutral TOPO and protonated TOPO have to be exchanged first with the X_2-type ligand OAc aided by octAm.[82] Addition of octAm to a TOPO-capped ZrO_2 NC dispersion in chloroform has shown to liberate neutral TOPO molecules from the surface by deprotonating the $[HO-PR_3]^+$ ions, and partially desorbing di-n-octylphoshinate as an n-octylammonium ion pair (figure 2.5.2). When adding OAc with the octAm, the carboxylate functions of OAc displace the di-n-octylphosphinate ligands and neutral TOPO ligands are more completely removed. The complex TOPO shell of the as-synthesized $SrTiO_3$ NCs can thus be simplified to a complete

carboxylate shell.[12]
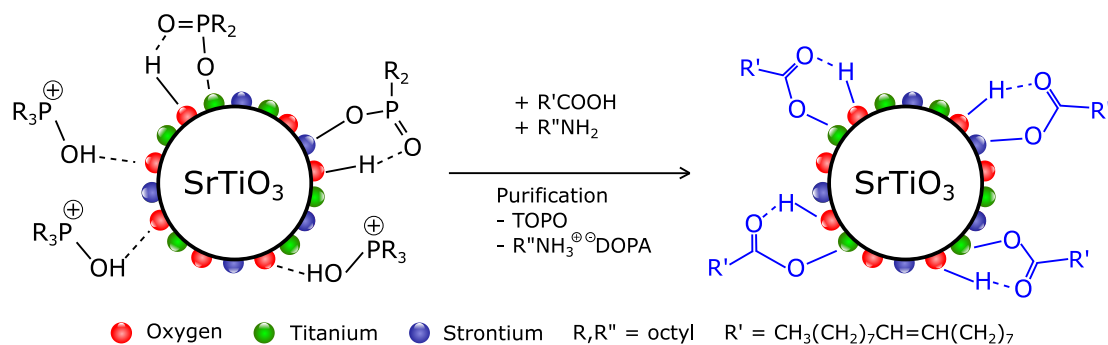
Figure 2.5.2: Exchanging TOPO capped nanocrystals through the oleic acid/n-octylamine ligand exchange procedure.

The oleate-passivated NC surfaces can then be stripped from their carboxylate shell by an extremely mild stripping procedure using $BF_3:Et_2O$. The Lewis acid BF_3 forms a physisorbed $[OAc:BF_3]^-$ adduct with the carboxylate terminus of the bound oleate ligands that is in continuous equilibrium during the stripping procedure and is responsible for the surface stabilization. In the presence of excess BF_3, the anionic $[OAc:BF_3]^-$ undergoes disproportionation reactions leading to the loss of neutral $OAc_x(B_yF_z)$ species and the formation of BF_4^-, which stabilize the cationic surface of the naked NCs through electrostatic stabilization and allow the NCs to be dispersed in polar media such as DMF and DMSO.[13]
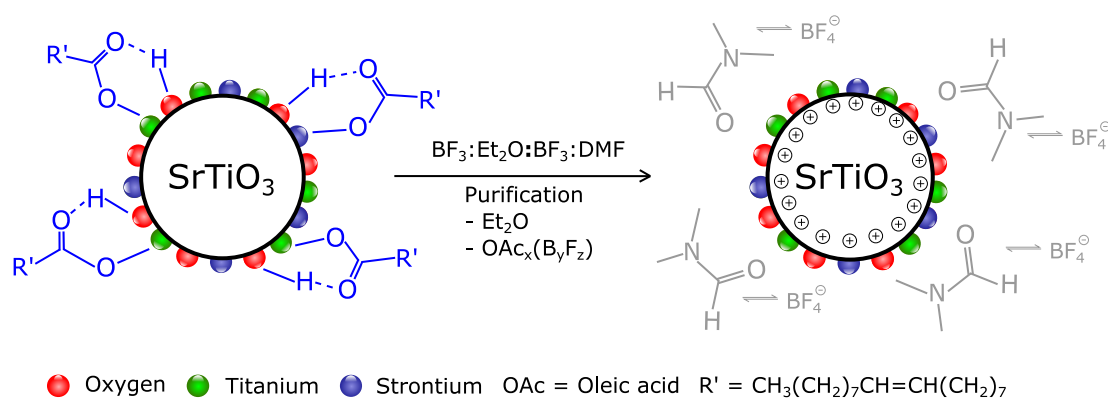
Figure 2.5.3: Stripping of oleic acid capped nanocrystals by a $BF_3:Et_2O$ treatment to result in cationic nanocrystals under equilibrium control with DMF and BF_4^- ions.

2.6 Mesoporous SrTiO$_3$ thin films and powders

Mesoporous materials are defined as materials with intermeditate pore sizes of 2 to 50 nm and are often applied in heterogeneous catalysis. Three-dimensional mesoporous frameworks consisting of mixed metal oxide NC building blocks are excellent materials for catalytic applications due to their large pore size, high surface area, and thermal and chemical stability.[83] Ligand stripped NCs aided by BCP structure-directing agents in particular produce mesoporous materials with exceptional control over the pore size, wall thickness, local ordering, and uniformity of the pores. Key to the controllability of these mesostructures lies in the diversity of BCPs that can be made. In order to make these mesostructured materials, BCPs which strongly adsorb to the naked cationic NC surfaces have to be used.[84] Buonsanti et al. synthesized BCPs with a NC-tethering domain made out of poly(N,N-dimethylacrylamide) (PDMA) and a porogenic polystyrene domain (PS) which succesfully resulted in the synthesis of mesoporous NC frameworks out of TiO$_2$ NCs.[85]
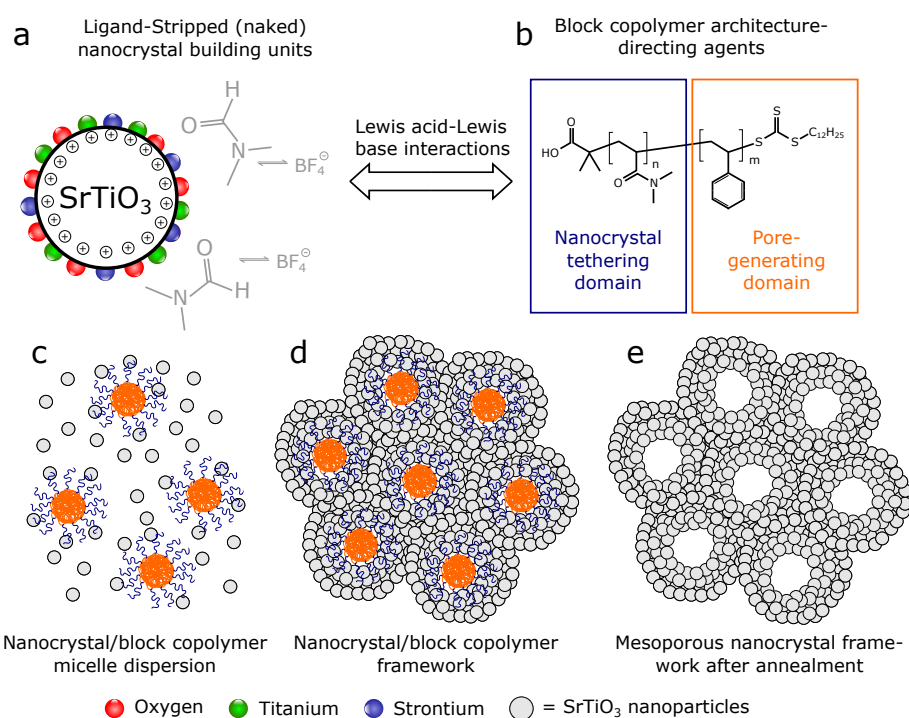
Figure 2.6.1: (a) naked cationic SrTiO$_3$ nanoparticles, (b) PDMA-b-PS block-copolymer, (c) nanocrystal/block-copolymer dispersion, (d) nanocrystal/block-copolymer framework, and (e) mesoporous nanocrystal framework after annealing.

When the BCPs are introduced into a polar solvent, the dipolar BCP will form a micellar solution with a PS center and a PDMA corona. Upon addition of the NCs into

the micellar solution, the NCs adsorb to the PDMA corona which ultimately form the walls of the NC framework. The adsorption strength of PDMA to NC surfaces is owed to the similar chemical structure as DMF, thereby mimicking the dynamic adsorption interactions of DMF at the cationic NC surfaces.[78] The pore sizes, wall thickness and pore structure can be finely tuned by altering the M_w of the PS block, the M_w of the PDMA block, and the M_w ratio of both BCP domains respectively. Pure mesoporous thin films or powders are obtained by thermal treatment of the hybrid mesoporous BCP-NC frameworks.[85]

2.7 SrTiO$_3$ photocatalytic tests

SrTiO$_3$ has been the scope of many researches due to its excellent physical and chemical properties, and acts as a photocatalyst in water-splitting reactions,[62] organic pollutant photodegradation processes,[86,87] and CO$_2$ photoreduction reactions.[88] The perovksite oxide has been utilized in several, UV light-driven, degradation reactions including the degradation of rhodamine B (RhB) and methyl orange (MO); showcasing its versatile photocatalytic application potential.[14] Furthermore, Rahman et al. showed that by doping SrTiO$_3$ with Cu, the perovskite material could be used to degrade methylene blue upon visible light irradiation, reporting a 66% degradation within a timespan of 2 h.[15] The successful degradation of organic dyes under visible light irradiation can thus be utilized as a first indicator of the enhanced photocatalytic properties of the material and can be measured by monitoring the colour change of the dyes through UV-Vis measurements.

In terms of CO$_2$ reduction, the perovskite oxide is often studied as a co-catalyst in composites (e.g. TiO$_2$/SrTiO$_3$,[89] BiVO$_4$/SrTiO$_3$[90]), but almost no publications focus on refined SrTiO$_3$ as a photosensitizer in CO$_2$ reduction reactions.[91] Pristine SrTiO$_3$ is only catalytically active upon UV light irradiation and thus not an ideal photocatalyst. By introducing dopant elements into the material however, the light harvesting properties can be enhanced. Bi et al. proved this change in optical properties by incorporating Cr^{3+} dopant elements into the SrTiO$_3$ perovskite oxide crystal structure which resulted in a shoulder formation at around 500 nm and a broad sub-peak at around 610 nm in the UV-Vis absorption spectra (as can be seen in figure 2.7.1), thus successfully enhancing the optical properties of the material. The shoulder in the UV-Vis spectrum can be devoted to Cr, introducing new mid gap states into the bandgap which elevates the VB and lowers the E_g;[92] the broad-sub
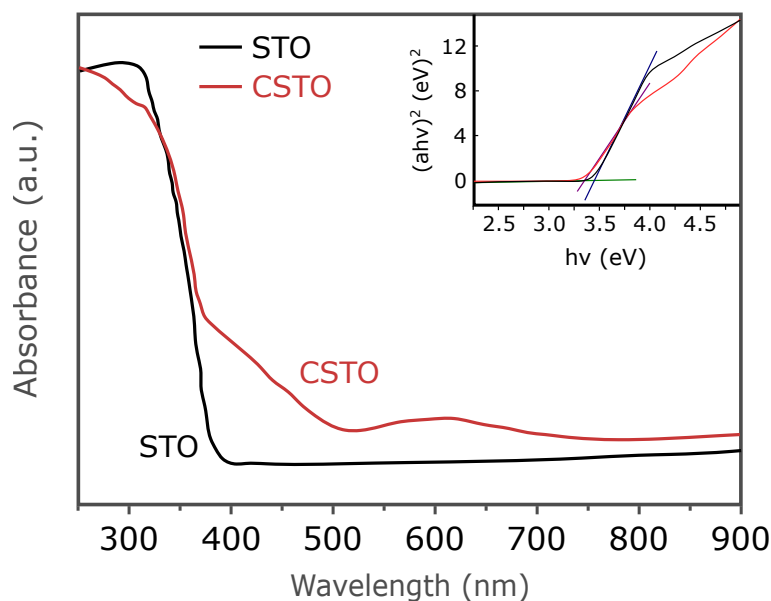
Figure 2.7.1: UV-Vis absorption spectra of pristine $SrTiO_3$ and Cr-doped $SrTiO_3$ as measured by Bi et al.[88]

peak is ascribed to oxygen vacancies creating new states.[93] Consequently, the optical properties of $SrTiO_3$ photocatalyst can be improved by doping with Cr^{3+} atoms and the enhanced light harvesting properties can be measured by UV-Vis measurements.

As the CO_2 reduction reaction can result in the formation of several reaction products depending on the choice of co-reagent,[22] measurement of the possible reaction products is less straightforward as compared to dye degradation experiments. Before devising a measurement system that monitors the CO_2 reduction reaction products, one must first define the co-reagent and physical state of the co-reagent. The most promising co-reagent to be employed as a proton source is H_2O due to its global abundancy.

When studying the H_2O-aided CO_2 reduction reaction, one must take into account the physical state of the water molecules, playing both the role of solvent whilst providing protons for the reduction reaction. CO_2 reduction in liquid H_2O mainly results in CH_3OH,[94] $HCHO$[95] and $HCOOH$[96] formation; whereas reduction in a gaseous H_2O environment mainly produces CH_4 molecules.[97] The conversion of CO_2 into CH_4 and or CH_3OH is highly interesting as these can be used directly as a chemical feedstock in many industrial applications, or consumed for energy production. Both reaction products require a different measurement system considering CH_3OH is a liquid and the photoreactor must thus be coupled to a liquid chromatography inlet, whilst the gaseous CH_4 products can only be measured by a gas chromatograph.

In general, chromatography offers a suitable monitoring system to measure the different reaction products formed from the aqueous CO_2 reduction reaction. The concentration of the various reaction products formed can be defined by a flame ionization detector, and possible O_2 concentrations could be measured by a thermal conductivity detector. [98]

Chapter 3

Experimental section

3.1 SrTiO$_3$ nanocrystal synthesis

SrTiO$_3$ nanocrystals (NCs) were synthesized utilizing trioctylphosphine oxide (TOPO) as a solvent and structure directing agent, and Cr^{3+} ions were embedded into the SrTiO$_3$ crystal structure by adding chromium(III) nitrate nonahydrate[11] or chromium(III) acetylacetonate (CrAcAc)[99] to the reaction mixture. The complex TOPO shell was first exchanged to a carboxylate shell utilizing oleic acid (OAc) under basic conditions. The OAc capped NCs were then stripped of using a mild BF$_3$:Et$_2$O/DMF stripping procedure developed by Doris et al.[13] The bare cationic NCs could then be utilized as building units into a NC framework through a polymer-templated assembly.[84]
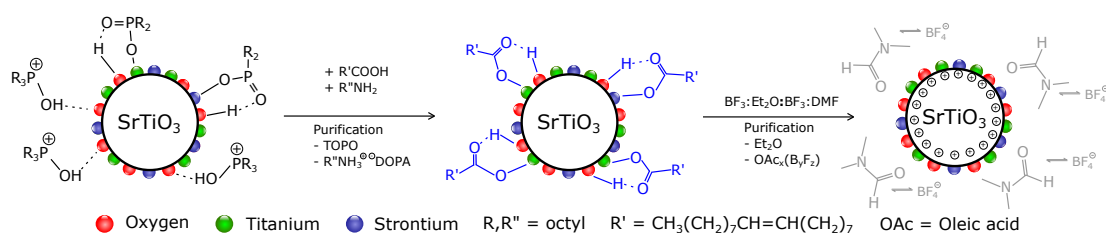
Figure 3.1.1: Overview of surface modifications performed on the nanocrystal: the d-n-octylphosphinate shell is first exchanged to a carboxylate shell through oleic acid treatment under basic conditions before being stripped off through a mild BF$_3$:Et$_2$O/DMF ligand stripping procedure.

3.1.1 Experimental procedure

TOPO was used as a solvent and a structure directing agent in the $SrTiO_3$ NC synthesis of, solubilizing the growing nanoparticles whilst limiting NC aggregation. TOPO is a hygroscopic substance which is detrimental for our NC synthesis. Thus, a recrystallisation in acetonitrile was performed to obtain pure crystalline TOPO.
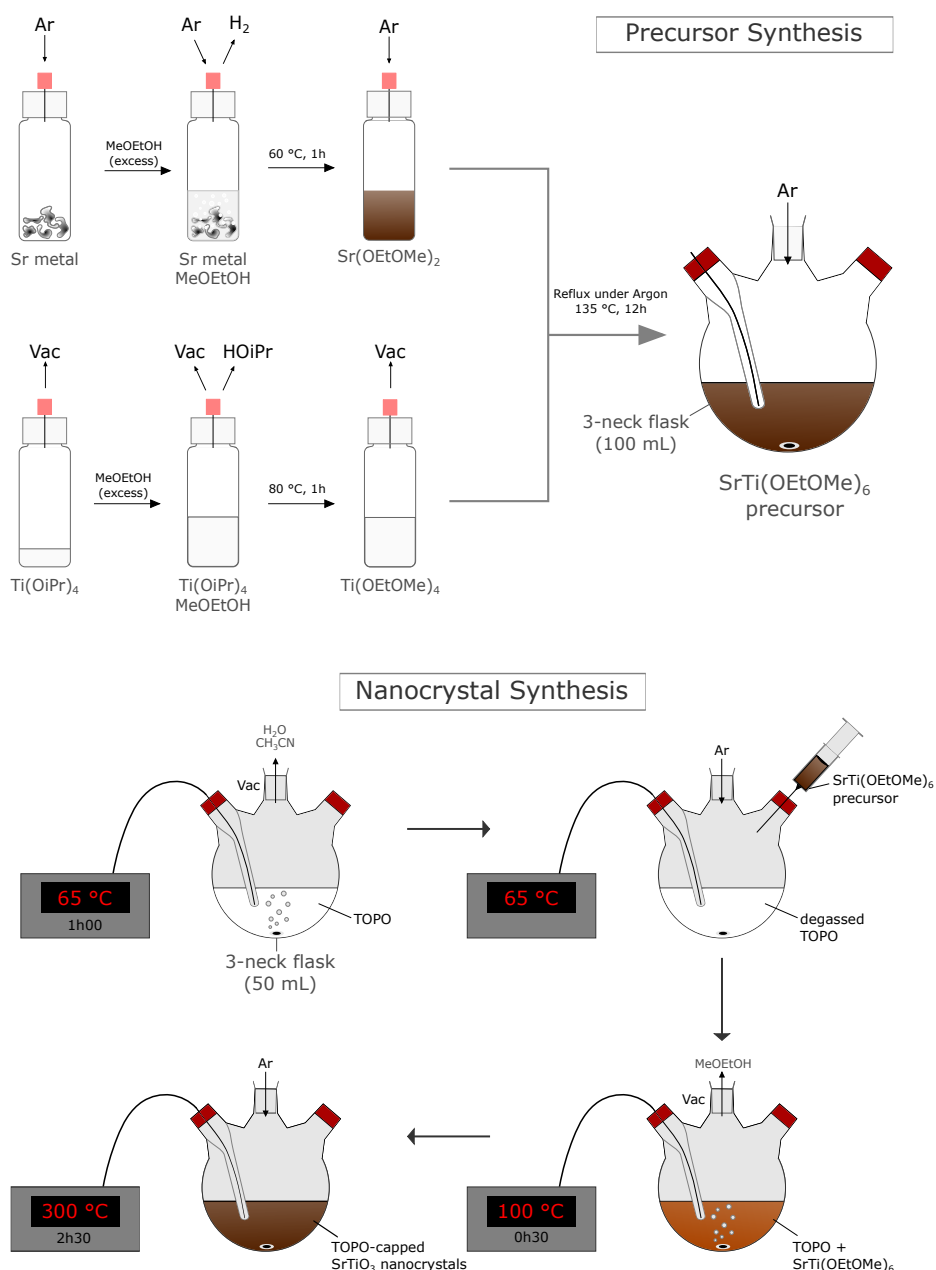
Figure 3.1.2: Overview synthesis of $SrTiO_3$ nanocrystals: (top) $SrTi(OEtOMe)_6$ precursor preparation in 2-methoxyethanol, (bottom) nanocrystal synthesis in TOPO.

First, 400 g of TOPO was dissolved in 3 L of CH_3CN at 60 °C. Next, the solution was filtered over a glass filter at 90 °C to remove all impurities. The filtered TOPO solution was left to crystallize for 3 days and the recrystallized TOPO was filtered over a glass filter under vacuum. Finally, the pure TOPO crystals were dried under vacuum for 48 hours to remove any residual CH_3CN. The purity of the recrystallised TOPO was confirmed through ^{31}P-NMR (figure 3.1.4).

To synthesize $SrTiO_3$ and Cr-doped $SrTiO_3$ NCs with a clean 1:1 Sr:Ti ratio, a $SrTi(OEtOMe)_6$ precursor was first synthesized. $Ti(OiPr)_4$ reacts with water to deposit TiO_2; and Sr, once ignited, reacts heavily with O_2 and N_2 to form solid SrO and Sr_2N_3 respectively. Both reagents must thus be kept under inert atmosphere at all times. To start, 0.525 g of Sr (6 mmol) and 1.776 mL $Ti(OiPr)_4$ (6 mmol) was weighed under inert atmosphere (Ar). Next, MeOEtOH was added in excess, 1.892 mL (24 mmol) in the $Ti(OiPr)_4$ vial and 5.677 mL (72 mmol) in the Sr vial respectively. The Sr vial was heated to 60 °C while stirring until Sr was completely dissolved and the solution displayed an orange-red, transparent colour which turned into a dark brown colour after several hours. Upon dissolving, bubbles of H_2 are formed that are displaced from the vial by the heavier argon gas. The $Ti(OiPr)_4$ MeOEtOH mixture was heated to 80°C while vigorously stirring and 1.892 mL (24 mmol) of additional MeOEtOH was added two consecutive times to force a complete ligand exchange. The vial was put under vacuum to remove isopropanol released from the ligand exchange reaction. Both solutions were added into a 100 mL three-neck flask under argon atmosphere and the mixture was refluxed overnight at 135 °C. The attained precursor solution was a viscous dark brown solution (figure 3.1.2).

The $SrTiO_3$ NCs were synthesized by adding 13.2 g of TOPO into a 50 mL three neck-flask containing a glass stirring bar, a glass finger, a septum, and a Graham coil condenser connected to a Schlenk line set-up with a small valve. The flask was placed within a heating mantle and the temperature sensor was inserted in the glass finger. First, the flask was heated to 65 °C to melt the solid TOPO and any residual adsorbed water or acetonitrile was vacuumed off. After degassing, the flask was flushed with argon and 3 mmol of $SrTi(OEtOMe)_6$ precursor was added with a syringe through the septum. The residual unbound MeOEtOH was vacuumed off as the mixture was slowly heated to 100 °C while vigorously stirring. When no more bubbles were formed the mixture was flushed with argon and heated to 300 °C. Once the temperature surpassed 250 °C, the TOPO gas could be seen as a white fume

above the reaction mixture as bubbles started ascending from the reaction mixture.

After 2 hours and 30 minutes at 300 °C, the flask was allowed to cool down to 80 °C. The reaction product was transferred into a plastic centrifugal tube, 20 mL of CH_3CN was added to dissolve the remaining TOPO and the NCs ($\pm$ 330 mg) were precipitated by centrifugation at 5000 rotations per minute (rpm) for 5 minutes. After centrifugation, the dark brown supernatant was discarded and the dark brown precipitate was left to dry for 1 minute under air. The nanoparticles (NPs) were dispersed in 10 mL of toluene and were stable without adding additional surfactants. To remove all unbound TOPO, the NCs were precipitated with 20 mL of CH_3CN and redispersed in 10 mL of toluene for three consecutive times.
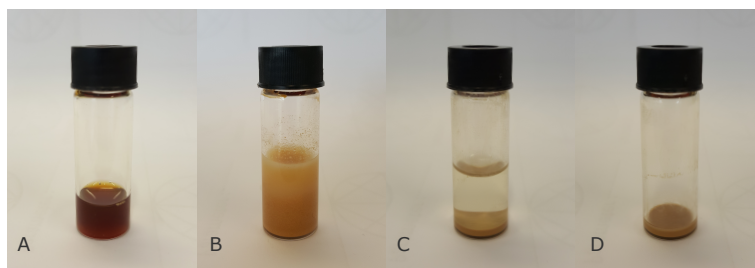
Figure 3.1.3: (A) nanocrystal toluene dispersion, (B) colloidal dispersion after adding acetonitrile, (C) precipitate and supernatant, (D) $SrTiO_3$ precipitate after centrifugation.

3.1.2 Characterization

To assign which types of TOPO derivatives are bound to the NC surface, a ^{31}P-NMR spectrum was taken (figure 3.1.4). The bottom spectrum displays the ^{31}P-NMR spectrum for pure, recrystallised TOPO. The sharp resonance peak at $\delta = 43$ ppm coincides with that of free neutral TOPO. No further peaks are visible in this spectrum which indicate that the recrystallised TOPO is indeed pure. The top ^{31}P-NMR spectrum was taken from the SrTiO$_3$ NCs suspension after three consecutive CH$_3$CN purification steps. The resonance peak at $\delta = 57$ ppm can be ascribed to di-n-octylphosphinate (DOPA) groups that are bound to the NC surface. The resonance peak broadening can be ascribed to the bound state of DOPA.
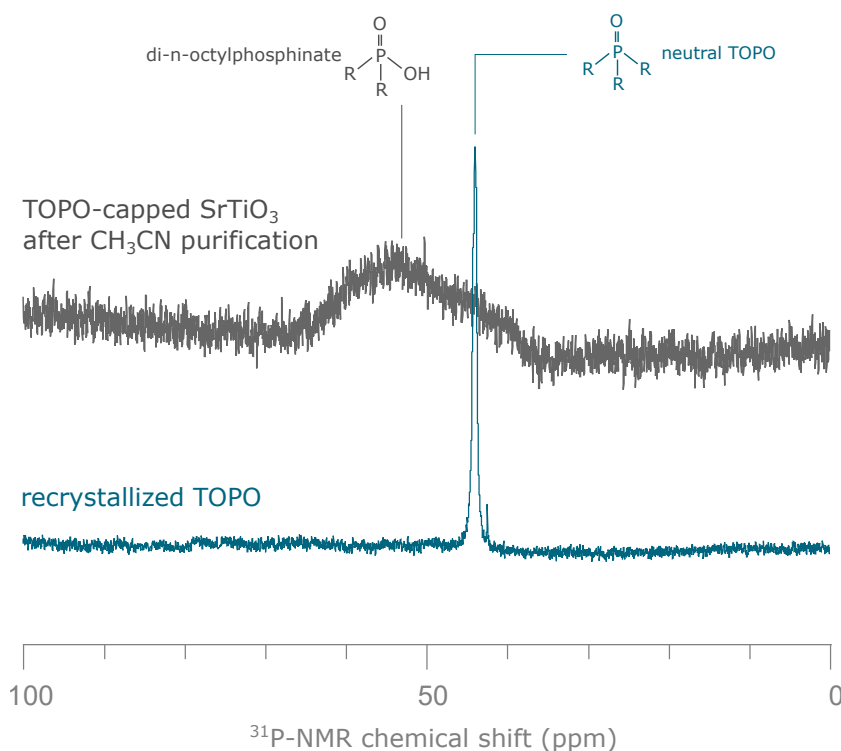
Figure 3.1.4: (top) ^{31}P-NMR spectrum of SrTiO$_3$ NCs after CH$_3$CN purification, (bottom) ^{31}P-NMR spectrum of pure TOPO after recrystallisation.

Image 3.1.5 shows the dynamic light scattering (DLS) spectrum of TOPO-capped SrTiO$_3$ NCs. The as-synthesized SrTiO$_3$ NCs surface is coated with protonated TOPO, through H-bonding with the surface O-species, di-n-octylphosphinate, through covalent bonding with the surface Sr and Ti atoms, and surrounded by free unbound TOPO.[12] Before CH$_3$CN purification, large agglomerates are present in the NC suspension owing to the free unbound TOPO molecules present in the suspension. After

three consecutive CH_3CN purification steps, the agglomerates have disappeared and a sharp peak around 10 nm has emerged with the major peak indicating a hydrodynamic diameter of 7.396 nm and a polydispersity index of 0.255. The CH_3CN purification steps have washed of all unbound TOPO and gave result to a monodisperse NC suspension. TEM images further confirm the monodispersity and non-agglomeration of the NCs (figure 3.1.5.B).
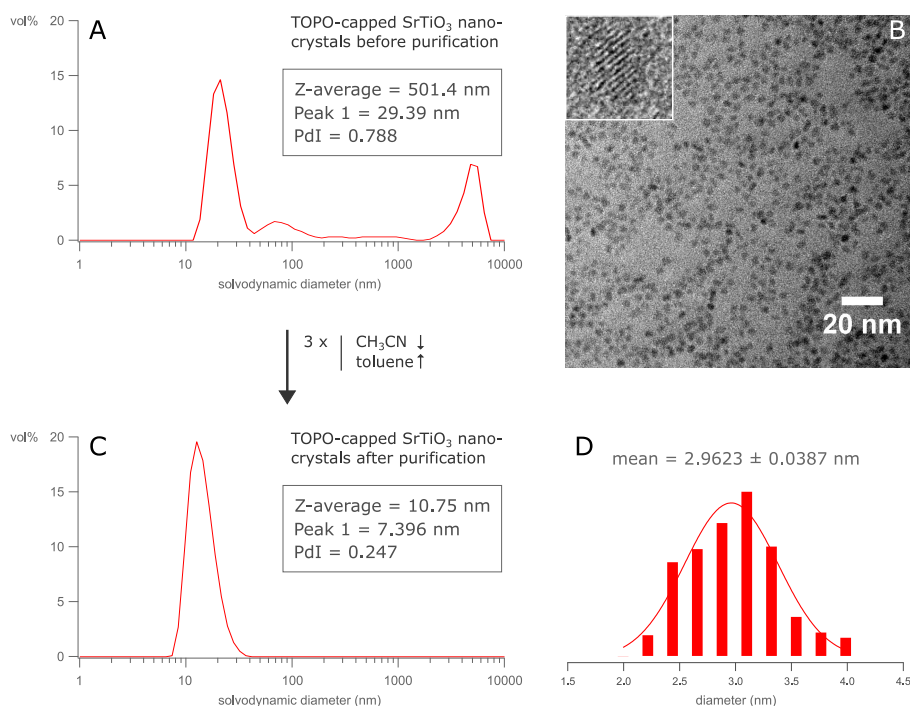
Figure 3.1.5: (A) DLS image of as-synthesized TOPO capped $SrTiO_3$ nanoparticles before CH_3CN purification and (C) after CH_3CN purification (B) TEM image of TOPO capped $SrTiO_3$ nanoparticles after CH_3CN purification and (D) histogram of the undoped $SrTiO_3$ nanoparticles size.

An X-Ray diffraction (XRD) measurement was performed on the $SrTiO_3$ NCs to identify the crystallite size and phase (figure 3.1.6). The measurement was performed using $Cu_{K\alpha}$ radiation in a 2θ range from 25 to 65°. Characteristic peaks can be found at 32.2°, 40°, 46.3° and 57.5° that can be assigned to the (110), (111), (200) and (211) diffractions respectively. The characteristic peaks are in perfect alignment with the diffraction peaks for the $Pm\bar{3}m$ space group which corresponds with a cubic crystal structure with lattice cell parameters a = 0.39053 nm.[100] The peak broadening is consistent over all diffraction peaks and is owed to the nanosize of the crystallite. The Scherrer equation (formula 3.1.1) was used to determine the crystallite size; where k is a constant (0.94 for this equation), λ is the X-ray wavelength

$(\lambda_{K\alpha} = 0.15418$ nm), θ is the diffraction angle of the characteristic peak with the highest intensity, $32.2°$ for SrTiO$_3$ which is devoted to the (110) diffraction, and β is the full width at half maximum of the major peak, equal to $4.3°$ in this spectrum. Based on this formula, we were able to calculate the crystal size to be about 2.01 nm.

$$D = \frac{k\lambda}{\beta cos(\theta)} \qquad (3.1.1)$$
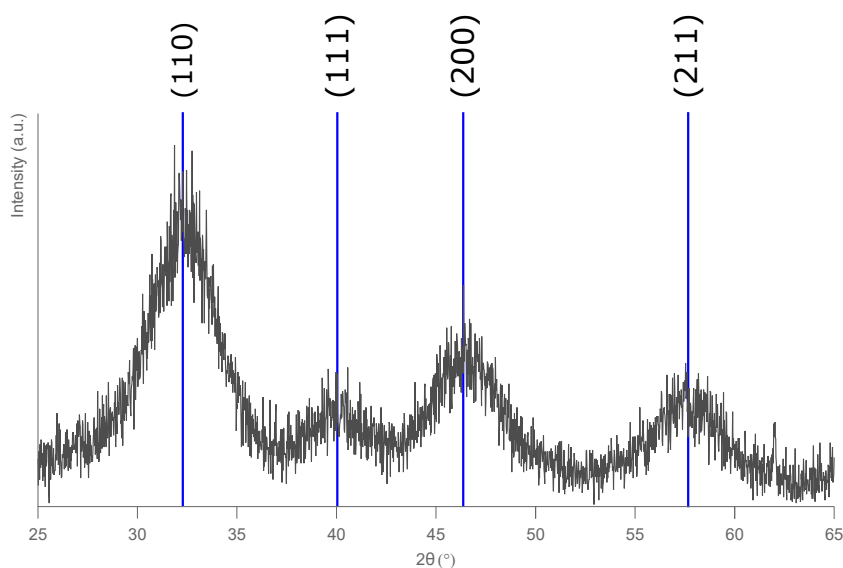
Figure 3.1.6: XRD spectrum of SrTiO$_3$ nanocrystals after purification with CH$_3$CN.

3.2 Cr-doped SrTiO$_3$ nanocrystal synthesis

3.2.1 Chromium(III) Nitrate Nonahydrate route

3.2.1.1 Experimental procedure

To synthesize Cr-doped SrTiO$_3$ NCs, 0.15 mmol of chromium(III) nitrate nonahydrate (Cr(NO$_3$)$_3$.9 H$_2$O) was dissolved in 2 mL butanol.[11] Next, TOPO was degassed at 65 °C under vacuum to remove any residual adsorbed water. After 1 hour of degassing under vacuum, the flask was flushed with argon, 3 mmol of the SrTi(OEtOMe)$_6$ precursor and 0.15 mmol of the olated Cr(NO$_3$)$_3$ precursor was added to the flask. The flask was then put under vacuum again at 65 °C to remove any residual MeOEtOH and butanol. When bubble formation stopped, the flask was flushed again with argon and the temperature was set at 300 °C. However, the reaction mixture only reached a temperature of 250 °C. Bubble formation could be seen and the same white fog was visible inside the flask as could be seen for the undoped SrTiO$_3$ NC synthesis. After 2 hours and 30 minutes the temperature still did not exceed 250 °C. The reaction was stopped and the reaction product was precipitated with CH$_3$CN and purified as was done for the undoped SrTiO$_3$ NC synthesis. Quite remarkable was the fact that the reaction product started solidifying at 180 °C as opposed to the undoped SrTiO$_3$ NCs in which the reaction mixture only started solidifying below 60 °C. After three consecutive purification steps the precipitate had a greyish/green colour. When adding 10 mL of toluene to the solid product, a turbid dark green suspension was attained with a black and green precipitate.

3.2.1.2 Characterization

The suspension was precipitated with CH$_3$CN and centrifuged for 2 minutes at 5000 rpm. This resulted in a green supernatant and a green precipitate with black spots. The precipitate was then dried for 2 days under air and grounded into a fine powder for XRD analysis. The obtained XRD spectrum did not exhibit diffraction peaks at 32.2°, 40°, 46.3° and 57.5° as would be expected for a cubic SrTiO$_3$ NC. Furthermore, the XRD pattern did not exhibit any diffraction peaks at all, indicating that no crystalline material was formed (figure 3.2.1). Doping should only induce small changes in the crystal lattice structure and thus Cr-doped SrTiO$_3$ should exhibit the same characteristic peaks as pristine SrTiO$_3$. Based on this XRD pattern, and the observations that the material did not exhibit the same colour, solidified at a differ-
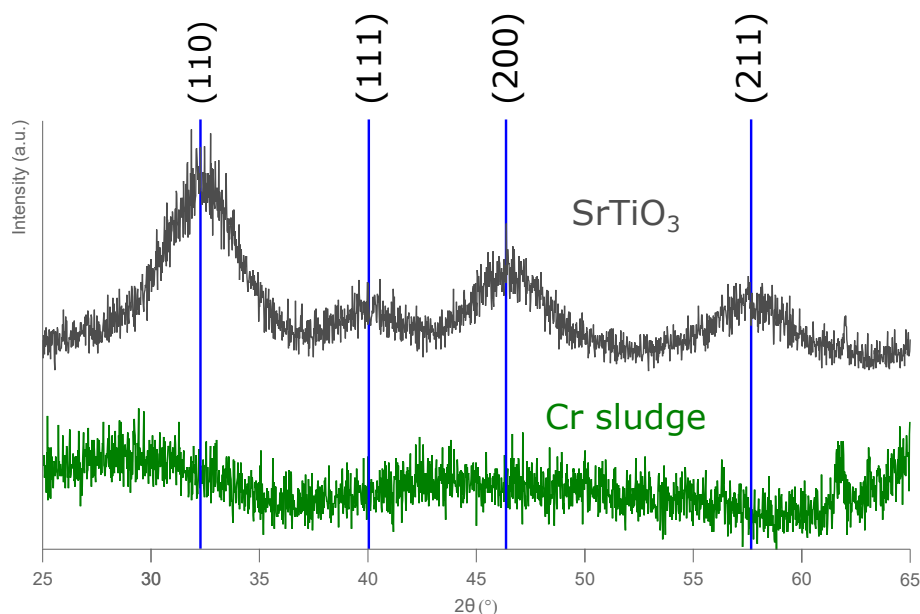
Figure 3.2.1: (top) XRD spectrum of the cubic crystal structure of undoped $SrTiO_3$ nanocrystals, (bottom) XRD spectrum of the synthesized Cr sludge, displaying no resemblance with the (110),(110),(200) or (211) XRD signals for cubic $SrTiO_3$ nanocrystals.

ent temperature, and did not dissolve in toluene as compared to pristine $SrTiO_3$; it was clear that no Cr-doped $SrTiO_3$ NCs were formed.

To check whether the $Cr(NO_3)_3$ precursor solution was the reason for this sludge formation, another reaction was performed using only 13.2 g of TOPO and 0.15 mmol of $Cr(NO_3)_3$ precursor. The reaction set-up and execution was the same as previously used for the undoped $SrTiO_3$. The mixture inside the flask displayed a bright green colour which turned into a dark brown/greyish colour after heating the mixture above 150 °C. The mixture reached a temperature of 300 °C and remained there for 2 hours and 30 minutes. After reaction completion, the product mixture cooled down below 180 °C without solidifying. There was no black precipitation present in the flask and when adding CH_3CN no precipitation formation could be seen. Thus indicating that the $Cr(NO_3)_3$ TOPO interaction was not the reason for this sludge formation. However, because synthesis with the $Cr(NO_3)_3$ precursor did not result in the desired Cr-doped $SrTiO_3$ NCs, this reaction procedure was not pursued any further. Possible reasons as to why this reaction procedure did not result in the formation of Cr-doped $SrTiO_3$ NCs were not further investigated.

3.2.2 Chromium(III) Acetylacetonate route

3.2.2.1 Experimental procedure

As a second attempt, chromium(III) acetylacetonate (CrAcAc) was used as a precursor for synthesizing Cr-doped $SrTiO_3$ NCs.[99] First, 0.15 mmol of CrAcAc was added to 0.5 mL of MeOEtOH and the solvent was heated to 60 °C until all CrAcAc had dissolved. The CrAcAc precursor was added to the three-neck flask under argon, containing degassed TOPO at 60 °C along with 3 mmol of the $SrTi(OEtOMe)_6$ precursor. The flask was degassed under vacuum to remove any residual MeOEtOH until no more bubbles were formed. Next the temperature was raised to 300 °C and the reaction mixture was kept there for 2 hours and 30 minutes. After reaction completion, the reaction product exhibited a dark brown colour and did not solidify at 180 °C as could be seen for the $Cr(NO_3)_3$ precursor. The contents of the flask were transferred to a plastic tube and 20 mL of CH_3CN was added to dissolve the remaining TOPO and precipitate the as-synthesized NCs. After centrifugation for 5 minutes at 5000 rpm, the supernatant was discarded and the dark brown precipitate was dissolved in 10 mL of toluene. Three consecutive washing steps were performed with CH_3CN and toluene. The precipitate displayed the same beige colour as could be seen for the undoped $SrTiO_3$ NCs (figure 3.1.3.D).

3.2.2.2 Characterization

The precipitate was dried in plain air for 2 days and grounded into a fine powder for XRD analysis. The acquired XRD spectrum displayed the same characteristic diffraction peaks as could be seen for the undoped $SrTiO_3$. Consequently, the Cr-doped $SrTiO_3$ NCs exhibit the same cubic crystal structure and space group $Pm\bar{3}m$. Incorporating a dopant element in the crystal structure induces a shift in the 2θ value of the peaks in the XRD spectrum. Substituting the twelve-fold coordinated Sr^{2+} ions, with an ionic radius of 0.144 nm, by Cr^{3+} ions, with an ionic radius of 0.0615 nm, should result in a decreased crystal plane interspacing d, and thus an increase in the 2θ value according to Bragg's law (formula 3.2.1). The Ti^{4+} ions, which are six-fold coordinated to the O^{2-} ions, exhibit an ionic radius of 0.0605 nm, which is smaller than the ionic radius of Cr^{3+} ions. Concomitantly, the substitution site of Cr^{3+} ions in the perovksite oxide can be measured with XRD analysis.
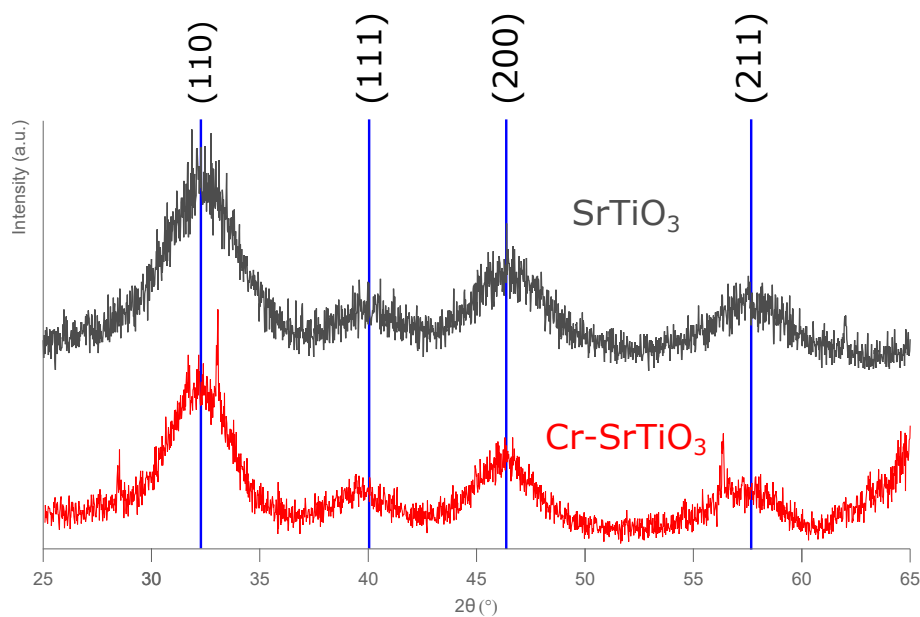
Figure 3.2.2: (top) XRD spectrum of the cubic crystal structure of undoped SrTiO$_3$, (bottom) XRD spectrum of the cubic crystal structure of Cr-doped SrTiO$_3$.

$$2dsin(\theta) = n\lambda \tag{3.2.1}$$

The XRD pattern in figure 3.2.2 exhibits a line broadening effect due to the nanometer size of the material, which makes determination of the center of the major diffraction peak (at around 32.2°) rather subjective. As a result, the 2θ shift due to Cr-incorporation could not be determined. The XRD pattern shows that the Cr-doped SrTiO$_3$ NCs are indeed crystalline and exhibit a size of about 2.01 nm, as calculated through the Scherrer equation (formula 3.1.1). To confirm the monodispersity, a DLS measurement was taken after CH$_3$CN purification, the resulting DLS spectrum can be seen in figure 3.2.3. The NPs are covered with TOPO ligands that are solvated in a toluene solvation shell. The size peak obtained by DLS thus includes the NPs diameter, ligand shell and solvation shell. The major peak identified in this spectrum is centered at 7.141 nm, which corresponds rather well to our calculated NC size if we take into account the ligand shell and solvation shell of our TOPO-capped NC. The near perfect alignment of the volume % peaks indicate that the TOPO-capped Cr-SrTiO$_3$ dispersion is indeed monodisperse and non-agglomerated. These findings are confirmed with the TEM image on the right side of figure 3.2.3, displaying the NC dispersion in toluene and a detail of one of the NCs crystal planes. Furthermore, the TEM image allows us to gain a visual representation of the size of our NCs.
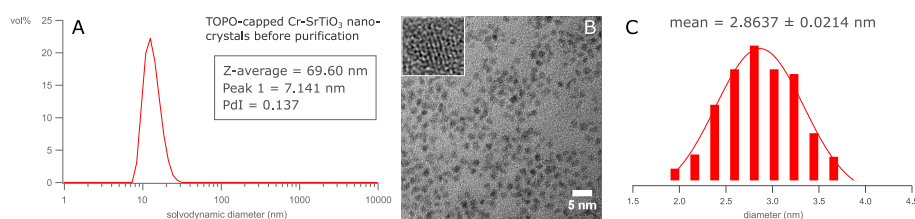
Figure 3.2.3: (A) DLS spectrum of Cr-doped SrTiO$_3$ after purification with CH$_3$CN, (B) TEM image of Cr-doped SrTiO$_3$ after purification with CH$_3$CN, (C) histogram of the Cr-doped SrTiO$_3$ nanocrystals size.

3.3 SrTiO$_3$ nanocrystals ligand exchange

3.3.1 Experimental procedure
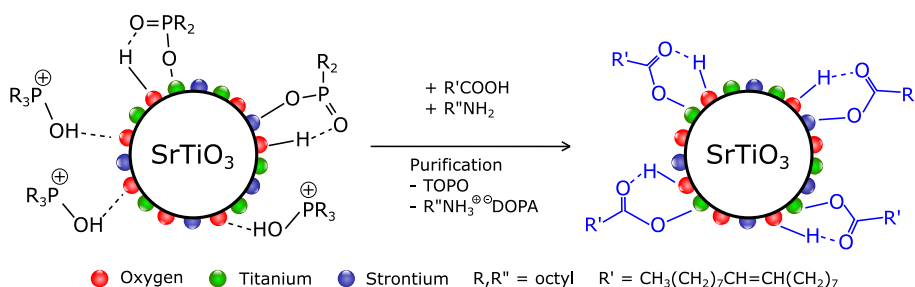
Figure 3.3.1: Exchanging TOPO capped nanocrystals through the oleic acid/n-octylamine ligand exchange procedure.

The ^{31}P-NMR spectrum (figure 3.1.4) taken right after purification indicated DOPA to be the sole ligand attached to the NC surface, with the hydroxyl-tri-n-octylphosphonium associated with the NC surface through H-bonding. Since the complexity and steric volume of the apolar n-octyl chains can obscure structure-function relationships, a simplification of the complex ligand shell was needed.[101] The experimental procedure used was the same as stated in the paper of De Roo et al.[12] To perform the ligand exchange, 200 µL of octAm and 400µL of OAc was added in excess to 1 mL of the NC toluene suspension. The basic octAm liberates neutral TOPO molecules from the surface and partially desorbs the DOPA molecules bound to the surface. Addition of OAc together with octAm removes TOPO more completely and OAc displaces the DOPA ligands for a complete carboxylate shell. The suspension is precipitated with 2 mL of acetone and centrifuged for 2 minutes at 5000 rpm. The solid precipitate was suspended in 1 mL of hexane and 50µL of OAc was added a second

time to force the remaining DOPA ligands off of the NCs surface. The suspension was then washed for 3 consecutive times with acetone and suspended in 1 mL of hexane to result in a stable dispersion with a transparent brown colour.
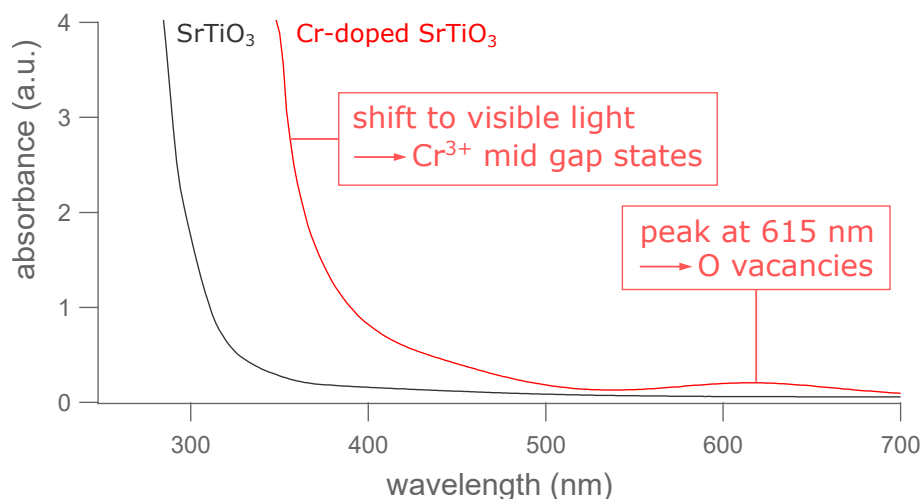
Figure 3.3.2: UV-Vis measurement of undoped $SrTiO_3$ and Cr-doped $SrTiO_3$ nanocystals capped with oleic acid ligands, displaying a shoulder formation at 500 nm induced by the Cr^{3+} ions, and a peak at 615 nm owing to the oxygen vacancies in Cr-doped $SrTiO_3$.

To test whether the optical activity of the synthesized Cr-doped $SrTiO_3$ NCs was indeed extended to the visible light region, a UV-Vis measurement was performed on the OAc capped Cr-doped and undoped $SrTiO_3$ NCs. The UV-Vis samples were prepared by suspending 5 mg of NCs in 5 mL of hexane. The resulting UV-Vis spectrum can be witnessed in figure 3.3.2. As can be observed from the spectrum, the UV-Vis response of Cr-doped $SrTiO_3$ NCs is significantly extended to the visible light region as opposed to the undoped $SrTiO_3$ NCs. By doping the photocatalyst with Cr^{3+} ions we thus increase the optical properties of the photocatalyst, as was intended.
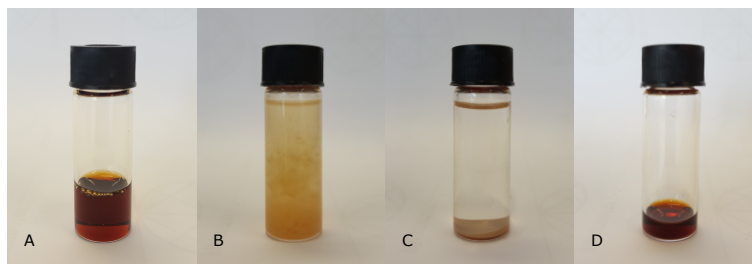
Figure 3.3.3: (A) TOPO capped nanocrystals suspended in toluene along with oleic acid and n-octylamine, (B) precipitation after adding acetone, (C) precipitate and supernatant after centrifugation, and (D) oleic acid capped nanocrystals suspended in 0.5 mL of hexane.

3.3.2 Characterization

To monitor the progress of the ligand exchange reaction during the course of re-action, X-ray Fluorescence (XRF) spectrometry was applied on the NC suspension to verify if any phosphorous ligands were still present. When the phosphor con-taining DOPA ligands were completely exchanged for the OAc ligands, the signal for P should disappear accordingly from the XRF spectrum. To prepare the XRF sample, 50 µL of the NC suspension was deposited on a white teflon disk and the hexane solvent was left to evaporate from the disk for 15 minutes. The disk was then placed into the XRF instrument and three successive measurements were taken with a focus on Sr, Ti, C, Cr and P. The XRF signal for P reduced from 2.03 to 0 mass%, indicating a complete removal of the native DOPA ligands and TOPO molecules after the OAc/n-octAm treatment.
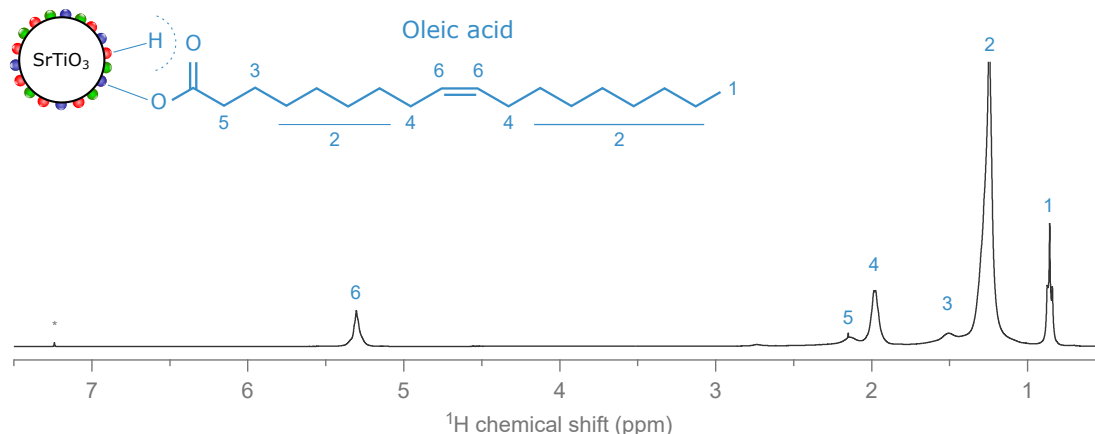
Figure 3.3.4: ^{1}H-NMR spectrum of oleic acid capped nanocrystals after a complete oleic acid/n-octylamine ligand exchange procedure and three acetone purification steps (* = CDCl$_3$).

To verify whether a complete carboxylate shell was attained during the ligand ex-change procedure, a ^{1}H-NMR spectrum was taken. The sample was prepared by precipitating 1 mL of the hexane NC suspension with acetone, drying it through a vacuum atmosphere, and redispersing it in deuterated chlorofom. The resulting NMR spectrum can be found in figure 3.3.4. The sharp resonance at $\delta = 0.8$ ppm can be linked to the methyl end group of OAc, whilst the major peak in the spectrum, at $\delta = 1.3$ ppm, is owed to the CH$_2$ groups. A resonance peak can also be found in the region $\delta = 5.4$ ppm owing to the H atoms bonded on the OAc alkene group. Peak 4 at $\delta = 2$ ppm can be assigned to the CH$_2$ groups neighbouring the alkene. All peaks in the ^{1}H-NMR spectrum can thus be assigned to that of surface bound oleyl chains, which, together with the lack of signals in the XRF results, leads to the

conclusion that the native TOPO ligands are successfully exchanged for OAc ligands.

The NC suspension exhibited a transparent brown colour, indicating the OAc capped NC's were stable in hexane. A DLS measurement confirmed this observation, and no agglomerated species could be identified (figure 3.3.5.A). A TEM image was also taken to verify the monodispersity retainment, which is preserved after the ligand exchange as can be seen on figure 3.3.5.B.
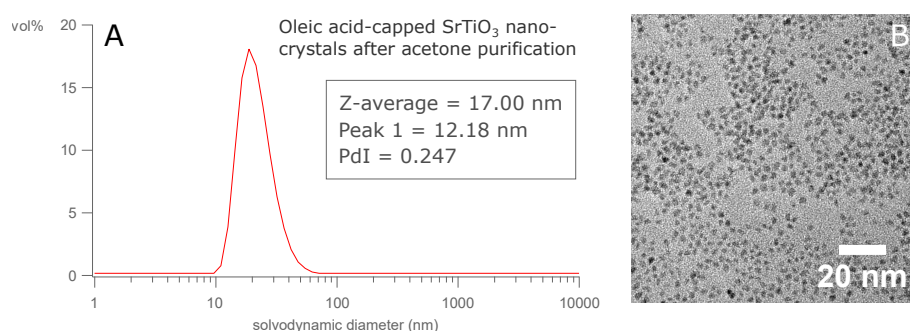
Figure 3.3.5: (A) DLS spectrum of oleic acid capped nanocrystals, (B) TEM image of oleic acid capped nanocrystals.

3.4   SrTiO$_3$ nanocrystal ligand stripping
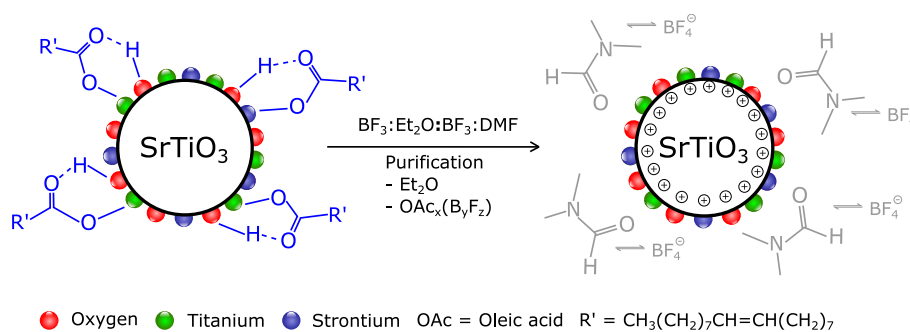
Figure 3.4.1: Stripping of oleic acid capped nanocrystals by a Et$_2$O:BF$_3$ treatment to result in cationic nanocrystals under equilibrium control with DMF and BF$_4^-$.

Before the SrTiO$_3$ and Cr-doped SrTiO$_3$ NCs can be utilized as building units into a polymer-templated mesoporous NC framework, the OAc ligands have to be stripped from the surface to expose the cationic NC surface. The naked cationic NC surfaces have to remain bare to allow a favourable interaction with the NC-tethering domains of the block copolymers (BCPs) (see section 2.6). For these reasons we explored the mild ligand stripping procedure developed by Doris et al.[13] Activated DMF was

prepared by adding 20 µL of boron trifluoride diethyl etherate (BF$_3$:Et$_2$O) to 500 µL of DMF. To start, 1 mL of the hexane NC suspension containing 5-10 mg/mL of NCs was precipitated with acetone and the dry NCs were redispersed in 500 µL of anhydrous hexane (figure 3.4.2.A). Next, 500 µL of the activated DMF solution was added to the hexane NC suspension resulting in a two-phased liquid system with hexane as the top layer ($\rho = 0.867$ g/L) and DMF as the bottom layer ($\rho = 0.944$ g/L) (figure 3.4.2.B).
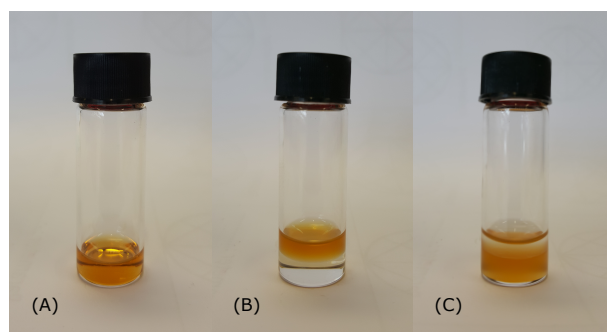
Figure 3.4.2: Ligand stripping procedure: (A) oleic acid capped nanocrystal suspended in hexane, (B) two-phased liquid system, with DMF/BF$_3$:Et$_2$O as the bottom layer and the nanocrystal hexane suspension as the top layer (C) two-phased liquid system after 10 minutes, with the nanocrystals now suspended in DMF.
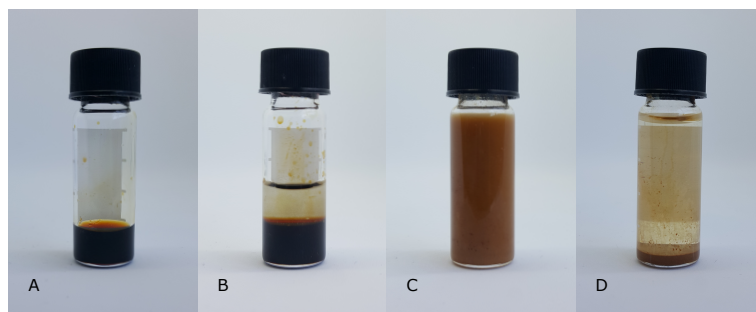
Figure 3.4.3: Washing procedure: (A) BF$_4$$^-$ electrostatically stabilized nanocrystals in DMF (B) hexane washing step, with hexane as the top layer and the nanocrystal DMF suspension as the bottom layer, (C) mixing of the two layers induced by toluene, and (D) precipitated nanocrystals and supernatant after centrifugation.

The two-phased system was mixed vigorously for 2 minutes to induce the ligand stripping procedure. After about 2 minutes in the ultrasonic bath, the OAc ligands were all stripped from the NCs surface which invoked a change in solvent solubility from hexane to DMF. To induce mixing of the two layers, 3 mL of toluene was added which resulted in a turbid brown colloidal suspension (figure 3.4.3). The suspension was centrifuged for 2 minutes at 5000 rpm, dispersed in 1 mL of DMF, and washed

for 2 consecutive times with 1 mL of hexane and precipitated with 2 mL of toluene. Finally, the NC precipitate was suspended in 1 mL of DMF which resulted in a transparent brown, electrostatically stabilized NC suspension. The precipitated cationic NCs displayed an exceptional solubility and stability in DMF which is owed to its costabilizing role in the stripping procedure.[13] The monodispersity retainment and non-agglomeration of the cationic NCs were verified through DLS and TEM (figure 3.4.4).
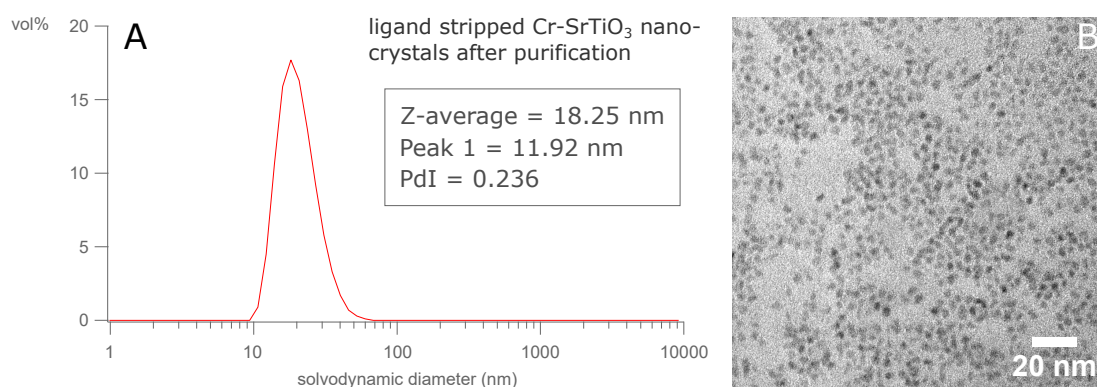
Figure 3.4.4: (A) DLS spectrum of ligand stripped Cr-doped $SrTiO_3$ nanocrystals, (B) TEM image of ligand stripped Cr-doped $SrTiO_3$ nanocrystals.

Figure 3.4.5 depicts the Fourier-transform infrared (FTIR) spectroscopy spectrum of the ligand stripped $SrTiO_3$ NCs versus the FTIR spectrum of OAc capped $SrTiO_3$ NCs. From the OAc capped FTIR spectrum, a sharp peak at 3011 cm^{-1} can be observed attributed to alkene C-H bond stretching. The two peaks at 2929 cm^{-1} and 2856 cm^{-1} can be assigned to the symmetric and asymmetric stretching vibrations of CH_2 and CH_3. A weak to medium C=C stretch is observed at around 1600 cm^{-1} owing to cis and trans alkene bonds in OAc. A peak is observed at around 1400 cm^{-1} which coincides with that of carboxylic acid C=O stretching vibrations. There is no broad O-H stretch region present between 3300-2500 cm^{-1}, indicating that all OAc is bound with the carboxylate group to the surface and no unbound OAc is present in the precipitate. Free unbound OAc displays a strong characteristic peak at 1700 cm^{-1} related to C=O stretch vibrations of carboxylic acid and C=C stretch vibrations of cis and trans OAc, which is not present in this spectrum.[102]

In the ligand stripped NC FTIR spectrum the sharp C-H stretches at around 3000 cm^{-1}, owing to CH_2 and CH_3 stretch vibrations, have strongly diminished indicating the removal of OAc ligands from the NC surface. The peaks in the region 3000-2800
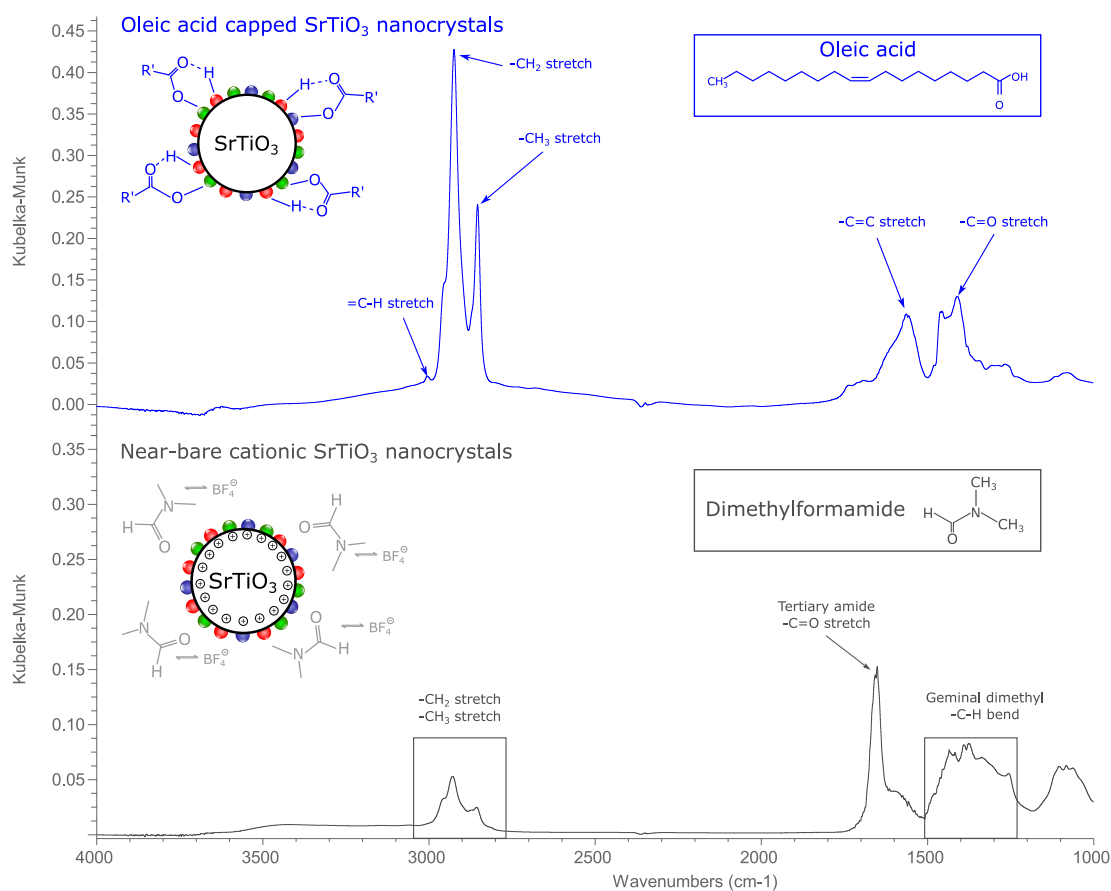
Figure 3.4.5: (top) oleic acid capped SrTiO$_3$ nanocrystals and (bottom) ligand stripped SrTiO$_3$ nanocrystals electrostatically stabilized by BF$_4^-$ and co-stabilized by DMF.

cm^{-1} can be attributed to C-H stretch vibrations from the two CH$_3$ groups of DMF, and CH$_2$ and CH$_3$ stretches from remaining OAc ligands bound to the NC surface. At around 1700 cm^{-1} a sharp peak is observed owing to C=O stretch vibrations from the tertiary amide group in DMF. A broad area between 1500-1250 cm^{-1} is also observed owing to the geminal dimethyl groups of DMF. Based on this FTIR spectrum we can conclude that the ligand stripping procedure removed the majority of OAc ligands, yet some ligands retained to the NC surface. During the stripping procedure the Lewis acid BF$_3$ forms a physisorbed [OAc:BF$_3$]$^-$ with the carboxylate terminus of the bound oleyl oleate ligands that is in a dynamic equilibrium with DMF and is responsible for the surface stabilization during the stripping procedure. Because an excess of BF$_3$ is added, the physisorbed [OAc:BF$_3$]$^-$ undergoes a disproportionate reaction to form a neutral OAc$_x$(B$_y$F$_z$) species which is lost during the hexane washing step, and BF$_4^-$ serves as an electrostatic stabilizer for the near-bare cationic surface. DMF and BF$_4^-$ are in dynamic equilibrium with the cationic surface which explains the occurrence of DMF in the stripped NCs FTIR spectrum.
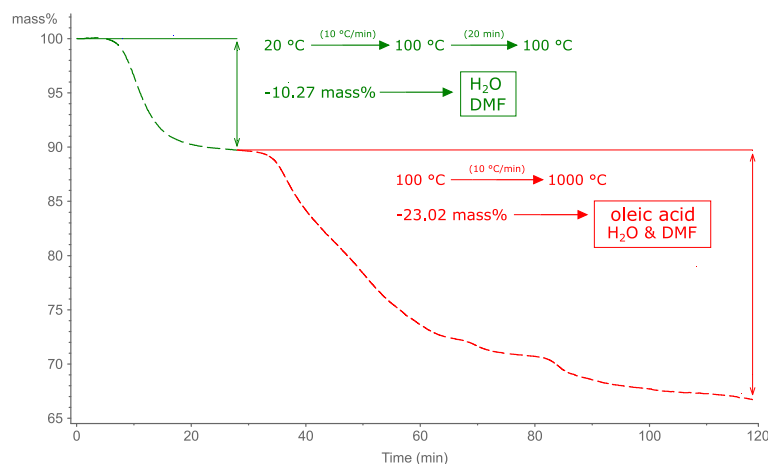
Figure 3.4.6: TGA curve of near-bare, cationic $SrTiO_3$ nanocrystals: the majority of DMF and physisorbed H_2O is thermally degraded in the first heating and isothermal step to 100 °C; residual oleic acid, DMF, and chemisorbed H_2O is thermally degraded in the second heating step to 1000 °C.

Figure 3.4.6 shows the TGA curve of the precipitated cationic $SrTiO_3$ NCs that have been dried in plain air for 2 days. The empty crucible was tarred and 100 μL of the cationic NC suspension was added and left to dry in an oven at 80 °C. After the dry NCs were obtained, the filled crucible was loaded in the TGA instrument and the measurement started. The sample was first heated from 20 °C to 100°C at a heating rate of 10 °C/min, at which it stayed for 20 minutes. The TGA curve displays a mass change of about 10.27 mass% after this isothermal step, which is owed to adsorbed water molecules and residual DMF evaporating from the surface. The sample was further heated to 1000 °C to thermally degrade all organic ligands and only retain the inorganic $SrTiO_3$ NCs. A mass change of 23.02 % can be seen when in the 100 °C to 1000 °C curve, this mass change is owed to remaining OAc ligands that are not completely stripped from the NC surface upon BF_3:Et_2O treatment. The BF_3:Et_2O stripping procedure thus strips of about 77% of the OAc ligands but retains about 23%. A more complete stripping of the OAc ligands might be obtained when using a stronger stripping procedure, as is discussed further in the future recommendations section. Furthermore, the crucible mass displayed a mass of 5.565 mg after the full temperature sequence. Based on this data the final yield of the bare cationic NCs was calculated at 20.22%.

3.5 Mesoporous SrTiO$_3$ and Cr-doped SrTiO$_3$
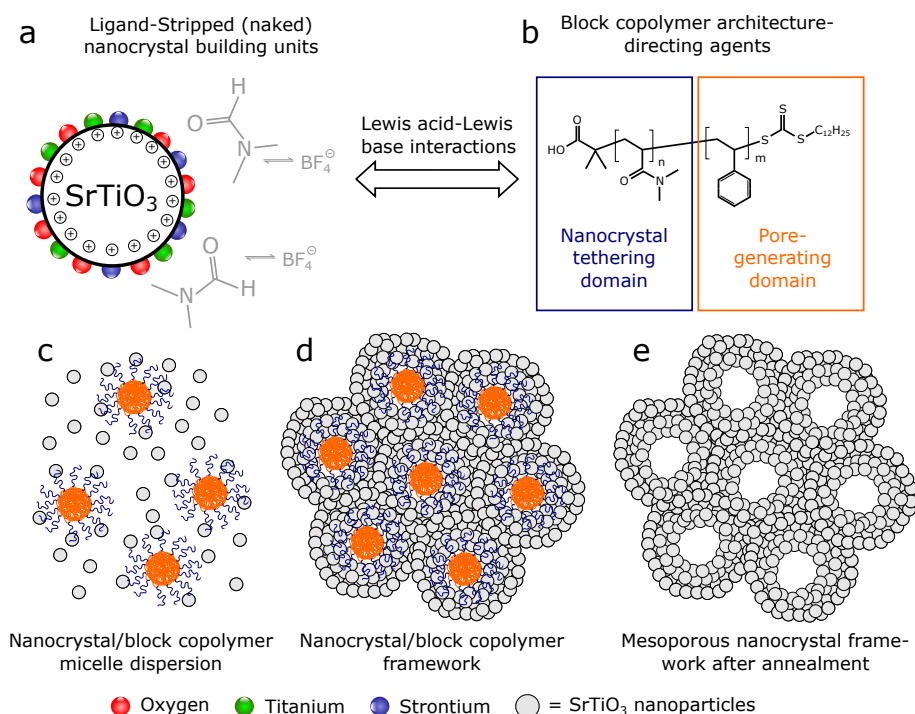
Figure 3.5.1: (a) naked cationic SrTiO$_3$ nanoparticles, (b) PDMA-b-PS block-copolymer, (c) nanocrystal/block-copolymer dispersion, (d) nanocrystal/block-copolymer framework, and (d) mesoporous nanocrystal framework after annealing.

3.5.1 Mesoporous layers

To gain a visual representation of the mesoporous NC framework we aimed to deposit mesoporous layers on a silicon wafer and analyse it through scanning electron microscopy (SEM). The NC framework was formed with the aid of a PDMA-b-PS BCP, where PDMA serves as the NC-tethering domain, owing to the structural similarity to DMF, and PS as the pore-generating domain due to its apolar character. Several BCPs with differences in M$_w$ of the NC-tethering domain and pore-generating domain were tested (table 3.5.1). To start, 12.5 mg of the desired BCP was weighed into a 4 mL glass vial. The BCP was dissolved in 100 µL of dimethylformamide (DMF) and left to stir at 20 °C for 2 hours, the solution was a clear transparent liquid with a slight yellowish reflection. Next, 400 µL of ethanol was added to the BCP solution in drops of 10 µL to create a micellar solution, the suspension was then stirred vigorously for 1 day. When adding EtOH, a colour change from transparent yellowish to turbid white with a slight blue reflection is observed.

Polymer	PDMA (g/mol)	PS (g/mol)	PDI	BCP:NC mass ratio
P1	8300	24700	1.30	1:2, 1:3, 1:4
P2	5100	4700	1.15	1:2
P3	5100	8900	1.26	1:2
P4	5100	7400	1.16	1:2
P5	5100	7900	1.14	1:2

Table 3.5.1: List of block copolymers used as structure directing agents in the nanocrystal framework polymer-templating method.

Because the BCP:NC mass ratio is a determining factor in the mesopore size and periodicity of the framework; a 1:2, 1:3 and 1:4 BCP:NC mass ratio was tested with BCP P1. First, 5 mg, 7.5 mg and 10 mg of the the cationic NCs were precipitated through hexane/toluene and were redispersed in 20 µL, 25 µL and 30 µL of DMF respectively after drying in plain air. Next, 100 µL of micellar BCP solution was added to each NC suspension under vigorous stirring to obtain a monodisperse distribution of NC-coated BCP micelles. After 1 hour of stirring, the colloidal NC suspension displayed a turbid beige colour. The wafers were washed thoroughly with isopropanol and dried with an antistatic dustless softh cloth to clean the surface from organic molecules. Right before the spin-coating process, the surfaces of the wafers were pretreated by plasma treatment with oxygen to enhance the adhesion of the inorganic $SrTiO_3$ mesoporous NCs with the SiO_2 wafers.

The silicon wafers were coated with 50 µL of the colloidal NC-BCP suspension and rotated at 2000 rpm for 1 minute. After the spinning process had finished the coated wafers were placed on a heating plate at 80 °C to evaporate any residual solvent and prevent crack formations in the film. In order to generate the mesoporous NC framework, the coated wafers were heated to 400 °C at a heating rate of 2 °C/min over 3 hours, and remained at this temperature for another 2 hours. The cubic crystal structure of the $SrTiO_3$ NCs was retained at this temperature treatment as distortions to lower symmetry can only occur at temperatures below room temperature.[53] The resulting mesoporous layers are displayed in figure 3.5.2.
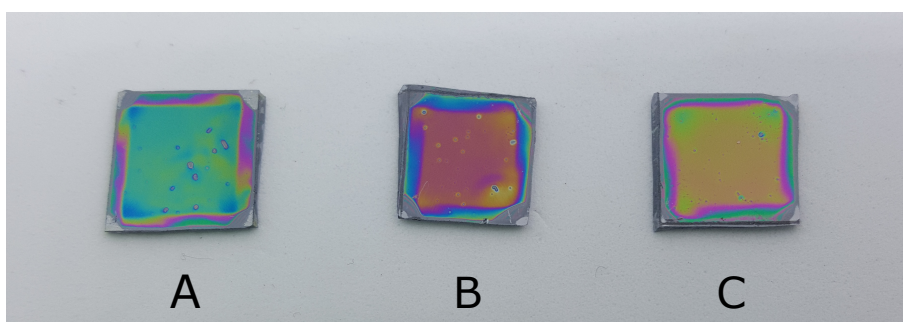
Figure 3.5.2: Mesoporous layers synthesized with block-copolymer P1 through a polymer-templated assembly with varying block-copolymer-to-nanocrystal mass ratio: (A) 1:2 nanocrystal ratio, (B) 1:3 nanocrystal ratio, and (C) 1:4 nanocrystal ratio.
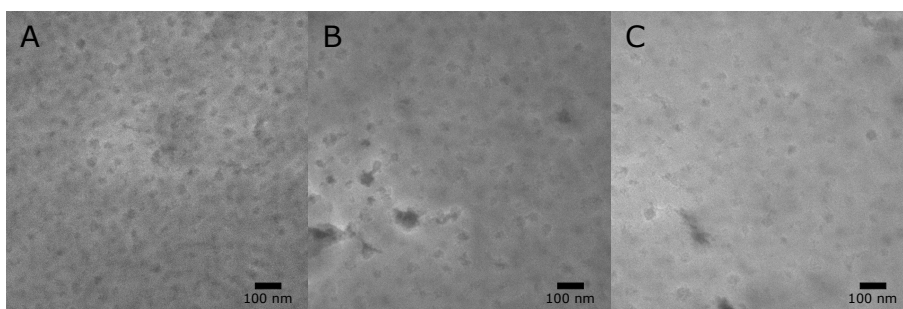
Figure 3.5.3: SEM imaging of mesoporous layers synthesized with block-copolymer P1 through a polymer-templated assembly with varying block-copolymer-to-nanocrystal mass ratio: (A) 1:2 nanocrystal ratio, (B) 1:3 nanocrystal ratio, and (C) 1:4 nanocrystal ratio.

After the final calcining step the coated wafers were analyzed by SEM imaging to study which BCP:NC mass ratio gave the best results in terms of pore size distribution, periodicity and possible defects in the mesoporous layer (figure 3.5.3). As can be seen on figure 3.5.3, neither of the mesoporous layers display pore periodicity or pore size uniformity. Figure 3.5.3.B and 3.5.3.C also exhibit large pores that are the result of supermicelles formed in the BCP micellar solution. Based on this initial test it was decided that the 1:2 BCP:NC mass ratio gave the best results. Several experiments were performed with the BCPs P2, P3, P4 and P5 in a 1:2 BCP:NC mass ratio to test the influence of the pore generating domains M_w on the pore periodicity and size distribution. The resulting mesoporous layers can be seen on figure 3.5.4, and the SEM images are displayed in figure 3.5.5.
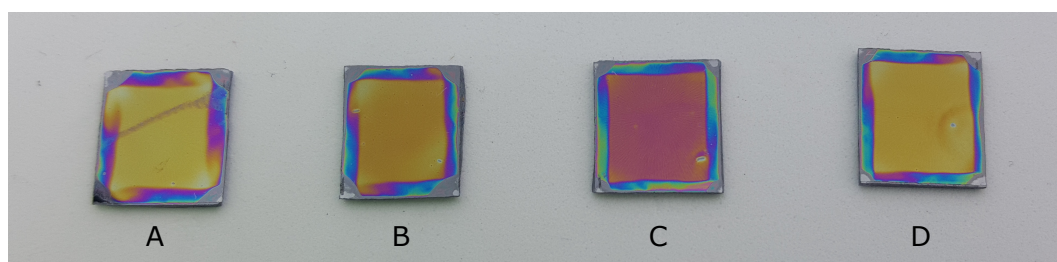
Figure 3.5.4: Mesoporous layers synthesized with a 1:2 block-copolymer-to-nanocrystal mass ratio with (A) block-copolymer P2, (B) block-copolymer P3, (C) block-copolymer P4, and (D) block-copolymer P5 through a polymer-templated assembly.
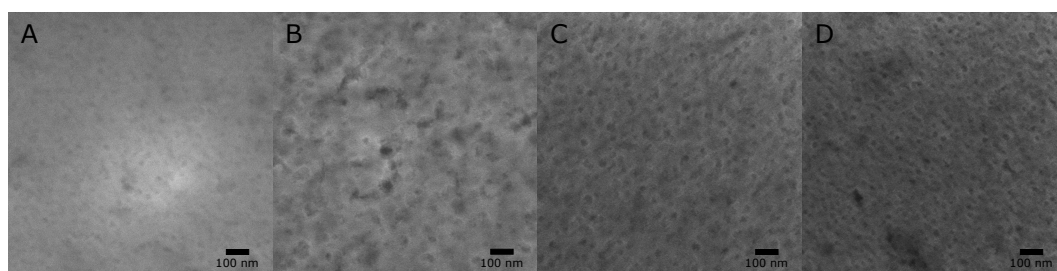
Figure 3.5.5: SEM images of mesoporous layers with a 1:2 block-copolymer-to-nanocrystal mass ratio synthesized with (A) block-copolymer P2, (B) block-copolymer P3, (C) block-copolymer P4, and (D) block-copolymer P5 through a polymer-templated assembly.

The pictures of the resulting mesoporous layers 3.5.4 look promising at first glance, but upon closer inspection several defects in the layers can be observed such as deposition of the NCs across the centrifugal lines of the wafer and macropores due to supermicelles formed in the BCP micellar solution. SEM imaging further confirms that the layers exhibit long pore periodicity, However, long range pore periodicity was not observed. Through optimalization of the stripping procedure with the use of a stronger stripping agent; and with a better BCP:NC mass ratio with the suiting BCP, the mesoporous layers could be drastically improved.

3.5.2 Mesoporous powders

3.5.2.1 Experimental procedure
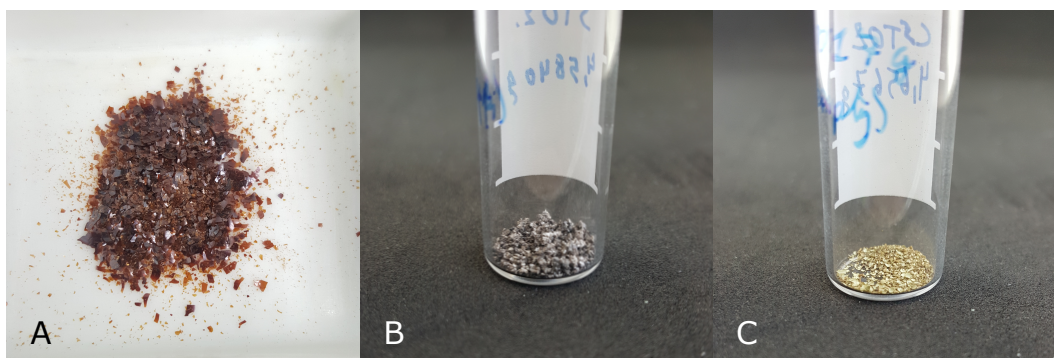
Figure 3.5.6: (A) flake-like precipitate of ligand stripped nanocrystals after drying in the oven, (B) undoped $SrTiO_3$ nanocrystals after calcination, and (C) Cr-doped $SrTiO_3$ nanocrystals after calcination.

Mesoporous $SrTiO_3$ NCs were synthesized in a similar manner as the mesoporous layers. To start, 25 mg of BCP P1 was weighed into a 4 mL glass vial and 400 µL of DMF was added while stirring to dissolve the BCPs. When the BCPs were completely dissolved, 1.6 mL of EtOH was added in drops of 10 µL to obtain a micellar BCP solution. As EtOH was added, the colour of the suspension changed from transparent with a yellow reflection to white turbid with a blue reflection. The solution was left stirring overnight. The NCs were precipitated with hexane/toluene and 100 mg of dry NCs were redispersed in 100 µL of DMF. The micellar BCP solution was added to the NC suspension under vigorous stirring and the resulting BCP-NC suspension was stirred for an additonal 2 hours. The suspension was then poured onto a glass tray and heated to 80 °C for 72 hours to evaporate DMF/ethanol and form the hybrid mesoporous BCP-NC framework through evaporation induced self-assembly. After three days, a flake-like precipitate was obtained (see figure 3.5.6.A) which was calcined at 400 °C for 2 hours at a heating rate of 2 °C/min. The resulting NC framework is displayed in figure 3.5.6.B for the undoped $SrTiO_3$ NCs and figure 3.5.6.C for the Cr-doped $SrTiO_3$ NCs.

3.5.2.2 Characterization

The as-synthesized mesoporous NC framework should allow the retainment of a large surface area whilst providing the structural stability that is desired for photocata-

lytic materials that are often applied in chemically harsh environments. The Brunauer–Emmett–Teller (BET) surface area and pore shapes of both the $SrTiO_3$ and Cr-doped $SrTiO_3$ frameworks were determined through N_2 adsorption-desorption. The resulting isotherm plots are displayed in figure 3.5.7. A significant increase in BET surface area is observed for the Cr-doped $SrTiO_3$ NCs (65.8215 m^2/g) as opposed to the undoped $SrTiO_3$ NCs (27.2723 m^2/g). This variation can be ascribed to a better assembly of the NC framework for the Cr-doped $SrTiO_3$ NCs as opposed to the $SrTiO_3$ NCs. In literature, reported BET surface area values for undoped $SrTiO_3$ (30.7 m^2/g) and Cr-doped $SrTiO_3$ (54.3 m^2/g) particles that are about 300 nm in size and not formed into a NC framework.[88] The BET surface area results presented in this work thus are very promising given the fact that the NCs lose part of their surface area when assembled into a NC framework. The N_2 adsorption-desorption isotherms also displays an H3-type hysteresis loop, following the IUPAC classification, which indicates the pore shapes to be slit-shaped. Consequently, the slit-shape pores do not allow a reliable assessment on the pore size distribution or the total pore volume.[103] The average adsorption Barrett-Joyner-Halenda (BJH) pore width was determined at 12.23 nm for $SrTiO_3$ and 8.284 nm for Cr-doped $SrTiO_3$ respectively.
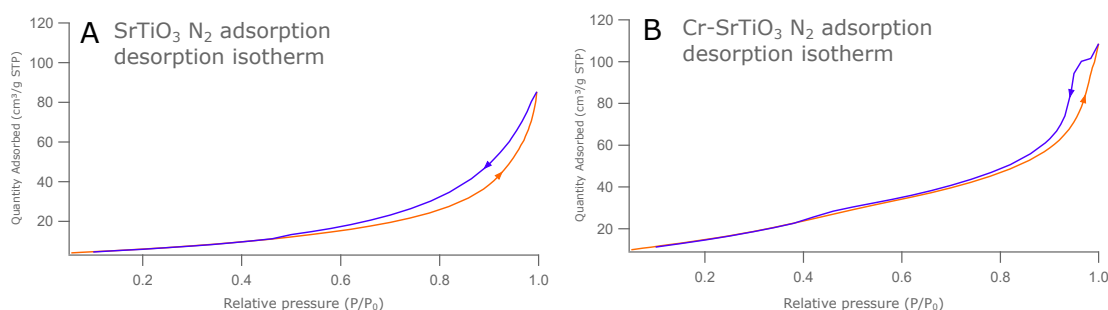
Figure 3.5.7: (A) N_2 adsorption-desorption isotherm of mesoporous $SrTiO_3$ nanocrystal framework, and (B) N_2 adsorption-desorption isotherm of mesoporous Cr-doped $SrTiO_3$ nanocrystal framework.

3.6 Photocatalytic tests

As a proof of concept, the photocatalytic properties of the Cr-doped SrTiO$_3$ NC frameworks were tested through the degradation reaction of methyl orange and methylene blue. Prior work focuses on the degradation of methylene blue through Cr- and Cu-doped SrTiO$_3$ NPs under visible light irradiation.[104,15] Due to pragmatic reasons, we were only able to test the decomposition reaction under UV-light irradiation (mercury lamp $\lambda = 360$ nm).

3.6.1 Experimental procedure

3.6.1.1 Methylene blue

A methylene blue solution in water was prepared with a concentration of 0.05 g/L, and 15 mg of finely grounded Cr-doped SrTiO$_3$ NCs were added to 50 mL of the methylene blue solution. The NC methylene blue mixture was transferred into a glass container which was kept at a constant temperature of 25 °C. First, the mixture was stirred for one hour in complete darkness. A sample (2 mL) was taken before (H00) and after 1 hour of stirring (H0). After 1 hour of stirring, the UV lamp (mercury $\lambda = 365$ nm) was turned on and a sample was taken every 15 min for the first four samples and every 30 min after that. The NCs were first precipitated from the sample by centrifugation, and the clear supernatant was used for the measurement. The resulting UV-Vis measurements can be observed in figure 3.6.1.A.

3.6.1.2 methyl orange

A methyl orange solution in water was prepared with a concentration of 0.01 g/L, and 50 mg of finely grounded Cr-doped SrTiO$_3$ NCs were added to 50 mL of the methyl orange solution.[87] The NC methyl orange mixture was transferred into a glass container which was kept at a constant temperature of 25 °C. First, the mixture was stirred for one hour in complete darkness. The samples were taken in the same manner as was done for the methylene blue experiment. The resulting UV-Vis measurements can be observed in figure 3.6.1.B.

3.6.2 Results
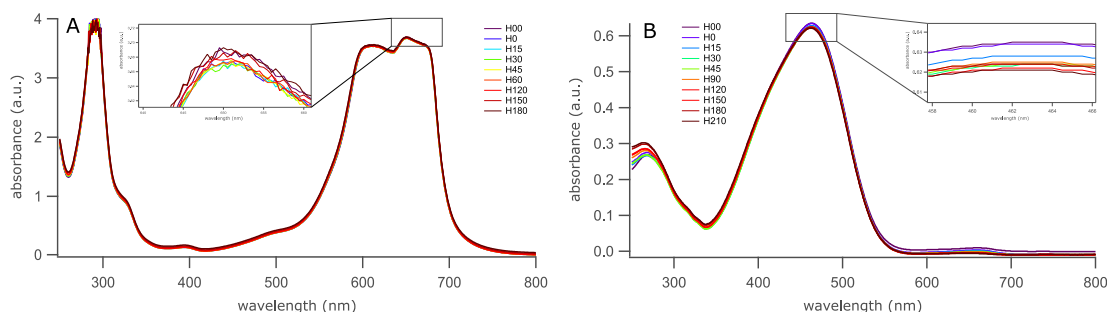
Figure 3.6.1: (A) detail of UV-Vis measurements at $\lambda = 650$ nm during the degradation reaction of methylene blue with Cr-doped SrTiO$_3$ (B) detail of UV-Vis measurements at $\lambda = 463$ nm during the degradation reaction of methyl orange with Cr-doped SrTiO$_3$.

Figure 3.6.1 represents the UV-Vis spectra of the samples taken during the methylene blue (A) and methyl orange degradation reaction (B). A detail of the wavelength region ranging from 458 to 466 nm is shown for the methyl orange spectrum(figure 3.6.1.B). Even though no significant degradation of the organic dye is witnessed, a small decrease in absorbance is observed, A = 0.635 at 0 minutes to A = 0.619 after 210 minutes. This decrease in absorbance is however not significant enough to claim that the synthesized Cr-doped SrTiO$_3$ NC frameworks aid in the photodegradation of methyl orange. The detail of the wavelength region from 640 to 660 nm presented in the methylene blue spectrum (figure 3.6.1.A) also suggests that the synthesized Cr-doped SrTiO$_3$ NC frameworks do not contribute to the photodegradation of methylene blue. The small variations in absorbance can probably be attributed to the sampling method which is non-quantitative and could lead to small differences in the UV-Vis spectra.

The synthesized Cr-doped SrTiO$_3$ NC frameworks thus did not display photocatalytic activity in the photodegradation of methylene blue and methyl orange under UV-light irradiation. When consulting the UV-Vis spectrum of Cr-doped SrTiO$_3$ NCs versus undoped SrTiO$_3$ NCs (figure 3.3.2), a clear improvement of the light harvesting properties of the Cr-doped SrTiO$_3$ NCs was noticed. The lack of photocatalytic activity of the Cr-doped SrTiO$_3$ NC frameworks in the organic dye degradation reactions can thus not be ascribed to an optical inactivity of the synthesized NCs under UV light irradiation. A possible explanation for this photocatalytic inactivity could be that the thiol containing BCP end groups inhibit the photocatalytic properties of the SrTiO$_3$ NCs. Another reason could be that the synthesized NCs

were too small in size, which may have led to a predominantly amorphous NC shell that obstructs effective transport of charge carriers to the surface adsorbed species and/or may have limited adsorption of reactants to the surface. A third possibility is that the NCs are so small in size that the bandgap energy increases due to the disappearance of quantized energy levels in the Ti-3d orbitals and O-2p orbitals. However, no final conclusion as to why the Cr-doped $SrTiO_3$ NC frameworks did not exhibit photocatalytic properties can be made as further research is needed to verify or disprove these hypotheses.

Unfortunately, we were not able to perform CO_2 photoreduction experiments on the Cr-doped $SrTiO_3$ photocatalyst during this master dissertation. CO_2 photoreduction experiments require the use of an air-tight quartz reaction container, irradiated by a light source capable of producing monochromatic visible light and preferably connected to a suitable monitoring system that can detect the CO_2 photoconversion products. As was stated in literature, the two major CO_2 conversion products formed when using $SrTiO_3$ as the photocatalyst are CH_3OH and CH_4.[14,15] Both reaction products require a different measurement system: a liquid chromatograph for the liquid CH_3OH molecules; and a gas chromatograph for the gaseous CH_4 molecules. The reaction setup capable of performing such an experiment could not be completed in the narrow timeframe of this thesis due to practical reasons.

Chapter 4

Conclusions and future perspective

4.1 Summary

The aim of this master dissertation was to synthesize monodisperse, highly crystalline $SrTiO_3$ nanocrystals (NCs) that can be applied for photocatalytic CO_2 reduction applications and organic dye degradation reactions. $SrTiO_3$ is an ABO_3 type perovskite oxide with a bandgap energy of 3.2 eV and has the potential to efficiently convert CO_2 under UV light irradiation into value added chemicals. As UV light only accounts for 4% of the incident sunlight, pristine $SrTiO_3$ is far from an ideal photocatalyst. Upon doping the perovksite oxide with Cr^{3+} ions however the spectral response is extended to the visible light region, accounting for 43% of sunlight, thus improving the photocatalytic application potential of the photocatalyst.

Through the use of trioctylphosphine oxide (TOPO) as a structure directing agent and solvent we were able to synthesize $SrTiO_3$ and Cr-doped $SrTiO_3$ nanoparticles of $\pm$ 3 nm that exhibit excellent monodispersity, size uniformity, crystallinity, and stability in toluene and chloroform. As compared to the frequently used solvent benzyl alcohol, the TOPO synthesized NCs were non-agglomerated and did not require additional surfactants to produce a stable dispersion in toluene. The NPs were coated with a complex TOPO shell consisting of di-n-octylphosphinate (DOPA) groups that were covalently bound to the surface metal atoms, protonated TOPO that interacted with the surface oxygen species through H-bonding, and freely diffusing TOPO. Via surface modidications, we were able to strip the native ligands off of the NC surface and deploy these ligand stripped NCs as building units into a mesoporous NC framework through a polymer-templated assembly. Through a facile oleic acid (OAc)/n-octylamine (octAm) ligand exchange procedure developped by De Roo et

al,[12] the native DOPA ligands and TOPO derivatives were exchanged for OAc ligands under basic conditions resulting in a complete carboxylate shell. To achieve bare cationic NC building units, the OAc capped NCs were stripped using BF_3:Et_2O in DMF as developped by Doris et al.[13] The bare cationic NCs could then be built into a mesoporous NC framework through the aid of block copolymer (BCP) architecture directing agents, a method developed by Helms et al.[84]

The optical response of the $SrTiO_3$ and Cr-doped $SrTiO_3$ NCs was measured through UV-Vis measurements, displaying a distinctive visible light response for the Cr-doped $SrTiO_3$ NCs as compared to the undoped $SrTiO_3$ species. Furthermore, the Cr-doped $SrTiO_3$ NC frameworks exhibited a significant increase in BET surface area (65.8215 m^2/g) as compared to the undoped $SrTiO_3$ NC frameworks (27.2723 m^2/g). This increase in BET surface area of the Cr-doped $SrTiO_3$ NCs can however not be attributed to the creation of oxygen vacancies on the NC surface as more measurements are necessary to make a reliable assessment. It is much more likely that this increased BET surface area can be attributed to a better pore ordering, pore structure and pore size distribution in the Cr-doped $SrTiO_3$ NC frameworks when compared to the undoped $SrTiO_3$ NC frameworks.

A possible application of the synthesized $SrTiO_3$ NCs was briefly explored by depositing the NC frameworks as thin films through spin-coating. Several BCPs with variations in the pore-generating domains and different BCP:NC mass ratios were tested in an attempt to improve the pore periodicity, pore size distribution and pore structure of the mesoporous layers. The resulting thin films were studied through SEM imaging and displayed short range pore ordening as was intended. However, no long range pore periodicity was witnessed and the pores exhibited a slit-shaped structure, as could be derived from the N_2 adsorption-desoprtion isotherms. We expect that with the proper optimalization of the ligand stripping procedure and polymer-templating method, a better result could be obtained. Nonetheless, the facile deposition of the ligand stripped NCs as mesoporous NC frameworks presents a promising application field of the photocatalyst.

Due to practical reasons, we were unable to explore the photocatalytic CO_2 reduction potential of the synthesized photocatalyst. As a proof of concept, the photocatalyst was applied in the degradation reaction of methylene blue and methyl orange under UV light irradiation. Unfortunately, the results of this experiment did not support the theoretical photodegradation ability of Cr-doped $SrTiO_3$ NCs, as was claimed in

prior work.[87,104] A possible explanation for this photocatalytic inactivity could be that the thiol containing BCP end groups inhibit the photocatalytic properties of the SrTiO$_3$ NCs. Another reason could be that the synthesized NCs were too small in size, which may have led to a predominantly amorphous NC shell that obstructs effective transport of charge carriers to the surface adsorbed species and/or may have limited adsorption of reactants to the surface. A third possibility is that the NCs are so small in size that the bandgap energy increases due to the disappearance of quantized energy levels in the Ti -3d orbitals and O-2p orbitals. Due to the narrow timeframe of this master dissertation however, these hypotheses could not be backed by substantial evidence. Possibilities to improve the photocatalytic properties of the Cr-doped SrTiO$_3$ NCs frameworks are discussed in the future perspectives section (section 4.2).

4.2   Future perspective

Embedding Cr^{3+} ions into the crystal lattice introduces discontinuous energy levels into the bandgap of SrTiO$_3$, which result in an increased optical response in the visible light region. We were only able to synthesize and process SrTiO$_3$ and Cr-doped SrTiO$_3$ NCs with a 5 mol% Cr doping into a mesoporous NC framework. Recommendations for future work thus include synthesizing a range of Cr-doped SrTiO$_3$ NCs with different doping levels and characterizing the NCs optical response through UV-Vis measurements. Furthermore, the crystal structure of SrTiO$_3$ lends itself perfectly to foreign element doping, and thus the influence of doping elements other than Cr^{3+} ions into the perovskite oxide could present an interesting extension of the research presented in this master dissertation.

The ligand stripped NCs retained about 23% of their OAc ligands, which obstruct interaction with the NC-tethering domains of the BCPs. Further improvements in the final yield of cationic NCs could thus be obtained by utilizing a stronger stripping agent capable of completely stripping off the OAc ligands. An improvement in pore periodicity, uniform pore size distribution and pore structure of the mesoporous layers and powders is also expected when optimizing the BCP:NC mass ratio in combination with a suitable BCP.

The organic dye photodegradation experiments on methylene blue and methyl or-

ange did not exhibit the photodegradation potential of the Cr-doped $SrTiO_3$ NCs as was claimed in literature.[104] To test whether the lack of degradation of the organic dyes can be attributed to defects in the NC framework, one could repeat the photocatalytic experiments with free Cr-doped $SrTiO_3$ NCs and compare the results to the results for the NC frameworks. One of the possible explanations for this photocatalytic inactivity was owed to the thiol end groups of the BCPs, removing these thiol end groups prior to assembling the BCP-NC framework may verify or disprove this hypothesis. Another reason for the photocatalytic inactivity of the NC frameworks was owed to the small size of the NCs (± 3 nm). Careful control of the NC size through optimization of the reaction synthesis and the resulting effect on its photocatalytic activity thus present an interesting new research topic. A design of experiments can be applied to study which parameters are the size determining factors in the TOPO reaction synthesis.

Because the NCs are so small in size (± 3 nm), a possible explication for the lack of photocatalytic activity might be that the bandgap energy increased due to disappearing quantized energy levels in the conduction band and/or valence band. The careful control of the NC size and its resulting photocatalytic properties in combination with a design of experiments might present an interesting new research subject.

Finally, the photocatalytic CO_2 reduction capability of the Cr-doped $SrTiO_3$ NCs could be explored by devising a reaction setup with a Xenon light irradiation source capable of producing monochromatic visible light, and an airtight glass quartz reactor coupled to a GC and/or HPLC outlet to analyze all CO_2 conversion products.

Chapter 5

Appendix

5.1 Supporting information

Element	Ti (mass%)	Sr (mass%)	Cr (mass%)	C (mass%)	P (mass%)
TOPO capped	13.6	25.4	0.745	58.2	2.03
OAc capped	22.5	32.5	0.486	44.5	0

Table 5.1.1: XRF results of the as-synthesized TOPO capped $SrTiO_3$ nanocrystals and oleic acid capped $SrTiO_3$ nanocrystals.
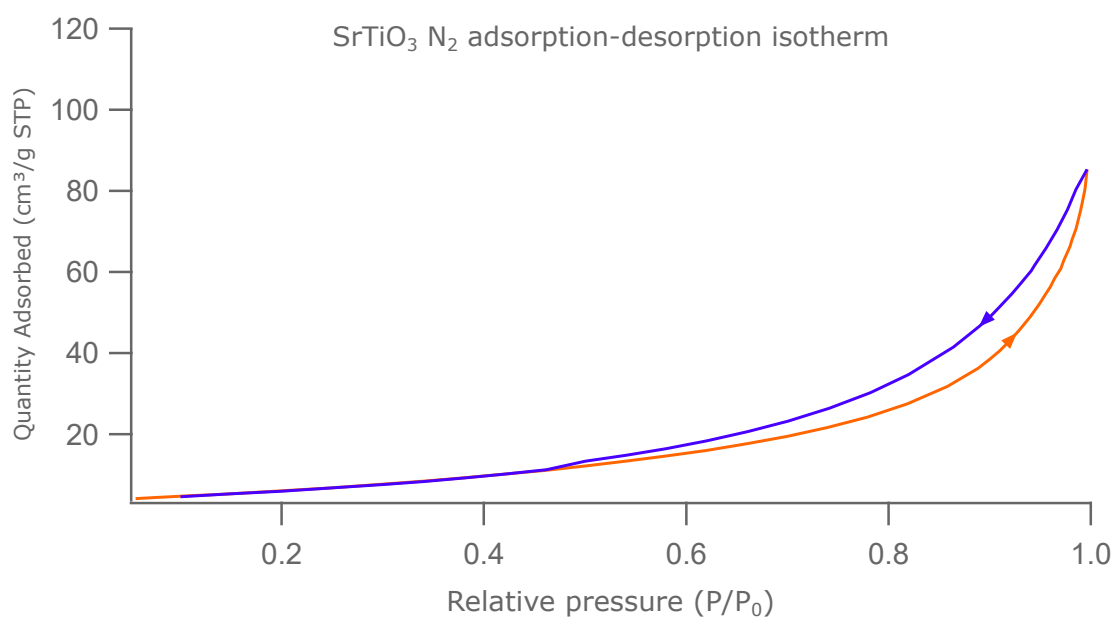
Figure 5.1.1: N_2 adsorption-desorption isotherm of mesoporous $SrTiO_3$ nanocrystal framework.
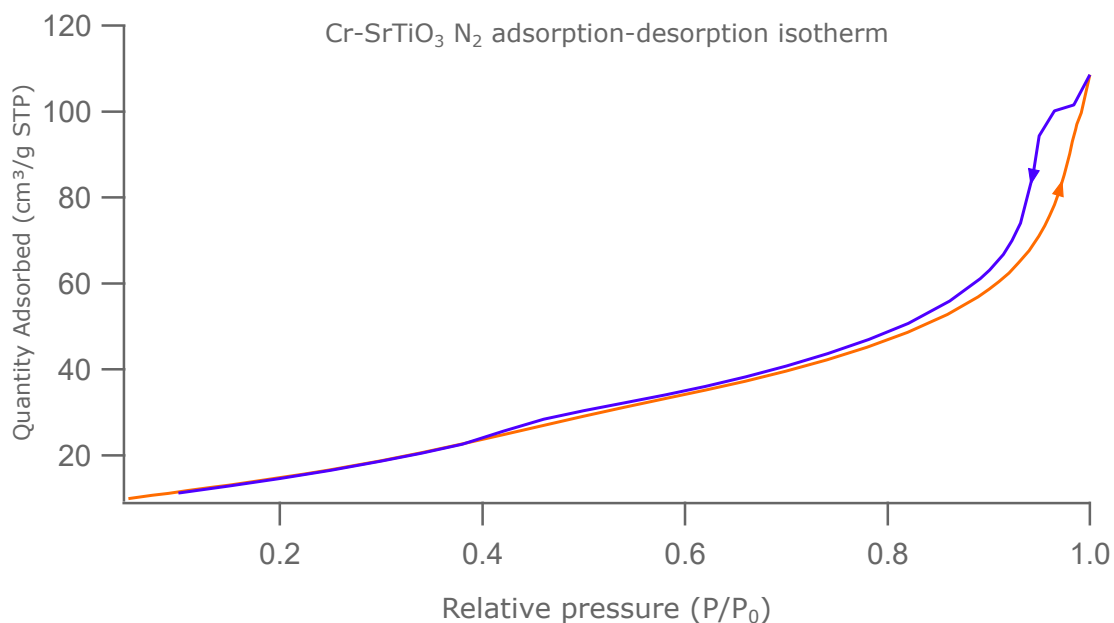
Figure 5.1.2: N_2 adsorption-desorption isotherm of mesoporous Cr-doped $SrTiO_3$ nanocrystal framework.
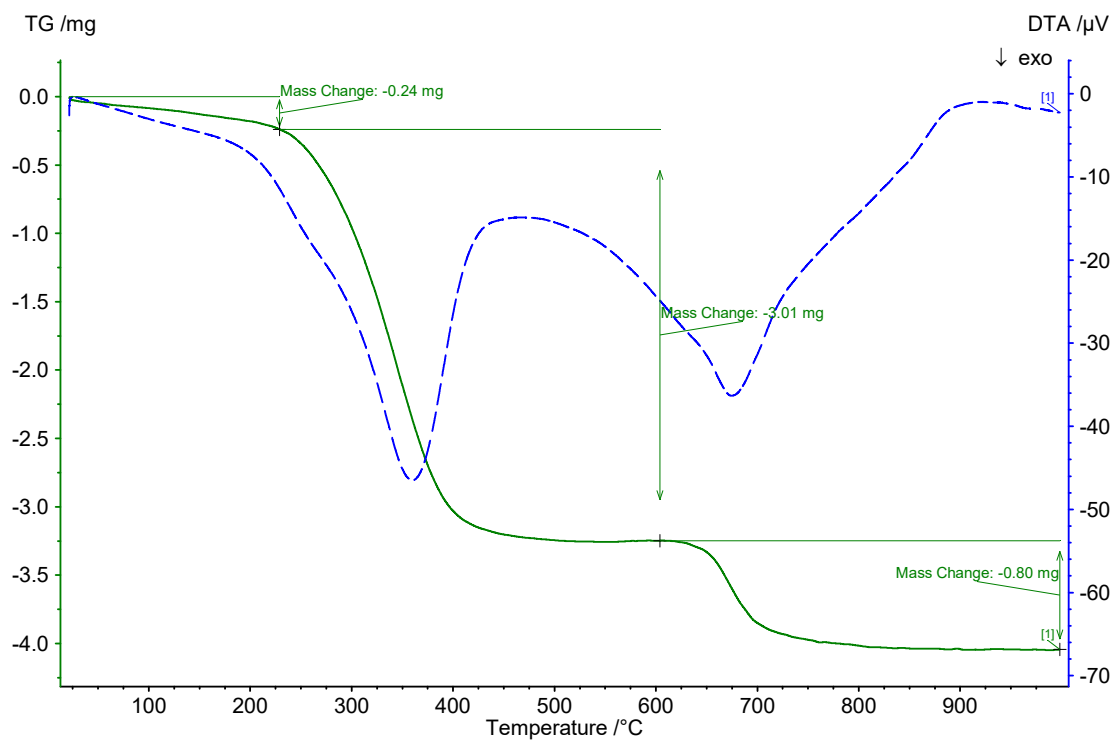
Figure 5.1.3: TGA curve of as-synthesized $SrTiO_3$ nanoparticles coated with free unbound TOPO, protonated TOPO, and di-n-octylphosphinate bound to the surface. Di-n-octylphosphinate is thermally degraded in the temperature region from 600 °C to 700 °C.
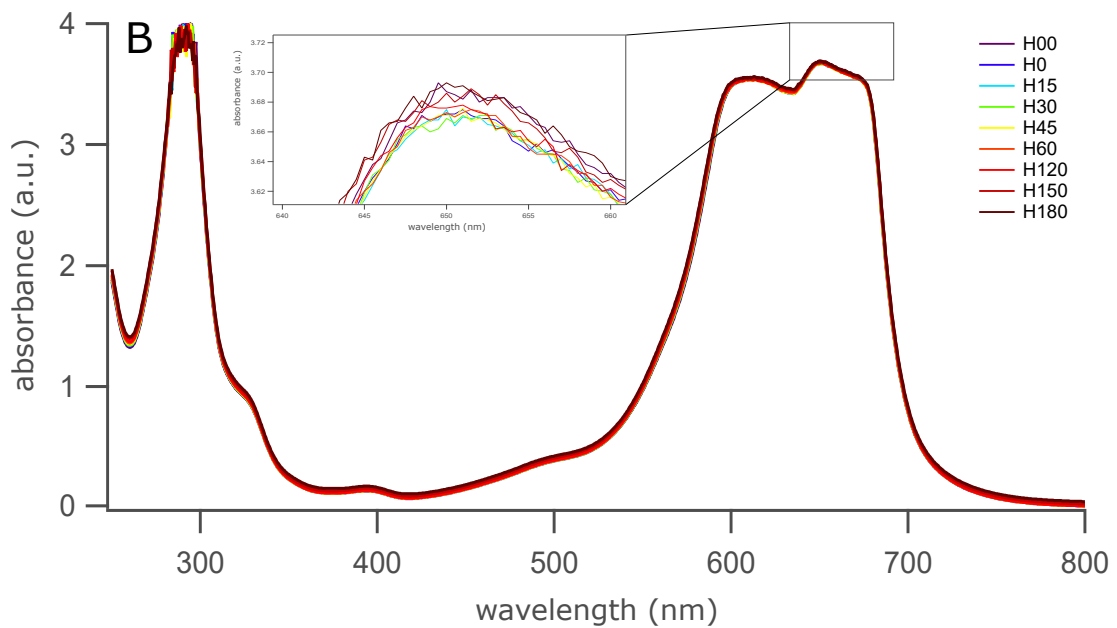
Figure 5.1.4: UV-Vis measurements of the methylene blue degradation reaction with Cr-doped $SrTiO_3$ nanocrystal frameworks, and a detail at $\lambda = 650$ nm. H00 is the first sample before UV light irradiation, H0 when UV light is turned on, H15 after 15 minutes, and so forth.
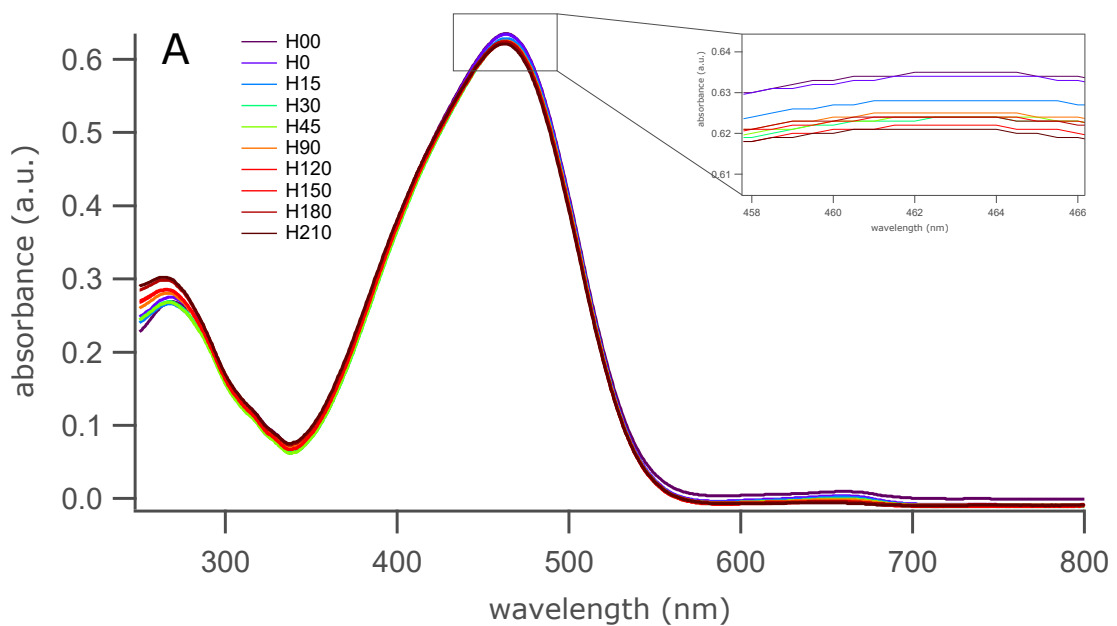
Figure 5.1.5: UV-Vis measurements of the methyl orange degradation reaction with Cr-doped $SrTiO_3$ nanocrystal frameworks, and a detail at $\lambda = 463$ nm. H00 is the first sample before UV light irradiation, H0 when UV light is turned on, H15 after 15 minutes, and so forth.

5.2 Equipment and analysis techniques

5.2.1 Transmission Electron Microscopy (TEM)

TEM measurements were performed on the JEOL JEM-2200FS TEM instrument. The electron beam was produced using a 200 kV field emission gun and equipped with an in-column energy filter.

5.2.2 Scanning Electron Microscopy (SEM)

SEM images were obtained with the JEOL JSM-7600F FEG-SEM instrument. The electron column was combined with semi-in-lens detectors and an in the lens Schottky field emission gun.

5.2.3 Nuclear Magnetic Resonance (NMR)

The Bruker Avance 300 (300 MHz) and the Bruker Avance (500 MHz) FT-NMR were used to obtain the ^{1}H-NMR and the ^{31}P-NMR spectra. The TopSpin software was used to analyze the spectra.

5.2.4 Dynamic Light Scattering (DLS)

A Malvern Nano ZS instrument was used for the DLS measurements. The irradiation source used was a laser beam which produced monochromatic light of wavelength 633 nm and the scattered light was detected at an angle of 173 °.The zetasizer software was used for result analysis.

5.2.5 X-Ray Diffraction (XRD)

The XRD patterns were obtained with a Thermo Scientific ARL X'TRA Powder Diffractometer. The X-ray beam was produced by CuK_{α} radiation. Detection of the X-rays is performed with an Peltier-cooled Si(Li) detector.

5.2.6 X-ray Fluorescence (XRF)

XRF sigansl were measured through with the Rigaku NEX CG instrument. And the analysis software used was the NEX software by Rigaku.

5.2.7   N$_2$ adsorption desorption

The BET adsorption-desorption isotherms were obtained via a Micromeritics TriStar instrument, with N$_2$ as a cooling gas at 77K. The TriStar 3000 V6.08 software package was used to analyse the istoherms.

5.2.8   Thermogravimetric Analysis

The Jupiter STA 449 F3 instrument by NETZSCH was used to perform TGA. The software used was the Proteus Thermal Analysis software by NETZSCH.

5.2.9   Fourier-Transform Infrared spectroscopy (FTIR)

The Nicolet 6700 FT-IR instrumennt by Thermo Scientific was used to obtain FTIR spectra. The software used to analyze the FTIR spectra was OMNIC.

5.2.10   UV-Vis measurements

To measure the UV-Vis response the UV-1800 UV SPECTROPHOTOMETER was used by SHIMADZU. The spectra were processed on the internal software of the instrument.

5.2.11   Spin coating

The instrument used for Spin-coating was MODEL WS-400B-6NPP/LITE by Laurell Technologies Corporation.

5.3   Utilized chemicals

5.3.1   Standard chemicals

Product	CAS	Supplier	Purity	Hazard symbols
Strontium	7440-24-6	Sigma Aldrich	99.9%	
Titanium isopropoxide	546-68-9	Sigma Aldrich	97%	
Methoxyethanol	109-86-4	Sigma Aldrich	99.9%	
Acetonitrile	75-05-8	ROTIPURAN	99.5%	
Trioctylphosphine Oxide	78-50-2	STREM Chemicals	90%	
Toluene	108-88-3	VWR chemicals	90%	
Oleic acid	112-80-1	Sigma Aldrich	90%	-
Oleylamine	112-90-3	Sigma Aldrich	70%	
Octylamine	111-86-4	Acro Organics	99%	
Acetone	67-64-1	VWR Chemicals	90%	
Isopropanol	67-63-0	Fiers	99.7%	
Cr(NO$_3$)$_3$.9H$_2$O	7789-02-8	Acros Organics	99%	
Toluene-d	2037-26-5	Sigma Aldrich	99%	
Butanol	71-36-3	VWR Chemicals	95%	
Pentane	109-66-0	Sigma Aldrich	99%	
Ethanol	64–17-5	VWR Chemicals	99.8 %	
MEEAA	16024-58-1	Sigma-Aldrich	90%	
Methanol	67-56-1	Sigma Aldrich	90%	
Chromium acetylacetonate	21679-31-2	Sigma Aldrich	97%	-
Chloroform	64-66-3	Sigma Aldrich	99%	
Nitrosyl tetrafluoroborate	14635-75-7	Sigma Aldrich	95%	
Dichloromethane	75-09-2	ROTISOLV	99.9%	
Hexane	110-54-3	Sigma Aldrich	95%	
BF$_3$:Et$_2$O	109-63-7	Acros Organics	48%	
Dimethylformamide	68-12-2	ROTISOLV	99.5%	
Methylene blue	122965-43-9	Sigma Aldrich	82%	
Methyl Orange	547-58-0	Sigma Aldrich	85%	

5.3.2 Block copolymers

Polymer	PDMA (g/mol)	PS (g/mol)	PDI
P1	8300	24700	1.30
P2	5100	4700	1.15
P3	5100	8900	1.26
P4	5100	7400	1.16
P5	5100	7900	1.14

5.4 List of abbreviations

Abbreviation	Meaning
BCP	block copolymer
BET	Brunauer Emmett Teller
BJH	Barrett-Joyner-Halenda
CB	conduction band
CBC	valence band
CCS	carbon capture and storage
CCU	carbon capture and utilization
CrAcAc	chromium(III) acetylacetonate
DLS	dynamic light scattering
DMF	dimethylformamide
DOPA	di-n-octylphosphinate
E_{CB}	conduction band energy
E_g	bandgap energy
E_{VB}	valence band energy
FTIR	Fourier-transform infrared
GHG	greenhouse gas
HOMO	highest occupied molecular orbital
LUMO	lowest unoccupied molecular orbital
NC	nanocrystal
NMR	nuclear magnetic resonance
NP	nanoparticle
OAc	oleic acid

octAm	n-octylamine
PDMA	poly(N,N-dimethylacrylamide)
PO	perovskite oxide
PS	polystyrene
rpm	rotations per minute
SEM	scanning electron microscopy
TEM	transmission electron microscopy
TOPO	trioctylphosphine oxide
UNFCCC	United Nations conference for climate change
VB	valence band
XRD	X-ray diffraction
XRF	X-ray fluorescence

Bibliography

[1] Intergovernmental Panel on Climate Change. *Climate change 2014: mitigation of climate change*, volume 3. Cambridge University Press, 2015.

[2] JGJ Olivier, G Janssens-Maenhout, M Muntean, and JAHW Peters. Trends in global co2 emissions: 2015 report. pbl netherlands environmental assessment agency, the hague; european commission, joint research centre (jrc). *Institute for Environment and Sustainability (IES)*, 2015.

[3] IEA. *World Energy Outlook 2017*. Organisation for Economic Co-operation and Development, OECD, 2017.

[4] Michael Zemp. *Global glacier changes: facts and figures*. UNEP/Earthprint, 2008.

[5] John Cook, Naomi Oreskes, Peter T Doran, William RL Anderegg, Bart Verheggen, Ed W Maibach, J Stuart Carlton, Stephan Lewandowsky, Andrew G Skuce, Sarah A Green, et al. Consensus on consensus: a synthesis of consensus estimates on human-caused global warming. *Environmental Research Letters*, 11(4):048002, 2016.

[6] H Douglas Lightfoot and Orval A Mamer. Back radiation versus co2 as the cause of climate change. *Energy & Environment*, 28(7):661–672, 2017.

[7] Iouli E Gordon, Laurence S Rothman, Christian Hill, Roman V Kochanov, Y Tan, Peter F Bernath, Manfred Birk, V Boudon, Alain Campargue, KV Chance, et al. The hitran2016 molecular spectroscopic database. *Journal of Quantitative Spectroscopy and Radiative Transfer*, 203:3–69, 2017.

[8] Ibrahim Khan, Khalid Saeed, and Idrees Khan. Nanoparticles: Properties, applications and toxicities. *Arabian Journal of Chemistry*, 2017.

[9] Run Shi, Geoffrey IN Waterhouse, and Tierui Zhang. Recent progress in photocatalytic co2 reduction over perovskite oxides. *Solar RRL*, 2017.

[10] Steven L Suib. A review of recent developments of mesoporous materials. *The Chemical Record*, 17(12):1169–1183, 2017.

[11] He Yu, Jiajia Wang, Shicheng Yan, Tao Yu, and Zhigang Zou. Elements doping to expand the light response of srtio3. *Journal of Photochemistry and Photobiology A: Chemistry*, 275:65–71, 2014.

[12] Katrien De Keukeleere, Sofie Coucke, Els De Canck, Pascal Van Der Voort, Fabien Delpech, Yannick Coppel, Zeger Hens, Isabel Van Driessche, Jonathan S Owen, and Jonathan De Roo. Stabilization of colloidal ti, zr, and hf oxide nanocrystals by protonated tri-n-octylphosphine oxide (topo) and its decomposition products. *Chemistry of Materials*, 29(23):10233–10242, 2017.

[13] Sean E Doris, Jared J Lynch, Changyi Li, Andrew W Wills, Jeffrey J Urban, and Brett A Helms. Mechanistic insight into the formation of cationic naked nanocrystals generated under equilibrium control. *Journal of the American Chemical Society*, 136(44):15702–15710, 2014.

[14] Luís F Silva, Osmando F Lopes, Vagner R Mendonça, Kele TG Carvalho, Elson Longo, Caue Ribeiro, and Valmor R Mastelaro. An understanding of the photocatalytic properties and pollutant degradation mechanism of srtio3 nanoparticles. *Photochemistry and photobiology*, 92(3):371–378, 2016.

[15] Qazi Inamur Rahman, Musheer Ahmad, Sunil Kumar Misra, and Minaxi Lohani. Efficient degradation of methylene blue dye over highly reactive cu doped strontium titanate (srtio3) nanoparticles photocatalyst under visible light. *Journal of nanoscience and nanotechnology*, 12(9):7181–7186, 2012.

[16] Gavin A Schmidt, Reto A Ruedy, Ron L Miller, and Andy A Lacis. Attribution of the present-day total greenhouse effect. *Journal of Geophysical Research: Atmospheres*, 115(D20), 2010.

[17] José Pinto Peixoto and Abraham H Oort. Physics of climate. 1992.

[18] Josep G Canadell, Corinne Le Quéré, Michael R Raupach, Christopher B Field, Erik T Buitenhuis, Philippe Ciais, Thomas J Conway, Nathan P Gillett, RA Houghton, and Gregg Marland. Contributions to accelerating atmospheric co2 growth from economic activity, carbon intensity, and efficiency of natural

sinks. *Proceedings of the national academy of sciences*, 104(47):18866–18870, 2007.

[19] John Raven, Ken Caldeira, Harry Elderfield, Ove Hoegh-Guldberg, Peter Liss, Ulf Riebesell, John Shepherd, Carol Turley, and Andrew Watson. *Ocean acidification due to increasing atmospheric carbon dioxide*. The Royal Society, 2005.

[20] Richard Vevers. Deterioration of the great barrier reef.

[21] Inventory of u.s. greenhouse gas emissions and sinks. `https://www.epa.gov/ghgemissions/inventory-us-greenhouse-gas-emissions-and-sinks`. Accessed: 2018-05-31.

[22] Elham Karamian and Shahram Sharifnia. On the general mechanism of photocatalytic reduction of co2. *Journal of CO2 Utilization*, 16:194–203, 2016.

[23] Larry Myer. Global status of geologic co2 storage technology development. *United States carbon sequestration council report July*, 2011, 2011.

[24] Zhihua Zhang and Donald Huisingh. Carbon dioxide storage schemes: technology, assessment and deployment. *Journal of Cleaner Production*, 142:1055–1064, 2017.

[25] Brad A Seibel and Patrick J Walsh. Potential impacts of co2 injection on deep-sea biota. *Science*, 294(5541):319–320, 2001.

[26] Mohd Asyraf Kassim and Tan Keang Meng. Carbon dioxide (co2) biofixation by microalgae and its potential for biorefinery and biofuel production. *Science of the Total Environment*, 584:1121–1129, 2017.

[27] Rosa M Cuéllar-Franca and Adisa Azapagic. Carbon capture, storage and utilisation technologies: a critical analysis and comparison of their life cycle environmental impacts. *Journal of CO2 Utilization*, 9:82–102, 2015.

[28] Efthymia Ioanna Koytsoumpa, Christian Bergins, and Emmanouil Kakaras. The co2 economy: Review of co2 capture and reuse technologies. *The Journal of Supercritical Fluids*, 2017.

[29] Ken Allinson, Dan Burt, Lisa Campbell, Lisa Constable, Mark Crombie, Arthur Lee, Vinicius Lima, Tim Lloyd, and Lee Solsbey. Best practice for transitioning from carbon dioxide (co2) enhanced oil recovery eor to co2 storage. *Energy Procedia*, 114:6950–6956, 2017.

[30] Dennis YC Leung, Giorgio Caramanna, and M Mercedes Maroto-Valer. An overview of current status of carbon dioxide capture and storage technologies. *Renewable and Sustainable Energy Reviews*, 39:426–443, 2014.

[31] Wenhui Li, Haozhi Wang, Xiao Jiang, Jie Zhu, Zhongmin Liu, Xinwen Guo, and Chunshan Song. A short review of recent advances in co2 hydrogenation to hydrocarbons over heterogeneous catalysts. *RSC Advances*, 8(14):7651–7669, 2018.

[32] Samsun Nahar, MFM Zain, Abdul Amir H Kadhum, Hassimi Abu Hasan, and Md Riad Hasan. Advances in photocatalytic co2 reduction with water: A review. *Materials*, 10(6):629, 2017.

[33] Kan Li, Bosi Peng, and Tianyou Peng. Recent advances in heterogeneous photocatalytic co2 conversion to solar fuels. *ACS Catalysis*, 6(11):7485–7527, 2016.

[34] Iwao Omae. Recent developments in carbon dioxide utilization for the production of organic chemicals. *Coordination Chemistry Reviews*, 256(13-14): 1384–1405, 2012.

[35] Michele Aresta, Angela Dibenedetto, and Eugenio Quaranta. *Reaction Mechanisms in Carbon Dioxide Conversion.* Springer, 2016.

[36] Xin Li, Jiaguo Yu, Jingxiang Low, Yueping Fang, Jing Xiao, and Xiaobo Chen. Engineering heterogeneous semiconductors for solar water splitting. *Journal of Materials Chemistry A*, 3(6):2485–2534, 2015.

[37] Han Zhou, Jianjun Guo, Peng Li, Tongxiang Fan, Di Zhang, and Jinhua Ye. Leaf-architectured 3d hierarchical artificial photosynthetic system of perovskite titanates towards co 2 photoreduction into hydrocarbon fuels. *Scientific reports*, 3:1667, 2013.

[38] Yi Ma, Xiuli Wang, Yushuai Jia, Xiaobo Chen, Hongxian Han, and Can Li. Titanium dioxide-based nanomaterials for photocatalytic fuel generations. *Chemical reviews*, 114(19):9987–10043, 2014.

[39] Wei Wang, Moses O Tadé, and Zongping Shao. Research progress of perovskite materials in photocatalysis-and photovoltaics-related energy conversion and environmental treatment. *Chemical Society Reviews*, 44(15):5371–5408, 2015.

[40] Peilin Liao and Emily A Carter. New concepts and modeling strategies to design and evaluate photo-electro-catalysts based on transition metal oxides. *Chemical Society Reviews*, 42(6):2401–2422, 2013.

[41] Sheng Zeng, Piyush Kar, Ujwal Kumar Thakur, and Karthik Shankar. A review on photocatalytic co2 reduction using perovskite oxide nanomaterials. *Nanotechnology*, 29(5):052001, 2018.

[42] J Appel. Superconductivity in pseudoferroelectrics. *Physical Review Letters*, 17(20):1045, 1966.

[43] HPR Frederikse, WR Hosler, and WR Thurber. Magnetoresistance of semi-conducting srti o 3. *Physical Review*, 143(2):648, 1966.

[44] Arun Kumar Yadav, Parasmani Rajput, Ohud Alshammari, Mahmud Khan, Gautham Kumar, Sunil Kumar, Parasharam M Shirage, Sajal Biring, Somaditya Sen, et al. Structural distortion, ferroelectricity and ferromag-netism in pb (ti1- xfex) o3. *Journal of Alloys and Compounds*, 701:619–625, 2017.

[45] RA De Souza. Oxygen diffusion in srtio3 and related perovskite oxides. *Advanced Functional Materials*, 25(40):6326–6342, 2015.

[46] RJH Voorhoeve, DW Johnson, JP Remeika, and PK Gallagher. Perovskite oxides: materials science in catalysis. *Science*, 195(4281):827–833, 1977.

[47] Ewelina Grabowska. Selected perovskite oxides: characterization, preparation and photocatalytic properties—a review. *Applied Catalysis B: Environmental*, 186:97–126, 2016.

[48] Junjiang Zhu, Hailong Li, Linyun Zhong, Ping Xiao, Xuelian Xu, Xiangguang Yang, Zhen Zhao, and Jinlin Li. Perovskite oxides: preparation, characteriz-ations, and applications in heterogeneous catalysis. *Acs Catalysis*, 4(9):2917–2940, 2014.

[49] Antonio Guerrero and Juan Bisquert. Perovskite semiconductors for photoelec-trochemical water splitting applications. *Current Opinion in Electrochemistry*, 2(1):144–147, 2017.

[50] Ping Xiao, Jingping Hong, Tao Wang, Xuelian Xu, Yuhong Yuan, Jinlin Li, and Junjiang Zhu. Oxidative degradation of organic dyes over supported per-

ovskite oxide lafeo 3/sba-15 under ambient conditions. *Catalysis letters*, 143 (9):887–894, 2013.

[51] Jasmin Shamshoddin Shaikh, Navaj Shamshoddin Shaikh, Sawanta S Mali, Jyoti V Patil, KK Pawar, Pongsakorn Kanjanaboos, Chang Kook Hong, Jin Hyeok Kim, and Pramod Patil. Nanoarchitectures in dye sensitized solar cells: Metal oxides, oxide perovskite and carbon based materials. *Nanoscale*, 2018.

[52] Markus Niederberger, Georg Garnweitner, Nicola Pinna, and Markus Antonietti. Nonaqueous and halide-free route to crystalline batio3, srtio3, and (ba, sr) tio3 nanoparticles via a mechanism involving c- c bond formation. *Journal of the American Chemical Society*, 126(29):9120–9126, 2004.

[53] Ana Claúdia Lourenço Santana Marques. Advanced si pad detector development and srtio3 studies by emission channeling and hyperfine interaction experiments. 2009.

[54] Wen-Tao Sun, Yuan Yu, Hua-Yong Pan, Xian-Feng Gao, Qing Chen, and Lian-Mao Peng. Cds quantum dots sensitized tio2 nanotube-array photoelectrodes. *Journal of the American Chemical Society*, 130(4):1124–1125, 2008.

[55] Takeo Shimidzu, Tomokazu Iyoda, and Yoshihiro Koide. An advanced visible-light-induced water reduction with dye-sensitized semiconductor powder catalyst. *Journal of the American Chemical Society*, 107(1):35–41, 1985.

[56] Xiaoyan Sun and Jun Lin. Synergetic effects of thermal and photo-catalysis in purification of dye water over srti1-x mn x o3 solid solutions. *The Journal of Physical Chemistry C*, 113(12):4970–4975, 2009.

[57] Jiahui Kou, Jun Gao, Zhaosheng Li, He Yu, Yong Zhou, and Zhigang Zou. Construction of visible-light-responsive srtio 3 with enhanced co 2 adsorption ability: Highly efficient photocatalysts for artifical photosynthesis. *Catalysis Letters*, 145(2):640–646, 2015.

[58] Shang-Di Mo, WY Ching, MF Chisholm, and G Duscher. Electronic structure of a grain-boundary model in srtio 3. *Physical Review B*, 60(4):2416, 1999.

[59] Ryoko Konta, Tatsuya Ishii, Hideki Kato, and Akihiko Kudo. Photocatalytic activities of noble metal ion doped srtio3 under visible light irradiation. *The Journal of Physical Chemistry B*, 108(26):8992–8995, 2004.

[60] Jinshu Wang, Shu Yin, Masakazu Komatsu, Qiwu Zhang, Fumio Saito, and Tsugio Sato. Photo-oxidation properties of nitrogen doped srtio3 made by mechanical activation. *Applied Catalysis B: Environmental*, 52(1):11–21, 2004.

[61] Tsutomu Umebayashi, Tetsuya Yamaki, Hisayoshi Itoh, and Keisuke Asai. Analysis of electronic structures of 3d transition metal-doped tio2 based on band calculations. *Journal of Physics and Chemistry of Solids*, 63(10):1909–1920, 2002.

[62] He Yu, Shuxin Ouyang, Shicheng Yan, Zhaosheng Li, Tao Yu, and Zhigang Zou. Sol–gel hydrothermal synthesis of visible-light-driven cr-doped srtio 3 for efficient hydrogen production. *Journal of Materials Chemistry*, 21(30): 11347–11351, 2011.

[63] Ken-Ichi Tanaka and Atsumu Ozaki. Acid-base properties and catalytic activity of solid surfaces. *Journal of Catalysis*, 8(1):1–7, 1967.

[64] Gongming Wang, Yichuan Ling, and Yat Li. Oxygen-deficient metal oxide nanostructures for photoelectrochemical water oxidation and other applications. *Nanoscale*, 4(21):6682–6691, 2012.

[65] Jinhui Yang, Donge Wang, Hongxian Han, and Can Li. Roles of cocatalysts in photocatalysis and photoelectrocatalysis. *Accounts of chemical research*, 46 (8):1900–1909, 2013.

[66] Huaqiao Tan, Zhao Zhao, Wan-bin Zhu, Eric N Coker, Binsong Li, Min Zheng, Weixing Yu, Hongyou Fan, and Zaicheng Sun. Oxygen vacancy enhanced photocatalytic activity of pervoskite srtio3. *ACS applied materials & interfaces*, 6(21):19184–19190, 2014.

[67] Ryutaro Souda. Resonant ion-stimulated desorption and low-energy proton-scattering study of interactions of hydrogen and oxygen with the srtio 3 (100) surface. *Physical Review B*, 60(8):6068, 1999.

[68] Waranyu Pipornpong, Raina Wanbayor, and Vithaya Ruangpornvisuti. Adsorption co2 on the perfect and oxygen vacancy defect surfaces of anatase tio2 and its photocatalytic mechanism of conversion to co. *Applied Surface Science*, 257(24):10322–10328, 2011.

[69] Clemens Burda, Xiaobo Chen, Radha Narayanan, and Mostafa A El-Sayed. Chemistry and properties of nanocrystals of different shapes. *Chemical reviews*, 105(4):1025–1102, 2005.

[70] S Rajesh Kumar, CV Abinaya, S Amirthapandian, and N Ponpandian. Enhanced visible light photocatalytic activity of porous lamno3 sub-micron particles in the degradation of rose bengal. *Materials Research Bulletin*, 93: 270–281, 2017.

[71] Murid Hussain, Raffaela Ceccarelli, DL Marchisio, Debora Fino, Nunzio Russo, and Francesco Geobaldo. Synthesis, characterization, and photocatalytic application of novel tio2 nanoparticles. *Chemical Engineering Journal*, 157(1): 45–51, 2010.

[72] Francisco Zaera. Nanostructured materials for applications in heterogeneous catalysis. *Chemical Society Reviews*, 42(7):2746–2762, 2013.

[73] Swetlana Schauermann, Niklas Nilius, Shamil Shaikhutdinov, and Hans-Joachim Freund. Nanoparticles for heterogeneous catalysis: new mechanistic insights. *Accounts of chemical research*, 46(8):1673–1681, 2012.

[74] Markus Niederberger and Rupali Deshmukh. Mechanistic aspects in the formation, growth and surface functionalization of metal oxide nanoparticles in organic solvents. *Chemistry-A European Journal*, 2017.

[75] Jonathan Watte, Petra Lommens, Glenn Pollefeyt, Mieke Meire, Klaartje De Buysser, and Isabel Van Driessche. Highly crystalline nanoparticle suspensions for low-temperature processing of tio2 thin films. *ACS applied materials & interfaces*, 8(20):13027–13036, 2016.

[76] Alessandro Lauria, Irene Villa, Mauro Fasoli, Markus Niederberger, and Anna Vedda. Multifunctional role of rare earth doping in optical materials: Non-aqueous sol–gel synthesis of stabilized cubic hfo2 luminescent nanoparticles. *ACS nano*, 7(8):7041–7052, 2013.

[77] Jonathan De Roo, Freya Van den Broeck, Katrien De Keukeleere, Jose C Martins, Isabel Van Driessche, and Zeger Hens. Unravelling the surface chemistry of metal oxide nanocrystals, the role of acids and bases. *Journal of the American Chemical Society*, 136(27):9650–9657, 2014.

[78] Evelyn L Rosen, Raffaella Buonsanti, Anna Llordes, April M Sawvel, Delia J Milliron, and Brett A Helms. Exceptionally mild reactive stripping of native ligands from nanocrystal surfaces by using meerwein's salt. *Angewandte Chemie International Edition*, 51(3):684–689, 2012.

[79] Maksym V Kovalenko, Dmitri V Talapin, Maria Antonietta Loi, Fabrizio Cordella, Günter Hesser, Maryna I Bodnarchuk, and Wolfgang Heiss. Quasi-seeded growth of ligand-tailored pbse nanocrystals through cation-exchange-mediated nucleation. *Angewandte Chemie International Edition*, 47(16):3029–3033, 2008.

[80] Joseph M Luther, Matt Law, Qing Song, Craig L Perkins, Matthew C Beard, and Arthur J Nozik. Structural, optical, and electrical properties of self-assembled films of pbse nanocrystals treated with 1, 2-ethanedithiol. *ACS nano*, 2(2):271–280, 2008.

[81] Kurtis S Leschkies, Timothy J Beatty, Moon Sung Kang, David J Norris, and Eray S Aydil. Solar cells based on junctions between colloidal pbse nanocrystals and thin zno films. *ACS nano*, 3(11):3638–3648, 2009.

[82] Jonathan De Roo, Yolanda Justo, Katrien De Keukeleere, Freya Van den Broeck, José C Martins, Isabel Van Driessche, and Zeger Hens. Carboxylic-acid-passivated metal oxide nanocrystals: Ligand exchange characteristics of a new binding motif. *Angewandte Chemie International Edition*, 54(22):6488–6491, 2015.

[83] Brian J Scott, Gernot Wirnsberger, and Galen D Stucky. Mesoporous and mesostructured materials for optical applications. *Chemistry of materials*, 13 (10):3140–3150, 2001.

[84] Brett A Helms, Teresa E Williams, Raffaella Buonsanti, and Delia J Milliron. Colloidal nanocrystal frameworks. *Advanced Materials*, 27(38):5820–5829, 2015.

[85] Raffaella Buonsanti, Teresa E Pick, Natacha Krins, Thomas J Richardson, Brett A Helms, and Delia J Milliron. Assembly of ligand-stripped nanocrystals into precisely controlled mesoporous architectures. *Nano letters*, 12(7):3872–3877, 2012.

[86] Chih-Ang Chang, Brian Ray, Dilip K Paul, Dmytro Demydov, and Kenneth J Klabunde. Photocatalytic reaction of acetaldehyde over srtio3 nanoparticles. *Journal of Molecular Catalysis A: Chemical*, 281(1-2):99–106, 2008.

[87] Tao Xian and Hua Yang. Photocatalytic degradation of various dyes by strontium titanate nanoparticles. In *Advanced Materials Research*, volume 418, pages 18–21. Trans Tech Publ, 2012.

[88] Yiqing Bi, Muhammad Fahad Ehsan, Yan Huang, Jiarui Jin, and Tao He. Synthesis of cr-doped srtio3 photocatalyst and its application in visible-light-driven transformation of co2 into ch4. *Journal of CO2 Utilization*, 12:43–48, 2015.

[89] Yuji Okamoto, Ryuta Fukui, Motoharu Fukazawa, and Yoshikazu Suzuki. Srtio3/tio2 composite electron transport layer for perovskite solar cells. *Materials Letters*, 187:111–113, 2017.

[90] Jinhai Li, Fei Wang, Lingjun Meng, Mengshu Han, Yang Guo, and Cheng Sun. Controlled synthesis of bivo4/srtio3 composite with enhanced sunlight-driven photofunctions for sulfamethoxazole removal. *Journal of colloid and interface science*, 485:116–122, 2017.

[91] Wei-Hsuan Lee, Chi-Hung Liao, Min-Fei Tsai, Chao-Wei Huang, and Jeffrey CS Wu. A novel twin reactor for co2 photoreduction to mimic artificial photosynthesis. *Applied Catalysis B: Environmental*, 132:445–451, 2013.

[92] Pakpoom Reunchan, Naoto Umezawa, Shuxin Ouyang, and Jinhua Ye. Mechanism of photocatalytic activities in cr-doped srtio 3 under visible-light irradiation: an insight from hybrid density-functional calculations. *Physical Chemistry Chemical Physics*, 14(6):1876–1880, 2012.

[93] Markus Janousch, G Ingmar Meijer, Urs Staub, Bernard Delley, Siegfried F Karg, and Björn P Andreasson. Role of oxygen vacancies in cr-doped srtio3 for resistance-change memory. *Advanced Materials*, 19(17):2232–2235, 2007.

[94] Congjun Wang, Robert L Thompson, John Baltrus, and Christopher Matranga. Visible light photoreduction of co2 using cdse/pt/tio2 heterostructured catalysts. *The Journal of Physical Chemistry Letters*, 1(1):48–53, 2009.

[95] Tooru Inoue, Akira Fujishima, Satoshi Konishi, and Kenichi Honda. Photo-electrocatalytic reduction of carbon dioxide in aqueous suspensions of semi-conductor powders. *Nature*, 277(5698):637–638, 1979.

[96] Satoshi Kaneco, Hidekazu Kurimoto, Kiyohisa Ohta, Takayuki Mizuno, and Akira Saji. Photocatalytic reduction of co2 using tio2 powders in liquid co2 medium. *Journal of Photochemistry and Photobiology A: Chemistry*, 109(1): 59–63, 1997.

[97] Zhihuan Zhao, Jimin Fan, Mingming Xie, and Zhizhong Wang. Photo-catalytic reduction of carbon dioxide with in-situ synthesized copc/tio2 under visible light irradiation. *Journal of Cleaner Production*, 17(11):1025–1029, 2009.

[98] Majeda Khraisheh, Aoubai Khazndar, and Mohammad A Al-Ghouti. Visible light-driven metal-oxide photocatalytic co2 conversion. *International Journal of Energy Research*, 39(8):1142–1152, 2015.

[99] Felix Rechberger, Gabriele Ilari, Christoph Willa, Elena Tervoort, and Markus Niederberger. Processing of cr doped srtio 3 nanoparticles into high surface area aerogels and thin films. *Materials Chemistry Frontiers*, 1(8):1662–1667, 2017.

[100] RH Mitchell, AR Chakhmouradian, and PM Woodward. Crystal chemistry of perovskite-type compounds in the tausonite-loparite series,(sr 1- 2 x na x la x) tio 3. *Physics and Chemistry of Minerals*, 27(8):583–589, 2000.

[101] R Comparelli, E Fanizza, ML Curri, PD Cozzoli, G Mascolo, R Passino, and A Agostiano. Photocatalytic degradation of azo dyes by organic-capped anatase tio2 nanocrystals immobilized onto substrates. *Applied Catalysis B: Environmental*, 55(2):81–91, 2005.

[102] Przemysław Kowalik, Danek Elbaum, Jakub Mikulski, Krzysztof Fronc, Iza-bela Kamińska, Paulo C Morais, Paulo Eduardo De Souza, Rodrigo Barbosa Nunes, Fabiane Hiratsuka Veiga-Souza, Grzegorz Gruzeł, et al. Upconversion fluorescence imaging of hela cells using ros generating sio 2-coated lanthanide-doped nayf 4 nanoconstructs. *Rsc Advances*, 7(48):30262–30273, 2017.

[103] Matthias Thommes. Physical adsorption characterization of nanoporous ma-terials. *Chemie Ingenieur Technik*, 82(7):1059–1073, 2010.

[104] Inamur Rahman Qazi, Woo-Jin Lee, Hyun-Cheol Lee, Mallick Shamshi Hassan, O Yang, et al. Photocatalytic degradation of methylene blue dye under visible light over cr doped strontium titanate (srtio3) nanoparticles. *Journal of nanoscience and nanotechnology*, 10(5):3430–3434, 2010.